UiT

THE ARCTIC UNIVERSITY OF NORWAY

FACULTY OF SCIENCE AND THECHNOLOGY

DEPARTMENT OF GEOLOGY

Microstructural investigation of shear localization in the Ersfjord granite, Kvaløya, Troms:

A case study of kinematics, deformation mechanisms and fabric relationships

—

Daniel Persen

Master thesis in Geology, GEO-3900
May 2014

UNIVERSITY OF TROMSØ

Acknowledgements

I would like to thank my advisor Professor Holger Stünitz for good advice through this work. A big thanks to my secondary advisor Professor Steffen G. Bergh for the time he spent correcting this thesis, notably the work related to regional tectonics. Also, I would like to point out that their many projects throughout this region made this thesis possible.

I wish to thank Edel Ellingsen and Trine Merete Dahl at the department of geology for preparing thin sections studied during this work, and a big thanks to Tom-Ivar Eilertsen at the Department of Medical Biology for preparing carbon damped thin sections used for SEM studies.

I thank PhD Kjetil Indrevær for his discussions and good advice, this thesis was significantly improved! Elizabeth Bunin is thanked for her valuable help with correcting my English.

I would like to mention my fellow students Øystein ("Long Hair" – now, "Short Hair"), Jessica, Solveig, Ole Patrick, Kristoffer, Karina, Ingunn, Tore, Elise, Marta, Trude, Leif and Ingrid: All those moments, through all these years. Unforgettable.

A special mention to my office buddies; Iselin, Aldo and Anna, we had some crazy moments! Now "Gudrun" is out of coffee!

At last, five years of study have come to an end! These are amongst my final words to a challenging year: Thank you!

Elin min kjære, den siste store takk går til deg: Tusen takk for at du har vært en uunnværlig støttespiller gjennom dette året av både frustrasjon og glede! Du har holdt meg gående!

Daniel Persen

May, 2014

Abstract

The present "case study" deals with Paleozoic-Mesozoic oblique-dextral strike-slip shear zones situated within the Ersfjord granite (1,79 Ga), that are believed to give valuable insight into fault- and fluid flow mechanics from the brittle-ductile transition zone. Mesoscopic observations combined with microstructural evidence and geochronology suggests that Late Carbonifereous-Early Triassic fault activity took place, associated with the evolution of the continental margin of Northern Norway. Initial fault movement at minimum pressure-temperature conditions of c. 350°C and c. 290 MPa (c. 11-12 km depth) caused cataclastic failure. The faults appear as single or adjacent connected zones where the cataclasites reactivated the earlier ductile fabric, although most of the rock has also undergone some strain. Three deformation phases were identified: (1) Svecofennian deformation that produced gneiss foliation throughout the granite; (2) formation of semiductile shear zones along- and at a low angle to the foliation fabric; (3) a post-ductile brittle event which propagated along the pre-existing weak fabric and caused overprinting. The studied heterogeneities have acted as fluid canals, where microstructures suggest that pore pressure locally reached lithostatic levels (290 MPa). The fracturing of feldspar phorphyroclasts within the mylonites, the grain size reduction, the deformation mechanisms and the mineral assemblages all point towards greenschist facies conditions during shearing. Grain size reduction caused a switch from dislocation creep to diffusion creep deformation mechanisms. The occurrence of pumpellyite during late stage faulting implies minimum pressure and temperature conditions of c. 275°C and c. 220 MPa (c. 8-9 km depth). The absence of post-kinematic grain growth supports an exhumation history dominated by erosional processes.

"There is no royal road to scholarship, and only those who do not dread the fatiguing climb of its steep paths have a chance of gaining its luminous summits."

KARL MARX

(Preface to the French edition of "Das Kapital")

1. PART 1: INTRODUCTION 1-1

1.1. Chapter 1.1: Introduction 1-1

1.1.1. Thesis outline and objectives 1-2

1.2. Chapter 1.2: Regional geological setting 1-3

1.2.1. Previous work and location of study area 1-3
1.2.2. The West Troms Basement Complex 1-5
1.2.2.1. Neoarchaean TTG-gneisses of various compositions 1-6
1.2.2.2. Neoarchaean and Paleoproterozoic meta-supracrustal rocks overlying the Neoarchaean TTG-gneisses 1-7
1.2.2.3. Early Paleoproterozoic mafic dyke swarms 1-8
1.2.2.4. Paleoproterozoic granitic and mafic plutons 1-8
1.2.2.5. Archaean-Paleoproterozoic deformation, shear zones and fabrics 1-9
1.2.3. Kvaløya 1-11
1.2.3.1. Ersfjord Granite 1-12
1.2.3.2. Kattfjord Complex 1-13
1.2.4. Caledonian nappes 1-13
1.2.5. Post-Caledonian structures and passive margin evolution 1-14

1.3. Chapter 1.3: Methods and data base 1-18

1.3.1. Fieldwork 1-18
1.3.2. Mapping and sampling 1-19
1.3.3. Structural data 1-20
1.3.3.1. Stress- and strain rate estimations 1-21
1.3.3.2. Fabric trajectory calculations 1-23
1.3.3.3. Shear strain calculations 1-24
1.3.3.4. Fluid flow velocity estimations 1-25
1.3.4. Microscopy 1-26
1.3.4.1. Electron backscatter diffraction (EBSD) 1-26

1.4. Chapter 1.4: Clarifications and terms 1-28

1.4.1. Phrasing 1-28
1.4.2. Tables with terms and definitions 1-28

2. PART 2: PETROGRAPHY AND STRUCTURES 2-32

2.1. Chapter 2.1: Introduction 2-32

2.2. Chapter 2.2: Field observations 2-33

2.2.1. Host rock and fabric 2-33
2.2.2. Mesoscopic structures 2-36
2.2.3. Mesoscale kinematic data 2-40

2.3. Chapter 2.3: Mineralogy and microstructures 2-42

2.3.1. Micro-fabrics of the Ersfjord granite 2-42
2.3.1.1. Ductile fabrics 2-43
2.3.1.2. Foliated fabrics 2-48
2.3.2. Ductile Shear zones 2-52
2.3.2.1. Mylonites 2-52
2.3.3. Cataclasites 2-54
2.3.3.1. Mineralogy and textures 2-57
2.3.4. Deformation mechanisms 2-61
2.3.4.1. Dynamic recrystallization 2-62

2.3.4.2. Cataclastic flow 2-67

2.4. Chapter 2.3: Micro-kinematic data and results 2-68

2.4.1. Sense of shear 2-68
2.4.2. Strain and deformation mechanisms 2-72
2.4.2.1. Shear strain within the ductile shear zones 2-72
2.4.2.2. Flow stress and strain rate estimation for the ductile shear zones 2-75
2.4.2.3. Fabric trajectories within the ductile foliation 2-78
2.4.2.4. Cataclastic failure 2-81

3. PART 3: DISCUSSION 3-83

3.1. Chapter 3.1: Introduction 3-83

3.2. Discussion of petrography and structures 3-83

3.2.1. Alteration and precipitation assemblages 3-83
3.2.2. Petrographic constraints on alteration 3-84
3.2.3. Fabric relationships 3-85
3.2.3.1. Brittle-Ductile and Brittle-Plastic relationship 3-87

3.3. Chapter 3.3: Strain analysis and deformation mechanisms 3-93

3.3.1. Ductile shearing 3-97
3.3.1.1. Static recrystallization during progressive deformation 3-99
3.3.2. Semi-ductile to brittle faulting 3-101

3.4. Mineral assemblage and metamorphic conditions 3-104

3.4.1. Metamorphic conditions 3-106

3.5. Chapter 3.5: Comparison with similar setting 3-107

3.6. Chapter 3.6: Timing of shear zone development and structural evolution 3-109

4. PART 4: CONCLUSIONS 4-112

5. PART 5: REFERENCES 5-115

6. PART 6: APPENDICES 6-122

1. Part 1: Introduction

1.1. Chapter 1.1: Introduction

Mylonites and cataclasites are deformation structures commonly observed in quartzo-feldspathic rocks at the brittle-ductile transition, where quartz and mica deform by ductile deformation, while feldspars deform brittlely (Simpson, 1985). The Ersfjord Granite (figure 1-2) in the West Troms Basement Complex (figure 1-3) shows deformation zones of unknown origin. These deformation zones resembles structures to be expected within quartzo-feldspathic rocks (Kohlstedt et al., 1995). Semi-brittle flow produces both plastic- and brittle features within a deformation zone (De Ronde et al., 2004; Gay, 1968; Kilian et al., 2011; Kohlstedt et al., 1995; Mitra, 1978; Shimamoto, 1989). Only brittle failure occurs in cataclastic flow (figure 1-1). The transition from brittle deformation to semibrittle flow occurs when the confining pressure exceeds the plastic flow strength of the rock. On these premises the lithosphere is commonly divided into either two or three rheological regions (Sibson, 1977). In the uppermost part where temperature and pressure are relatively low, frictional sliding on preexisting fractures governs mechanical behavior. At greater depths, due to increasing temperature and pressure, plastic deformation controls the strength of the lithosphere. Between these two regions, brittle and plastic processes interact in a transitional zone. In this transitional zone, each lithological unit increases in strength with increasing depth until the temperature is high enough that plastic flow can occur at lower differential stresses than frictional sliding.

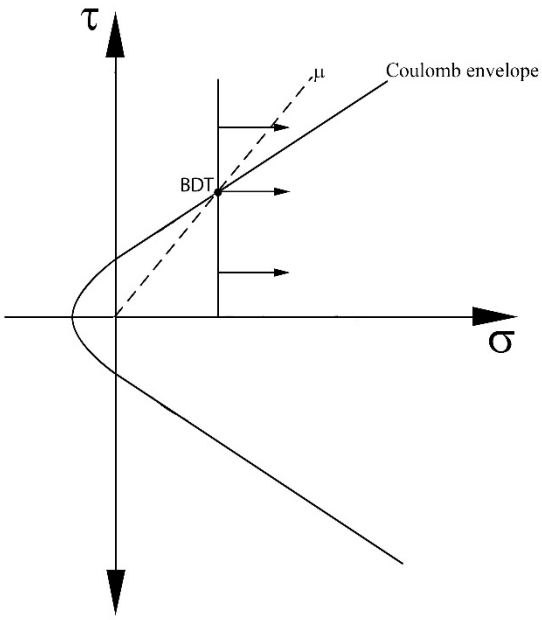

Figure 1-1: Schematic illustration for the transition from brittle failure to semibrittle flow (BDT). Above the brittle-ductile transition (BDT) it would require higher stresses to initiate frictional gliding on pre-exsisting fractures, than to form new ones. Most silicates require elevated temperature and pressure to initiate ductile deformation.

The Ersfjord granite, as studied in this thesis, shows

different deformation structures, reflecting both the brittle-plastic transition and the brittle-ductile transition. These observed heterogeneities may thus shed some light on the origins and temporal evolution of the Ersfjord granite and are studied through a "case study" presented within this thesis.

1.1.1. Thesis outline and objectives

Roughly 1,79 billion years ago, the Ersfjord granite—located in the West Troms Basement Complex—intruded Tonalitic-Trondhjemite-Gneisses (TTG) of Neoarcaean-Paleoproterozoic age. The granite shows signs of deformation: development of foliation, shear zones, fractures and faults. The focus of this thesis is the NNW-ESE striking shear zones located northwest of Grøtfjord, Kvaløya (1.2.1). The geological history of this region is influenced by several tectonic events (section 1.2.2) e.g., different phases of compressional deformation and extensional rifting, related to the opening of the North-Atlantic Ocean. Studies have shown that this rifting resulted in a complex system of post-Caledonian brittle structures both offshore and onshore (Bergh et al., 2007a; Davids et al., 2013; Indrevær et al., 2014a; 2014b; Koehl, 2013).

The purpose of this study is to describe and investigate semi-ductile structures and fractures near the contact between the Ersfjord granite and the Kattfjord Complex, with emphasis on the origins of these structures, depth of formation, deformation mechanisms and timing constraints. These heterogeneities have not previously been mapped in detail, and as such, their origins and associations are not fully understood. Structural data associated with these zones is of importance because structural information provides insight into the kinematic development of the shear zones.

Heterogeneities often form in areas which contain precursor structures; several models exist for explaining the development of brittle and ductile structures in rocks, such as (1) opening of microfractures in an orientation perpendicular to the local minimum compressive principal stress direction (Wilson et al., 2003), (2) nucleation along re-activated *en-échelon* joints (Pennacchioni, 2005), (3) the development of uniform and pervasive foliation parallel to the orientation of maximum compression (Shimamoto, 1989), and (4) reduction of grain size and production of matrix, which allows more fluids to infiltrate the heterogeneities, thus creating a larger area for chemical reactions and further reducing grain size (Mitra, 1978). These types of

models may help to describe the processes that form shear zones; this work attempts to test these hypothesizes.

1.2. Chapter 1.2: Regional geological setting

This chapter describes first the Precambrian geology of the West Troms Basement Complex (figure 1-3), and subsequently summarizes of the Precambrian tectonic evolution of the region (table 1-1). The following sections will, in more detail, focus on the Precambrian geology of Kvaløya and the contact between the plutonic body of the Ersfjord granite (1,79Ga) and the adjacent Archaean Kattfjord Gneiss Complex(>2.6Ga). Furthermore, Caledonian nappes and post-Caledonian brittle structures/faults associated with the evolution of the SW Barents Sea passive margin will be described as a basis for comparison. A summary of the tectonic and magmatic evolution can be seen in table 1-1.

1.2.1. Previous work and location of study area

Previous studies have been carried out in the West Troms Basement Complex. From the earliest recorded work of Keilhau (1861) to the recent work of e.g., Bergh et al. (2012); (2010); Indrevær et al. (2014a); (2014b). The focus during the 19th century was an extensive mapping-project (1:400000) of the northern region of Norway. This early work helped to distinguish the Precambrian basement from the Caledonian cover (Pettersen, 1887, 1891). Presently, the geology catches the interest of students and scientists wanting to describe and decipher the advanced structures (Bergh et al., 2007a; Corfu, 2004; Corfu et al., 2003; 2006; Kullerud et al., 2006a; Myhre et al., 2011; Zwaan, 1992a, 1992b). Still, more and newly discovered geologic features need to be studied in order to better understand the tectonic evolution of the West Troms Basement Complex.

The present study was carried out just north of Grøtfjord (figure 1-2), where ductile and brittle structures crop out along the shore. Grøtfjord is a small village located on northwestern Kvaløya in the Tromsø municipality. The lithologies of the investigated area are part of the West Troms Basement Complex, as seen infigure 1-3. The investigated structures are located within Precambrian basement rocks i.e., the Ersfjord granite (section 1.2.3.1). Special emphasis was given to the study of these structures, which are very similar to those described in earlier studies in respect to their lithologies, kinematics and mineralogy (Antonsdóttir, 2006; Indrevær et al., 2014a; 2014b; Thorstensen, 2011), but their significance has previously not been analyzed with focus on spatial distribution and orientation, kinematics, fault-rock behavior and timing.

Other fault zones in the region (figure 1-2) may be linked to these structures, first described by Antonsdóttir (2006). Presently, observed fault zones near the northwestern edge of the basement high e.g. Bremneset, Tussøya and Hillesøya fault zones (Indrevær et al., 2014a; 2014b; Koehl, 2013) are tentatively grouped together to form a right stepping array of fault segments that run along the westernmost parts of the WTBC. Its continuation eastward is not known.

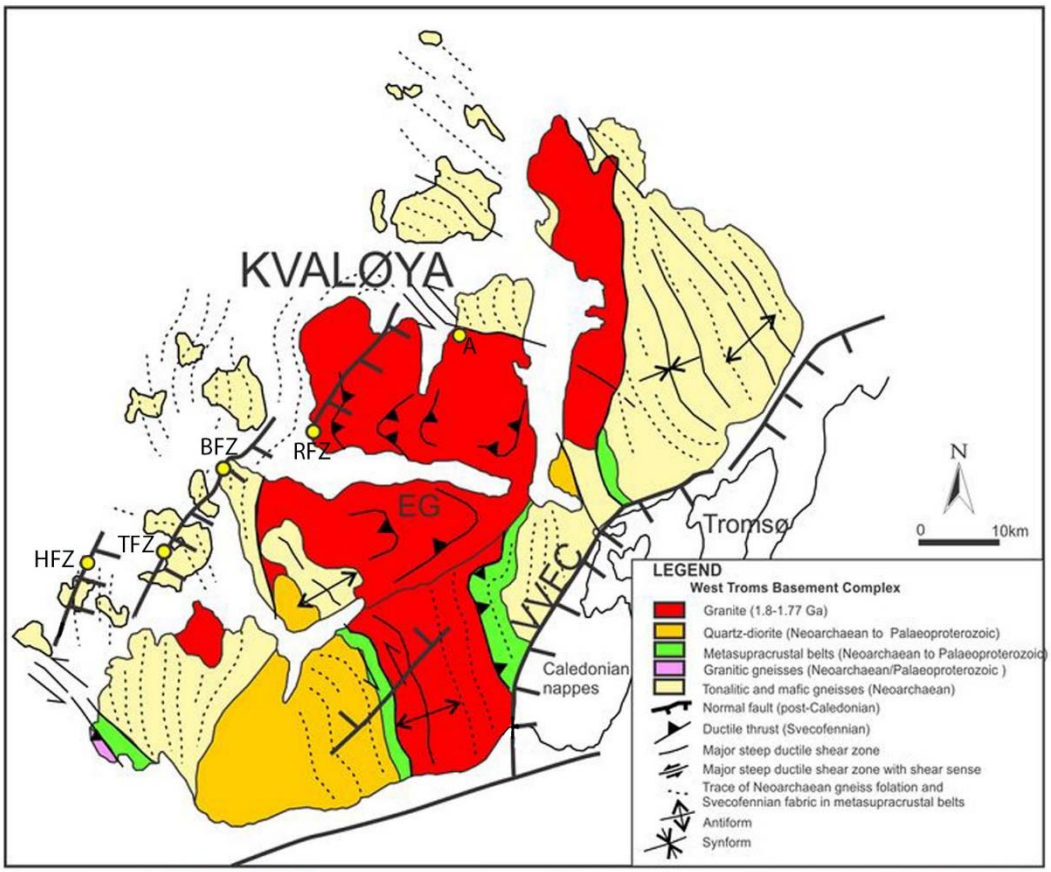

Figure 1-2: Geologic map of Kvaløya with the extent of the Ersfjord granite (EG) and the major post-Caledonian brittle fault zones on the western part.[A] marks the study area for this thesis. Mod. after Bergh et al. (2010) and Indrevær et al. (2014b). Abbrevations: VVFC=Vestfjorden-Vanna Fault Complex, HFZ=Hillesøya Fault Zone, TFZ=Tussøya Fault Zone, BFZ=Bremneset Fault Zone, RFZ=Rekvika Fault Zone

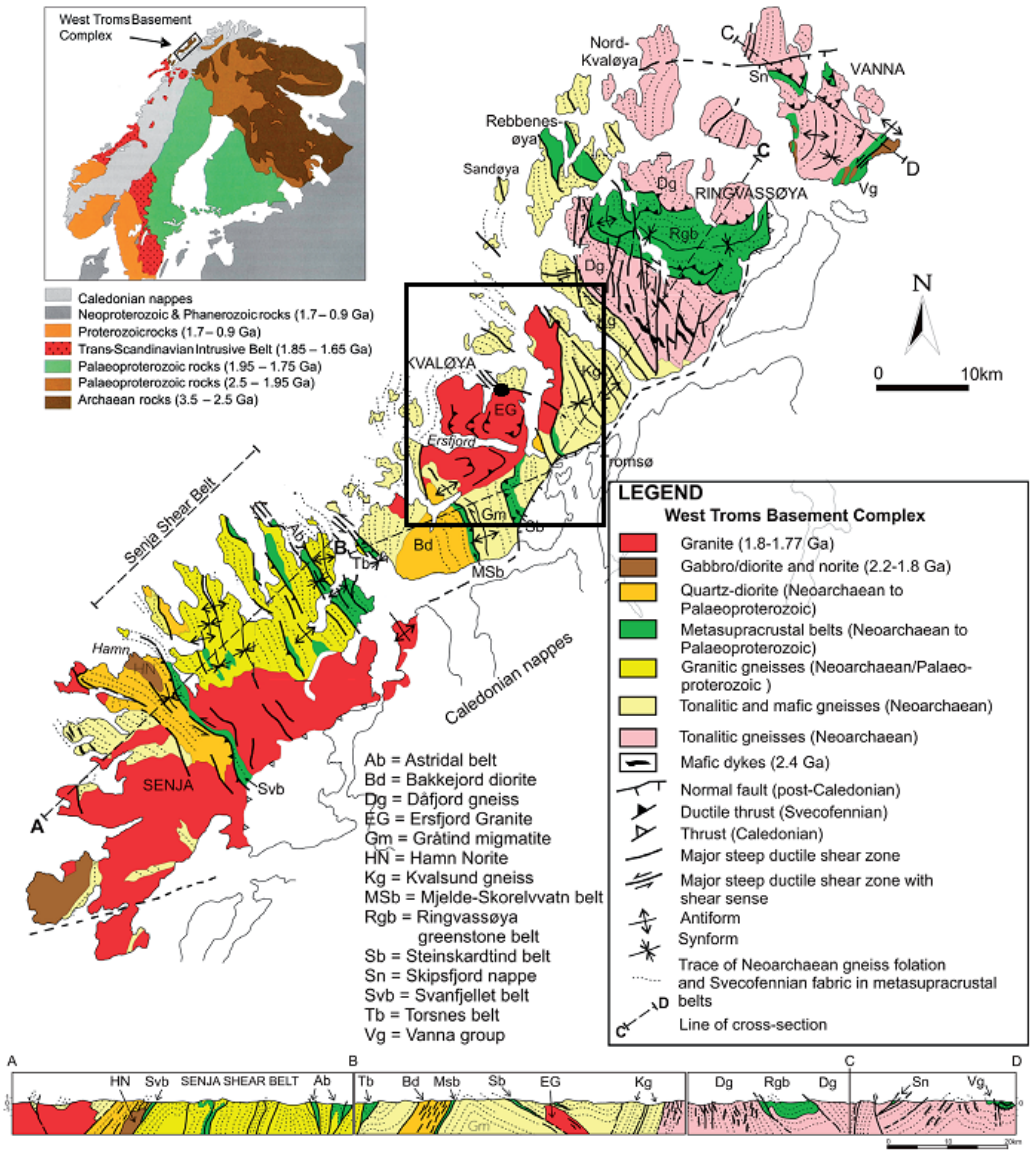

Figure 1-3: West Troms Basement Complex (WTBC) geologic-tectonic map and cross section with included lithology and major onshore structural elements. Infill map show the Fennoscandian shield. The location of field area, in Grøtfjord, is marked with the black square and dot. After Bergh et al. (2010).

1.2.2. The West Troms Basement Complex

The following descriptions of the regional geology, associated with this work, give a general understanding of the most important features and structures.

The WTBC is assumed to be a part of the northern margin of the Fennoscandian shield (Henkel, 1991), and is composed of Neoarchean to Mesoproterozoic TTG-gneisses, meta-volcanic and sedimentary units (greenstone belts), magmatic rocks and numerous ductile shear zones (2,89-1,57Ga) (Bergh et al., 2010). The Precambrian basement rocks are exposed along a series of

islands stretching from Lofoten-Vesterålen (South) to the island of Vanna (North), where the southern suite (Lofoten-Vesterålen) is composed of gabbro, anorthosite, mangerite, charnokite and granite (i.e., the AMCG-suite) with U-Pb crystallization ages of 1,8-1,7 Ga (Corfu, 2004). The northern part, including Senja, Kvaløya, Ringvassøya and Vanna is the main suite called the WTBC, and is composed of Neoarchean gneisses of varied compositions overlain by Neoarchaean and Paleoproterozoic meta-supracrustals, Neoarchaean and Paleoproterozoic mafic dykes, and Paleoproterozoic granitic- and mafic plutons (Bergh et al., 2012; Bergh et al., 2010). To the east, the WTBC is bounded against the Caledonian thrust nappes by a major NE-SW trending fault system—the Vestfjord-Vanna Fault complex—which includes the Kvaløysletta-Straumsbukta fault zone (T Forslund, 1988; Indrevær et al., 2014a). The presumed Permian-Early Triassic oblique-normal faults down-drops the Caledonian nappes by at least 3km (Andersen et al., 1987; T. Forslund, 1988; Zwaan, 1995). On the island of Senja, the Caledonian nappes are locally separated from the basement rocks by a low angle Caledonian thrust. Even though the WTBC is adjacent to the Caledonian orogeny, this crustal segment was only subject to weak metamorphic overprinting (Corfu et al., 2003; Dallmeyer, 1992), and many of the Archaean-Paleoproterozoic textures are preserved (Bergh et al., 2010).

Corfu et al. (2003) and Zwaan (1995) divided the basement rocks of the WTBC into two main zones/suites based on their present day distribution (i) The North-Eastern and (ii) the South-Western, separated by the ~30 km wide Senja shear belt. Later, Bergh et al. (2012); Bergh et al. (2010) divided the basement into four components on the basis of age- and composition different components: (1) Neoarchean TTG-gneisses of various compositions, (2) Neoarchean and Paleoproterozoic meta-supracrustal rocks overlying the Neoarchean TTG-gneisses, (3) Early Paleoproterozoic mafic dyke swarms and (4) Paleoproterozoic granitic and mafic plutons.

1.2.2.1. Neoarchaean TTG-gneisses of various compositions

Meso-Neoarchaean TTG-gneisses characterized by largly tonalitic-to-anorthositic and gabbroitic compositions, as well as banded migmatites, dominate the WTBC northeast of Senja. The oldest rocks are tonalities of the Dåfjord & Kvalsund gneisses that reveal U-Pb zircon crystallization ages of 2,92-2,77 Ga (Andresen et al., 1983; Zwaan et al., 1996). Further north, on Vanna, related tonalites show U-Pb crystallization ages of 2885±20 Ma (Bleeker, 2003). On Ringvassøya, these rocks are overlain by the Neoarchaean Ringvassøya greenstonebelt, which was metamorphosed up to granulite/migmatite facies (Bergh et al., 2010). The greenstonebelt

consists of arc-related meta-volcanics with a MORB-transitional, tholeiitic to calcalkaline affinity (Bergh et al., 2012), meta-volcanics show crystallization ages of c. 2,85 Ga (Motuza et al., 2001). This deformation happened prior to the deposition of Paleoproterozoic cover units and intrusions of 2,4 Ga mafic dyke swarms (Bergh et al., 2010; Kullerud et al., 2006b). The different gneisses are separated by high-grade migmatite zones, interpreted as ductile shear zones e.g., the Kvalsund migmatite zone separating the Dåfjord & Kvalsund gneisses on Ringvassøya (Andresen et al., 1983; Bergh et al., 2012). Common to these gneisses are the following deformation structures: Foliation, boudinaged mafic dykes and intrafolial, symmetrical folds. Together these structures indicate an ENE-VSV to E-V contraction and formation of thrust faults. Multiphase deformation is common and suggests a long Neoarchaean deformation history (Bergh et al., 2010).

1.2.2.2. Neoarchaean and Paleoproterozoic meta-supracrustal rocks overlying the Neoarchaean TTG-gneisses

The dominant meta-supracrustal belts in the WTBC display NW-SE trends that are largely parallel to the ~30 km wide Senja Shear Belt, which includes the Svanfjell-, Astridal- and Torsnes belts (Nyheim et al., 1994; Pedersen, 1997; Zwaan, 1995). North of Senja, smaller belts are present, such as Mjelde-Skorelvvatnbeltet (Armitage et al., 2005), Steinskardtindbeltet and a sheared quartzite unit on Sandøya (Gjerløw, 2008). Further north in the WTBC, broader meta-supracrustal belts dominate the Ringvassøya greenstone belt and the Vanna group, which are continental clastic sedimentary rocks deposited uncomformably onto the TTG-gneisses (Bergh et al., 2007b). New U-Pb ages derived from detrital Zircons reveal an age of deposition between 2403 Ma (underlying Ringvassøya dykes) and 2221±3 Ma, the age of a diorite sill in the supracrustal rocks (Bergh et al., 2012; Kullerud et al., 2006b; Myhre et al., 2011). Some of these belts can be traced several kilometers along strike, while others are discontinuously folded. Observed relict volcanic and sedimentary structures make it evident that, despite having been subjected to Svecofennian high-strain mylonitization and medium-to-high grade metamorphism, these rocks are of a supracrustal origin (Motuza et al., 2001; Nyheim et al., 1994; Pedersen, 1997). Rock types included in the meta-supracrustal belts are meta-conglomerates, meta-psammites, mica-schists and a diverse mafic-to-intermediate meta-volcanics (Bergh et al., 2010). Members of the Ringvassøya greenstone belt reveal the oldest

meta-supracrustal belts, which are U-Pb dated to c. 2,85-2,83 Ga (Kullerud et al., 2006a; Motuza et al., 2001).

1.2.2.3. Early Paleoproterozoic mafic dyke swarms

An extensive mafic, plagioclase-phyric and gabbronoritic dyke swarm, the Ringvassøya dykes, intruded the WTBC Neoarchaean tonalites and Paleoproterozoic meta-supracrustal belts on Ringvassøya, Vanna (Kullerud et al., 2006b), Senja (Zwaan, 1992a) and Kvaløya (Zwaan, 1995; 1992b). Preliminary U-Pb dating using the zircon crystallization method reveals ages of 2670 Ma for a mafic dyke swarm within the Bakkejord diorite (Kullerud et al., 2006a). Zircon and baddeleyite data from the Ringvassøya dykes reveal an age of 2403±3 Ma with a composition (from trace-element geochemistry) between MORB and intraplate basalts. These dykes are nterpreted to have an affinity toward continental tholeiites (Kullerud et al., 2006b). The same authors have observed that the dyke swarms display relict igneous textures and chilled margins. Locally, near the bedrock contacts, the dykes are deformed to a mylonitic fabric, but are otherwise largely undeformed. Most of the dykes strike several kilometers N-S to NNW-SSE and vary in thickness from a few decimeters to more than 100 meters. Some of the dykes intruded parallel to the gneiss foliation, and may be hard to distinguish from the older, surrounding mafic rocks; others intruded and truncated the gneiss foliation (Bergh et al., 2010).

1.2.2.4. Paleoproterozoic granitic and mafic plutons

The Ersfjord granite (1.2.3.1) and the Hamn Norite are the most prominent plutons that intruded the Neoarchaean crust on Kvaløya and Senja, respectively. These are extensive suites of felsic and mafic plutonic rocks (Bergh et al., 2010), respectively. Using U-Pb zircon crystallization methods the Ersfjord Granite reveals an age of 1792±5 Ma (Corfu et al., 2003), and the Hamn norite an age of 1802±2,5 Ma (Kullerud et al., 2006a). Two metamorphic overprints in the Ersfjord Granite are recorded by U-Pb Titanite ages of 1769±3 Ma and 1756±3 Ma (Kullerud et al., 2006a). Bergh et al. (2010) notes that the intrusive contacts with the adjacent gneisses are steep and mylonitized. The ages of these shear zones are unknown, but they may have formed after the main intrusion during the cool down of the granitic body (Stünitz, H. pers. com.). Pronounced, syn-tectonic granite-pegmatite dykes formed synchronously with shear zones in the meta-supracrustal belts at 1768±4 Ma; the formation of these dykes are is most likely genetically related to the main intrusive stage (Kullerud et al., 2006a).

1.2.2.5. Archaean-Paleoproterozoic deformation, shear zones and fabrics

During the Archaean, tectonic accreation and crustal thickening caused by plate convergence resulted in local mylonitization in granulite facies. Accreation may also explain the common mixing of mafic/ultramafic and sedimentary units (e.g., the lower units of the Ringvassøya greenstone belt are comprised of ocean floor and/or continental basalts) (Bergh et al., 2010). A model consistent with the widespread metamorphic ductile gneiss fabrics and stretching lineations in the tonalitic gneisses of the WTBC is E-W crustal thickening by convergence and underplating. This further supports E-W directed shortening in a tectonically thickened portion of the crust.

One complication in studying the Neoarchaean deformation fabrics within the WTBC is that they may be masked by superimposed amphibolite facies deformation related to Svecofennian tectonism. This difference may be shown in slightly younger U-Pb crystallization ages, and compositional variations of the gneisses on Senja and Kvaløya (<2.6 Ga) relative to the gneiss-cover on Ringvassøya (<2,9 Ga) (Bergh et al., 2010). From the derived ages of the Archaean units (>2,2-2,9 Ga; table 1-1 and prior sections), it seems unlikely that Archaean deformation actively affected the Ersfjord granite (1,79 Ga).

Relatively active magmatic events in the WTBC are marked by the felsic and mafic plutons at 1,8 and 1,79 Ga, respectively (1.2.2.4). This period is characterized by compressional tectonism and regional amphibolite- to granulite facies metamorphism, known in Fennoscandia as the Svecofennian orogeny (1,9-1,7 Ga). The most prominent Svecofennian deformation structures, which may be used to understand the Svecofennian tectonism, are (Bergh et al., 2010):

1. NW-SE striking, gently-to-moderately SW-dipping thrusts, and mylonitic fabrics that truncate the c. N-S trending Neoarchaean gneiss foliation
2. Regional antiformal-synformal NW-SE trending, tight-to-upright open folds
3. Steep, NW-SE striking, sinistral, ductile shear zones, with minor dextral strike-slip motions, which formed due to vertical folding
4. SE-directed, low-angle thrusts and steep, semi-ductile shear zones (i.e., on Ringvassøya and Vanna)

Bergh et al. argues that these structures may have formed by at least one Svecofennian tectonic events, where the earliest event produced SW-dipping, local mylonitic fabrics caused by NE-SW orthogonal contraction and dominantly NE-directed thrusting under amphibolite to

granulite metamorphic conditions. This was followed by NW-SE trending upright folds in a similar strain field at amphibolite facies conditions. The Senja shear belt and the Mjelde-Skorelvvatn belt are thought to have developed during these conditions. A third major event involving sinistral, minor dextral, strike-slip shearing at lower amphibolite facies conditions was confined to the NW-SE trending boundaries of the meta-supracrustal belts. This stage marks a change in the convergence direction, from orogen-parallel to transpressive-convergent along the Paleoproterozoic crustal margin. During this stage, strike-slip shearing aligned mafic dykes (e.g., the Svanfjell belt) into parallelism, and also affected the margins of the Ersfjord granite (Bergh et al., 2010), producing mylonitized lithologic contacts.

The presented arguments provide insight into the complex deformation history during formation of the WTBC through Neoarchaean and Paleoproterozoic times. The Ersfjord granite (1,79 Ga) may have been affected by these periods of contraction and transpression.

Table 1-1: Summary of the tectono-magmatic evolution of the West Troms Basement Complex. After Bergh et al. (2010).

West Troms Basement Complex	
Age (Ga)	Components and events
2,92-2,80 2,85-2,83 2,75-2,6 2,75-2,70 2,7-2,67 2,69-2,56	**Neoarchaean cratonization:** - Tonalite crystallization (*Dåfjord & Kvalsund gneisses*) - Volcanism and sedimentation: o *Ringvassøya greenstone belt* **Continued Neoarchaean cratonization:** - Mafic plutonism (*Bakkejord diorite*) in the southwest **Neoarchaean deformation and metamorphism:** - Magmatism, migmatization (*Gråtinden migmatite*) and ductile shearing (*Dåfjord* & *Kvalsund* gneisses) - Main gneiss foliation (initially horizontal), ductile shear zones, tight folds and dip-slip streaching lineation - Medium/high-grade metamorphism, ENE-WSW crustal contraction and thickening by accreation and/or underplating - High-grade metamorphism and resetting
2,40	**Crustal extension and intrusion** of the *Ringvassøya* mafic dyke swarms

2,40-2,20	**Deposition** of *Vanna group* clastic sediments in a marine subsiding basin
2,22	**Intrusion** of *Vanna diorite* sill
2,20-1,90	**Deposition** of *Mjelde-Skorelvvaten, Torsnes* and possibly, the *Astridal* supracrustal belts
1,993 1,80 1,79	**Intrusion/Volcanism** in the *Mjelde-Skorelvvaten belt* **Magmatism/Intrusion** of *granites* and *norite* in Senja **Magmatism/intrusion** of *Ersfjord Granite* in Kvaløya
c. 1,9-1,7 1,90-1,80? 1,78-1,77 c. 1,75? 1,70-1,67? 1,57	**Paleoproterozoic deformation:** - **Early:** Mylonitic foliation (initially horizontal), NW-SE trending gently-plunging isoclinals folds, NE-directed ductile thrusts with dip-slip stretching lineation. Prograde medium/high-grade metamorphism in the southwest. NE-SW orthogonal shortening, NE-directed thrusting/accreation - **Mid:** Regional open upright folding; NW-SE trend flat lying hinges and steep limbs; Low-to-medium grade metamorphism; continued NE-SW orthogonal crustal shortening. - **Late:** Retrogressive low grade metamorphism resulting in steep, regional N-plunging folds; steep, NW-SE striking ductile shear zones (strike-slip) - **Latest:** NE-SW trending upright folds of the *Vanna group* and SE-directed thrusts, steep semi-ductile strike-slip shear zones. Retrogressive low-grade metamorphism. Partitioned NE-SW shortening and orogen-parallel (NW-SE) strike-slip shearing. **Intrusion** of felsic pegmatite and retrogression

1.2.3. Kvaløya

The second largest island within the WTBC is Kvaløya, which is located north of Senja (figure 1-2 and 1-3). Precambrian basement rocks dominate Kvaløya, except for a small Caledonian nappe unit located at the south eastern tip of the island (Zwaan et al., 1998). These rocks are separated from the basement rocks by the NE-SW striking Kvaløysletta-Straumsbukta fault (figure 1-3) (T. Forslund, 1988), which is a part of the Vestfjorden-Vanna Fault Complex (VVFC,figure 1-5).

Bergh et al. (2010) and Myhre et al. (2013) recent geologic work in the region resulted in lithological subdivisions of the Precambrian rocks on Kvaløya: The oldest include the Neoarchaean Bakkejord diorite, the Gråtinden migmatite complex and the Kattfjord complex, dated at c. 2,8-2,6 Ga (Myhre et al., 2013), where the Paleoproterozoic Ersfjord granite is dated to 1,79 Ga (Corfu et al., 2003). Furthermore, these workers identified zones of meta-

supracrustal rocks and intermediate to mafic banded gneiss, as well as partly anatectic meta-supracrustal zones with younger granite and granodiorite, whereas the two dominating lithologies on Kvaløya are the Precambrian Ersfjord granite and the Kattfjord complex (1.2.3.1 and 1.2.3.2).

The strike of the main Archaean foliation on Kvaløya is N-S to NNW-SSE; the foliation dips gently-to-steeply WSW and NNE (Bergh et al., 2010) and is truncated by the Ersfjord granite. A weak foliation is also present in the Ersfjord granite itself; this foliation is now believed to have developed contemporaneously with, or slightly after, the intrusion of the Ersfjord granite (Bergh et al., 2010; Corfu et al., 2006; Kullerud et al., 2006a).

1.2.3.1. Ersfjord Granite

The Erfjord granite covers about 80% of the northwestern Kvaløya and is an intrusive plutonic complex (figure 1-2) (Romer et al., 1992). Aerial estimates for the extent of the granite is c. 40*20 km, and it belongs to the Paleoproterozoic granitic and mafic plutons (1.2.2.4) (Bergh et al., 2010; Zwaan, 1995). The age is revealed to be 1792±5 Ma (Andersen, 1979), with metamorphic overprints at 1769±3 Ma and 1756±3 Ma, respectively. These ages are in accordance with other magmatic suites in the WTBC i.e., the AMCG-suite (U-Pb Zircon dating; 1870-1866 Ma and 1800-1790 Ma) of Lofoten-Vesterålen (Corfu, 2004). During this age interval most known Precambrian juvenile crust were crystallized by arc-related magmatism (Condie, 2005), and suggest that the Ersfjord granite can be correlated to the emplacement of extensive plutonic suites across the Baltic shield during the Svecofennian Orogeny (Gorbatschev et al., 1993; Romer et al., 1992).

The porphyric granite is mostly homogeneous in which 5-15 mm large elongated phenocrysts of alkali-feldspar occur in an equigranular groundmass of quartz and plagioclase, with varying amounts of biotite, muscovite and zoisite. Whereas epidote and allanite, chlorite, titanite, magnetite, hematite, apatite and zircon occurs as accessory/secondary minerals (Romer et al., 1992). Locally the granite has a weak foliation distributed in wide km-thick zones that are mostly parallel to more localized ductile shear zones inside the pluton. These shear zones may be up to tens of meters thick and have a gentle dip to the SSE and NNW (ref, Bergh, S. pers. com.). When approaching the contact they merge into steeper orientations and increase in frequency (Bergh et al., 2010). The shear zone fabrics displays a brittle-ductile and brittle-

plastic relationship, with sigmoidal textures and asymmetric folds yielding a local top-to-the-NW sense of shear (Bergh et al., 2010). The significance and age of these zones are not yet resolved, but clearly the ductile portions of them formed after the main Ersfjord granite intrusion. Late occurring granite pegmatite dykes in the surrounding rocks and meta-supracrustal belts are considered to reflect the subsiding stage of intrusion (Bergh et al., 2010).

1.2.3.2. Kattfjord Complex

Bergh et al. describes the Kattfjord Complex as a part of the Kvalsund gneiss complex, whereas Zwaan (1992b) used that notation as a local term, but it is in fact a part of the Kvalsund gneiss complex (Bergh et al., 2012; 2010).

The dominant lithology of western Kvaløya (figure 1-3) is Neoarchaean tonalitic, banded and migmatitic gneisses with compositions of biotite gneiss, as well as mafic pods (Zwaan, 1992b) and surrounds the Ersfjord granite. Most of these gneisses display amphibolite metamorphic facies, where the protolithic course-grained plutonic texture is recrystallized to elongated fine-grained tonalitic gneiss (Zwaan, 1992b). The Bakkejord pluton and neosomes in the Kattfjord gneiss, yield U-Pb ages between 2,72 and 2,68 Ga, and thus, clearly predates the Ersfjord granite (1,79 Ga). This is supported by the fact that the Kattfjord gneiss foliation is cut by Svecofennian mylonitic fabric and granitic intrusions. Age dating using U-Pb zircon crystallization methods obtained ages of 2733±1 Ma for the tonalitic precursor of the Kvalsund gneiss, and 2587±1,5 Ma for a syn-tectonic granite dyke on NW Ringvassøya (Kullerud et al., 2006a).

1.2.4. Caledonian nappes

Gradual oblique-convergence of the plates Baltica and Laurentia during the Early Paleozoic ultimately led to a collision involving subduction of the margin of Baltica beneath Laurentia and the closure of the Iapetus ocean (Roberts, 2003). The Scandinavian Caledonides comprise a variety of thrust sheets composed of diverse rock compositions, origins and metamorphic grade. During the Caledonian compression the orogeny reached several peaks known as (1) Finmarkian event (Late Cambrian) (2) Trondheim event (Early Ordovician), (3) Taconian event (Mid-Late Ordovician) and Scandian event (Mid Silurian-Early Devonian) (Roberts, 2003), as

the exotic oceanic- and arc terranes got translated onto Archaean and Proterozoic crystalline rocks of the Fennoscandian Shield (Figure 1-3, infill map). As a result of these peaks in compression and numerous thrusts, a distinct tectonostratigraphy can be recognized comprising Lower, Middle, Upper and Uppermost Allochthons. For northwestern Troms Anderson et al. (1992) classified (Figure 1-4) the Upper Allochthon as being composited of the Vaddas, Kåfjord and Nordmanvik Nappes, the Middle Allochthon corresponds to the Målselv Nappe, and the Uppermost Allochthon is composed of the Tromsø Nappe Complex (Indrevær, 2011) which gathers the Troms- and Nakkedal Nappes. Whereas the Lower Allochthon (c.f. Kalak Nappe) has not been recognized in association with the WTBC.

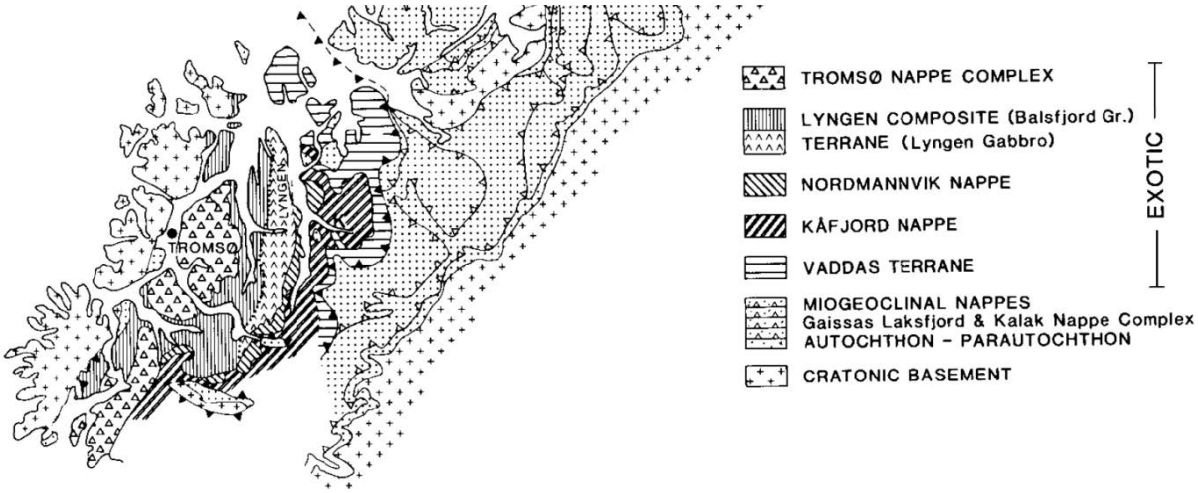

Figure 1-4: Geologic map of the main Caledonian units in Troms (after Andresen (1988))

During the compressional event the Ersfjord granite (1,79Ga) had already intruded into the Baltican crust, and may thus have been subject to weak overprint of Caledonian orogeny (Bergh et al., 2010; Corfu et al., 2003). Even as this convergence still was active at lower crustal levels (i.e., near the subduction zone), a post-orogenic extensional phase progressively started to reactivate low-angle ductile fabrics in the Caledonides, during Early Devonian (Roberts, 2003), causing exhumation and formation of metamorphic core complexes (Steltenpohl et al., 2011). Later the Caledonian nappes were down-faulted by a fault segment that belongs to the Vestfjoren-Vanna Fault Complex (figure 1-5) (T Forslund, 1988; Indrevær et al., 2014a; Olesen et al., 1997)

1.2.5. Post-Caledonian structures and passive margin evolution

During the Paleozoic and Mesozoic the continental margin of Mid-Norway and SW Barents Sea experienced multiple periods of rifting that were linked to the breakup of Pangea, and the final stages in opening of the North Atlantic Ocean in the Cenozoic (figure 1-5) (Faleide et al., 2008; Indrevær et al., 2014a). Mid-Carboniferous, Carboniferous-Permian and Permian-Early Triassic times were the earliest stages of rifting, and in the Western Barents Sea Carboniferous rift structures are common. These intracontinental structures led to the formation of deep rift basins e.g. Nordkapp- and Tromsø basins (Faleide et al., 2008). Rifting during the Permian-Early Triassic, Mid/Late Jurassic-Early Cretaceous and latest Cretaceous-Paleogene on the Lofoten-Vesterålen margin is thought to have occurred during multiple tectonic events (Bergh et al., 2007a). During this period of c. 300 Ma the deep basins developed as rifting propagated northwards leading to Harstad, Tromsø, Bjørnøya and Sørvestnaget Basins in the SW Barents Sea (Faleide et al., 2008; Indrevær et al., 2014a).

Widespread NNE-SSW right stepped normal faults, interconnected with ENE-WSW striking faults are present, both onshore and offshore, along the WTBCs southeastern and northwestern limits (Indrevær et al., 2014a). A set of auxiliary NW-SE trending fracture systems (e.g., reactivated Precambrian ductile shear zones, Caledonian structures or Permian rift structures) occurs, as discussed in this paper. East of the WTBC the onshore Caledonian nappes are down-dropped at least 1-3 km by the Vestfjorden-Vanna Fault Complex (VVFC) and marks the southeastern boundary of the WTBC (T. Forslund, 1988). Onshore on the west-flank of the WTBC no similar fault complex has been identified. Antonsdóttir (2006); Indrevær et al. (2014a); Thorstensen (2011) describes SW-dipping, NW-SE and N-S trending joint fault systems following the outer islands of the WTBC and runs parallel to VVFC. Indrevær et al. (2014a); (2014b) reports a characteristic red staining of the granitic host-rock close to these fault systems. The fault systems are comprised of cataclastic fault-rocks and hydrothermal alteration, with precipitation of epidote, chlorite, quartz, calcite and/or hematite on the fault/fracture surfaces. With kinematic data showing normal- to oblique-normal down-to-the SE movement. They suggested that these faults only accommodated horst-internal displacements in the order of 100's of meters or less, based on similarity with the Skorelvvaten fault zone, where minimum displacement was estimated to 250m. It was concluded that these portions of exposed faults not were the northwestern boundary to the WTBC, but linked up with the Troms-Finnmark Fault Complex (TFFC), where the southern portion of the TFFC defines the northwestern boundary to the WTBC. The link were interpreted as Ringvassøya-Loppa

Fault Complex (RLFC; figure 1-5) based on similarities in geometry, kinematics and displacements.

Davids et al. conducted age dating of onshore brittle faults using $^{40}Ar/^{39}Ar$ and/or apatite fission track (AFT) methods, and indicated that the main rifting events in western-Troms occurred during the Permian through Early Triassic, with no major reactivation during later Mesozoic and Cenozoic (Davids et al., 2013). Age spectra from the same author using the $^{40}Ar/^{39}Ar$ dating method, of hydrothermally altered K-fsp from brittle fault zones related to the VVFC indicates an Early-Mid Permian phase of fault activity. AFT ages from an age-elevation profile of the Store Blåmann mountain varies between 204±8 and 186±8 Ma and suggests rapid cooling through the partial annealing zone. The AFT analysis is only sensitive in the partial annealing zone, with temperatures between 120-60°C, with this in mind, the AFT results indicates that the region cooled to around or below 60°C by the Late Triassic-Early Jurassic, which at a geotherm of 20-30°C/km, corresponds to a depth of 2-3 km (Davids et al., 2013). Olesen et al. associated the cataclasites, fluid circulation and precipitation of hematite with a Permian phase (Olesen et al., 1997).

A.

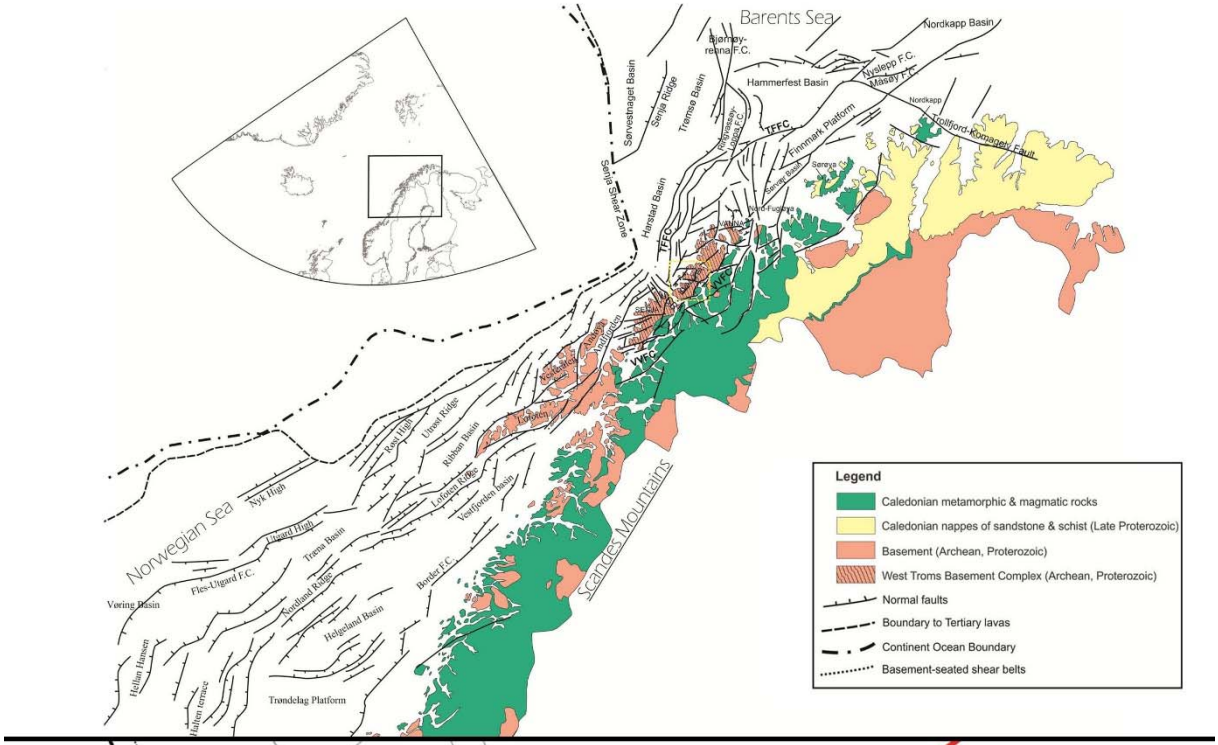
Barents Sea
Nordkapp Basin
Hammerfest Basin
Nyslepp F.C.
Måsøy F.C.
Nordkapp
Trollfjord-Komagelv Fault
Finnmark Platform
Sørvestnaget Basin
Senja Ridge
Tromsø Basin
Senja Shear Zone
Harstad Basin
TFFC
VVFC
Norwegian Sea
Nyk High
Utgard High
Trøma Basin
Fles-Utgard F.C.
Vøring Basin
Rost High
Utrost Ridge
Ribban Basin
Lofoten Ridge
Vestfjorden basin
Nordland Ridge
Helgeland Basin
Border F.C.
Trøndelag Platform
Hellan Hansen
Halten terrace
Scandes Mountains
Legend
Caledonian metamorphic & magmatic rocks
Caledonian nappes of sandstone & schist (Late Proterozoic)
Basement (Archean, Proterozoic)
West Troms Basement Complex (Archean, Proterozoic)
Normal faults
Boundary to Tertiary lavas
Continent Ocean Boundary
Basement-seated shear belts

B.

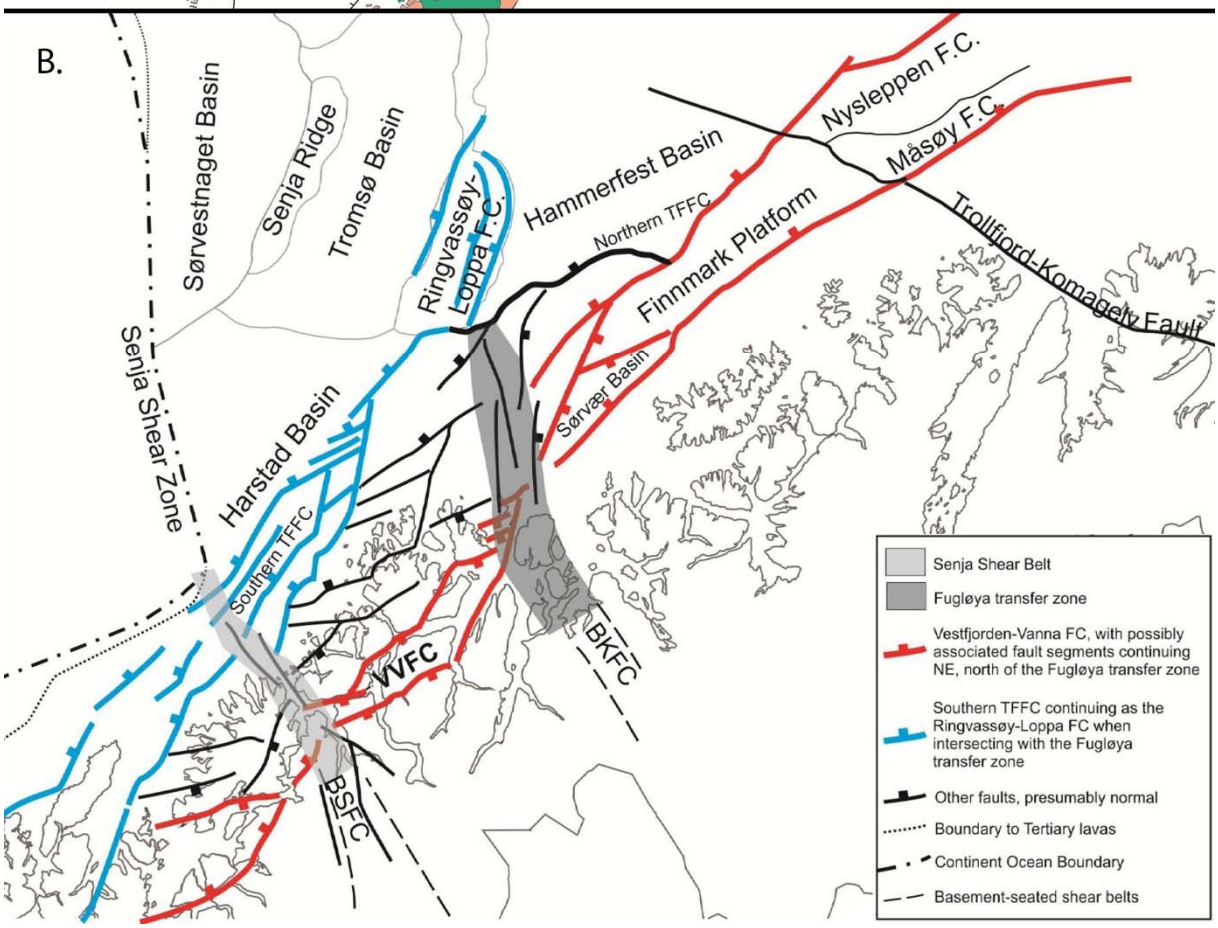
Sørvestnaget Basin
Senja Ridge
Tromsø Basin
Ringvassøy-Loppa F.C.
Hammerfest Basin
Nysleppen F.C.
Måsøy F.C.
Northern TFFC
Finnmark Platform
Trollfjord-Komagelv Fault
Sørvær Basin
Senja Shear Zone
Harstad Basin
Southern TFFC
VVFC
BKFC
BSFC
Senja Shear Belt
Fugløya transfer zone
Vestfjorden-Vanna FC, with possibly associated fault segments continuing NE, north of the Fugløya transfer zone
Southern TFFC continuing as the Ringvassøy-Loppa FC when intersecting with the Fugløya transfer zone
Other faults, presumably normal
Boundary to Tertiary lavas
Continent Ocean Boundary
Basement-seated shear belts

Figure 1-5 (Prev. page): (A) Regional tectonic onshore-offshore map, and setting of the mid-Norwegian shelf, along the West Troms Basement Complex and the SW Barents Sea margin. (B) Simplified tectonic model of the SW Barents Sea region linking major NNE-SSW and ENE-WSW trending fault complexes onshore and offshore, where two transfer zones, BSFC and BKFC, accommodated stepping of faults along the margin. After Indrevær et al. (2014a); (2014b). Abbreviations: TFFC=Troms-Finnmark Fault Complex, VVFC=Vestfjorden-Vanna Fault Complex, BSFC=Bothania-Senja Fault complex, BKFC=Bothania-Kvænangen Fault Complex

1.3. Chapter 1.3: Methods and data base

Within this chapter a description of the completed field work is presented, as well as a description of the equipment used throughout the gathering- and analyzing of data. This chapter also highlights the software used for projecting structural data, as well as containing defined equations used throughout the thesis for calculations e.g., shear strain, fabric anisotropy, flow laws etc. (1.3.3).

1.3.1. Fieldwork

Studies were carried out north of the village, along the shore, in Grøtfjord (figure 1-2, 1-3, and 2-1). The study area is located on the contact between the Ersfjord granite (1.2.3.1) and the Kattfjord Complex (1.2.3.2). The outcrop is well exposed and ideal for structural work, but the extent of exposure is limited, from the beach (south) and approximately 150 m. northwest to a boulder field. Further north, c. 50 m, is the contact with the Kattfjord Complex. The direct exposure of the shear zones and cataclastic zones are limited to approximately 20-30 m. along strike, depending on the tide.

Field work was completed in September 2013 with detailed mapping and sampling of relevant structures. The focus was the brittle-ductile/brittle-plastic shear zones and its adjacent cataclastic zones, and other adjacent brittle structures that cut through and/or displaced the main shear zones. Planar- and linear structures (i.e., strike and dip of shear zones, cataclasites, foliation and stretching lineation), were measured (2.2). Other goals during fieldwork were to collect representative samples of the different structures associated with the shear zones e.g., cataclasites, mylonites and foliation. The samples were taken along strike of the main shear zones, and adjacent to it. Some samples contain foliation and cataclastic zones, whereas others mylonites, and a few contains a combinations of the two fabrics.

All samples collected in this work are from outcrop, none are taken from “floats”, which assures a certain quality to the samples and to the locality.

1.3.2. Mapping and sampling

Detailed mapping was done on mm-scale paper, using a 1*1 m square grid divided into 10*10 cm grids (figure 1-6 A) on a scale of 1:10 and later converted to 1:100 (figure 2-1). The grid was moved 1 m. at a time, and mapping was done simultaneously for as long as the shear zone was exposed. The raw drawings were then scanned using an *Epson Expression 1640XL* and processed in *Photoshop CS6 Extended*, producing the final lithological map.

From outcrop samples were sawed out using a handheld power cutter of brand *Husqvarna,* and a 2 kg hammer and chisel (figure 1-6 B-C). All the raw samples were then taken back to the rock lab (Emilbua) at the Department of Geology, University of Tromsø for processing into thin rock slices, using a *CEDIMA CTS-265* saw and following, processed into small rock chips with a size of 2*4*2 [cm], using a *MK Diamond Products MK101XL* saw (figure 1-6 D). These chips where then sent to the geologic laboratory, Department of Geology, University of Tromsø for processing into thin sections.

All locations and samples on the outcrop were photographed using a *Nikon D800* attached with a *Nikon 50mm/f1,4* lens. After processing the samples at Emilbua into thin slices they were photographed; to have a reference for all the thin section locations and the associated rock.

Figure 1-6: (A) The grid used for mapping. It is 1x1 meter and divided into 10x10 cm squares. (B) An unprocessed, sawed out, raw sample across the shear zone and cataclastic zone. Pen=14cm. (C) The common size of the gathered rock samples. The sample displayed is taken across a cataclastic zone. Marker=14 cm. (D) After processing the raw samples, using the CEDIMA CTS-265, the result is rock slices like this. Black squares mark where the thin sections are taken from. The arrow with an «x» represents the «up dip» direction, and the straight arrow mark the lineation direction. Across sample=14 cm.

1.3.3. Structural data

Orientation data of structural elements were obtained using a *Suunto MC-2* compass, corrected for magnetic declination. The strike and dip of the planar elements is presented as right hand rule (RHR), and linear elements are presented as azimuth and plunge. All illustrations of planar- and linear data of the structural elements, are presented as lower hemisphere equal-area stereographic projection, using the program *Orient 2.1.1* (Vollmer, 2011). Data are either plotted as big circles, pole to plane plots or as slip-plots (Goldstein et al., 1988).

To infer the relative timing of structural data, a number of basic criteria were used e.g., cross-cutting, intersections, mergence, splaying or fracture terminations, and bending/rotation of fabric against each other, or mineralization patterns.

Kinematic analysis were performed using several basic kinematic indicators to constrain the relative slip motion (2.2.3 and 2.4.1). These include slickensides or mineral lineation, which are among the most widely used kinematic indicators for brittle and ductile faults. All recorded indicators are plotted in slip-linear plots, and projected as lower hemisphere equal-area stereographic plots, where the arrows indicates the movement of the hanging wall.

Photoshop CS6 Extended is the software used to produce lithological maps, illustrations and figures. Modifications are also done it the same software.

MATLAB R2013b is the software used for the calculations and plotting of data. It is applied to plot the displacement of the foliation (1.3.3.2) and estimate the fluid flow velocity (1.3.3.4).

1.3.3.1. Stress- and strain rate estimations

The flow stresses has been calculated using three different paleopiezometers: One empirically derived paleopiezometer (Stipp et al., 2003), and two theoretically derived (Shimizu, 2008; Twiss, 1977). The empirical paleopiezometer defined by Stipp et al. only considers the grain size. Calculations based on Shimizu's work, were done for α-quartz because no chessboard subgrain patterns was observed, which suggests that only α-quartz are present, in addition, other microstructures suggests that deformation took place below the α-β quartz transition zone. The last paleopiezometer, defined by Twiss, flow stress is plotted versus recrystallized grain-size within a x,y-diagram (figure 1-7).

The paleopiezometers are given as:

$$\sigma = \sqrt[1,26]{\frac{3631}{D}} \qquad [1],$$

from (Stipp et al., 2003), where σ is flow stress [MPa] and D is the recrystallized grain size [μm].

$$\sigma = 217 * D^{-0,8} exp^{\left(\frac{1190}{T}\right)} \qquad [2],$$

from (Shimizu, 2008), where T is absolute temperature [K].

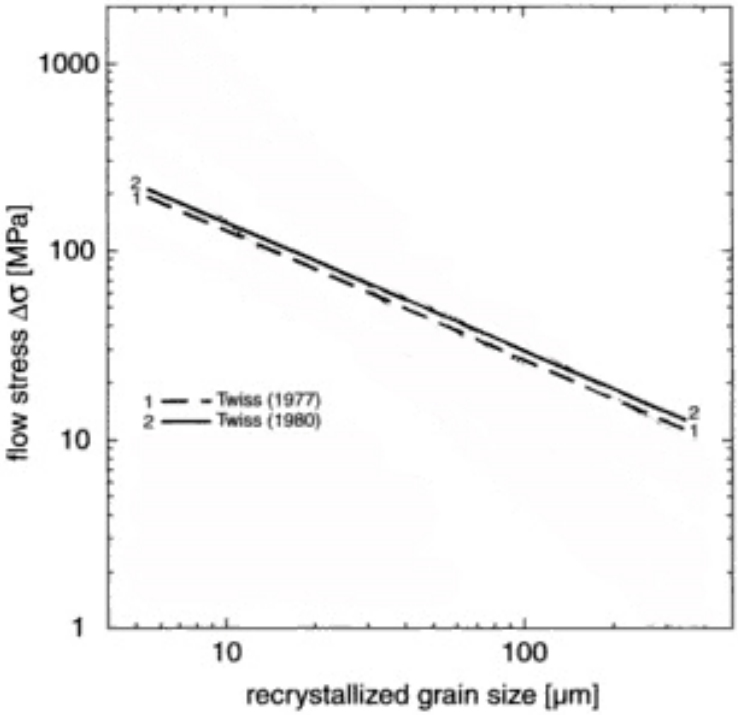

Figure 1-7: A paleopiezometer, where flow stress and grain size is plotted in an x,y-diagram, defined by Twiss (1977)

From figure 1-7 it is possible to directly read the theoretically derived flow stress, for a given recrystallized grain size.

In calculating the flow stresses (eq. [1], [2] and figure 1-7) presented in table 2-4, recrystallized grain sizes obtained during diameter grain size counting were used (2.4.2.2) and a temperature of 350°C. This temperature is chosen because it is believed being representative of the conditions under which the measured grains deformed; the temperature is consistent with the observed deformation (e.g., SGR) and mineral assemblages (2.3.2.1).

Strain rate ($\dot{\varepsilon}$) was calculated using the flow law for dislocation creep after Hirth et al. (2001):

$$\dot{\varepsilon} = A * f_{H_2O}^{m} * \sigma^{n} exp^{\left(\frac{-Q}{RT}\right)} \qquad [3],$$

where A is a material constant, $f_{H_2O}^{m}$ is water fugacity [MPa] and m is the water fugacity exponent, σ is the flow stress [MPa], n is an empirical exponent, typically set as 3-5 (Gleason et al., 1995; Luan et al., 1992; Stipp et al., 2002a), Q is the creep activation energy [$Jmol^{-1}$], R is the Boltzmann constant per mole (gas constant) and T is the absolute temperature [K].

Water fugacity was determined for pure water from the Pitzer et al. (1994) equation of state. Fugacity was calculated using the analytical solution:

$$\ln f = \left[\ln \rho + \frac{A^{res}}{RT} + \frac{P}{\rho RT}\right]_{P,T} + \ln(RT) - 1 \qquad [4],$$

where f is water fugacity, A^{res} is residual Helmholtz energy, ρ is "molar" density (n/V) and P, T and R is pressure, temperature and the Boltzmann gas constant, respectively. A JavaScript [1] completed the calculations. Water fugacity was calculated for a lithostatic pressure, corresponding to a minimum temperature of 350°C, using the established geothermal gradient of c. 30°C/km (2.3.3.1).

One sets of values were used for water fugacity and activation energy (Hirth et al., 2001), reflecting on the observed recrystallization microstructures:

(a) log(A)=-11,2 $MPa^{-n}s^{-1}$, f_{H_2O}= 38 MPa (at c. 290 Mpa, and 350°C) n=4, m=1, Q=135 kJ mol^{-1}

1.3.3.2. Fabric trajectory calculations

Fabric trajectories, presented in section 2.4.2.3, were constructed to infer the relative shear strain and displacement for the foliation in the Ersfjord granite. Figure 1-8 illustrates the fabric trajectories, which represent lines to which the long axes of the strain ellipsoid (greatest stretch) are the tangent in every point along the fabric trajectories.

First a reference line was defined parallel to the trend of the shear band that represents the shear plane. Then inclination lines were constructed with a 10 degree interval, from 10° to 40° and, respectively, moved parallel through the shear zone, marking points where the inclination line acts as a tangent to the fabric trajectories. A line connecting these points, where surfaces have an equal inclination, with respect to the reference line (i.e. isogons), was constructed. Then, shear strain (γ) was calculated for the inclination lines using the formula:

$$\gamma = \frac{2}{\tan 2\theta} \qquad [5],$$

where [Θ] is the angle between the reference line and the fabric trajectory.

Finally, the γ-values versus the distance across the shear band, for three cross sections, were plotted into an x,y-diagram. The y-axis was chosen for γ-values and the x-axis for distance values on the traverse across the shear band. In the end, displacement was determined by box-counting the area under the curves on a millimeter grid. The resulting area represents the

apparent displacement of the shear band. For a graphically solution an integration formula is defined:

$$D = \int_0^x \gamma dx \qquad [6]$$

The reason why this area represents the displacement is because shear strain (γ) is a unit less number and it is multiplied by a distance [mm] across the shear zone.

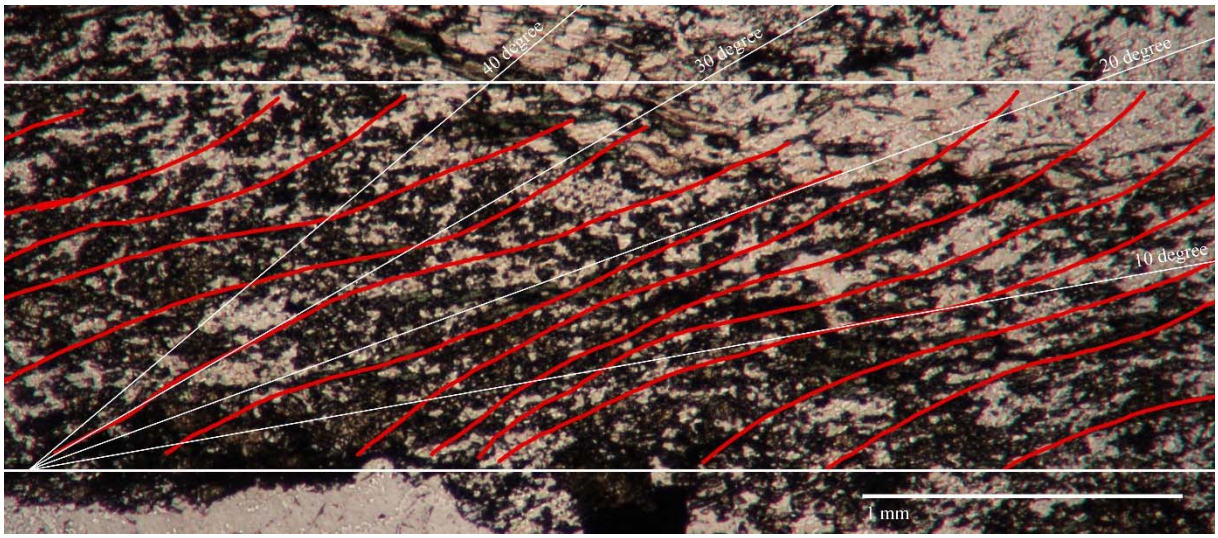

Figure 1-8: The red lines represent fabric trajectories for given shear band. The horizontal white lines are the reference lines and marks the shear band borders. The inclination lines marks points where their inclination, with respect to the reference line, has the same value (i.e. 10°, 20°, 30°, 40°) Sample: DP01_2.

Because the microphotograph is magnified, a conversion factor of 0,0149 was established, based on the magnification of the microphotograph and the print-out used to do the raw calculations. See section 1.3.4 for calculations.

1.3.3.3. Shear strain calculations

Shear strain for the ductile shear zones was calculated with the formula defined by Ramsay et al. (1983) p.295-296:

$$\gamma^* = \frac{(R^*-1)}{\sqrt{(R^*)}} \qquad [7],$$

where R^* is the aspect ratio for the recrystallized quartz aggregates. The reason why aspect ratio R* is used is because it is a more robust measurement compared to the rotation angle α*.

Shear strain was also calculated for the minimum displacement of the cataclastic zones, given by the two similar relationships:

$$\gamma = \tan \Psi \vee \frac{x}{y} \qquad [8],$$

where Ψ is the angle between displacement and width; x is displacement and y is width of the zone.

1.3.3.4. Fluid flow velocity estimations

With the presence of injected material into faults and fractures in the fault rocks, as described in section 2.3.3, it was possible to roughly estimate both the fluid velocity and fault slip rate during faulting. By considering *Stokes Law* which describes the movement of particles in a fluid (settling velocity *[U]*), where fluidizing occurs as the fluid velocity *[v]* surpasses the settling velocity:

$$v \geq U = \frac{2}{9} * \frac{(\rho_s - \rho_f)}{\mu} * gR^2 \quad [9],$$

where ρ_s is the sphere (clasts) density of the granite [2700 kg*m^{-3}], and ρ_f is the density of the fluid (variable), *G* is the gravitational constant and *R* is the radius of the spheres in the fluid [50µm and 100µm] and µ is the dynamic viscosity [Pa*s (kg*m^{-1}s^{-1})].

The biggest uncertainties are the fluid density when estimating the slip rates, therefore the formula was converted to a linear relationship displaying the slip rate as a function of fluid density:

$$y = a\rho_s + b \quad [10],$$

where *a* is slope of the line and *b* is the intercept of the y-axis. See the appendices for the constants and the linear relationships used to construct the plot.

Three constants were used for the dynamic viscosity [µ] (Bruges et al., 1966; Schmidt et al., 1963), one for water at 300°C as a basis of comparison (Indrevær et al., 2014b), two for water at 350°C, which is the temperatures believed to being representative of the conditions at which the deformation occurred (see 1.3.3.1). The constants are as follows:

1. For 300°C; µ=10^{-4} kg*m^{-1}s^{-1}, R=100µm
2. For 350°C; µ=7,28*10^{-5} kg*m^{-1}s^{-1}, R=100µm and 50µm
3. For 350°C; µ=6,48*10^{-5} kg*m^{-1}s^{-1}, R=100µm and 50µm

Estimations are presented in section 2.4.2.4 as a linear relationship. The estimations based on constants from point (2) and (3) were done two times, with the different grain sizes.

1.3.4. Microscopy

Thin sections were studied using a *Leitz Laborlux 11 pol s* transmitted light microscopy. During this study the mineralogy and the optical visible microstructures was described. All microphotographs were performed with a *Canon EOS 650D,* with a resolution of 5184x3456 pixels, attached to a C mount with magnification of 2,5x, mounted on a *Leica DM/LP* microscope, with no binning and objective magnification.

The actual pixel size [APS] of the microphotographs were established using the following equation for the different magnifications on the microscope:

$$APS = \frac{Camera\ resolution * Binning}{Lens\ mag * C\ mount * objective\ mag} \qquad [11],$$

where 5184 is camera resolution [px], binning was set to 1 (not present), lens mag was 2,5x, 5x, 10x or 62x, respectively, C mount was 2,5x and objective mag was set to 1 (not present).

By calculating the APS [nm], it was possible to determine how many pixels each scale bar should be, for the different microscope magnifications. Photoshop was used to construct the scale bars for each picture throughout this thesis, and the scale bar lengths [px] were calculated using this formula:

$$Scale\ bar\ length = \frac{Lenght\ [nm]}{APS} \qquad [12]$$

For instance, the scale bar length [px] is 1206 pixels for a microscope magnification of 2,5x: APS = 829,44 nm (eq. [11]). Then if the wanted scale bar is 1 mm, the calculation is as follows: 1000000 [nm]/829,44 [nm] = 1206 pixels, which represents 1 mm in the microphotograph.

1.3.4.1. Electron backscatter diffraction (EBSD)

The electron backscatter diffraction (EBSD) analysis were carried out in a Zeiss Merlin VP Compact scanning electron microscope (SEM), attached with an energy-dispersive X-ray spectroscopy detector (EDS). To be able to do this analysis, the thin sections were damped with

carbon in a vacuum for 15 minutes at the Department of Medical Biology, University of Tromsø.

The EDS analysis were used to identify the mineral pumpellyite, as described in section (2.2.3), and shown in figure 2-9 andfigure 2-13. The spectrums obtained are in large part due to the principle that each element has a unique atomic structure allowing unique set of peaks on its X-ray spectrum. The obtained spectrums are highlighted in appendix 4, corresponding with the calculated atomic structure.

The calculations were done in an excel spread sheet (seen in appendix 4), and are as follows:

The number of cations present in the pumpellyite structure are 8. The *GFW* is the molar weight for the respective oxides (e.g. Cr_2O_3 = 2*51,996+3*15,9994), and the *Wt.%* are the input-field for the oxides obtained during EDS analysis. The *mole units* are the measured *Wt.%* divided by the *GFW* for each element respectively, and the *cation units* are *mole units* multiplied with the amount of cations present for the oxides (e.g. the oxide Cr_2O_3 contains two cations, and are thus multiplied with 2). The total number of all cations should equal 8, thus are the *normalized cation units* calculated as this: *cation units* divided by the sum of all *cation units* multiplied with 8.

Based on these calculations it were possible to determine which cations fills the crystal structure of pumpellyite. Silicium are expected the fill 3 places, aluminum, manganese, magnesium and ferrous iron (Fe^{2+}) together are expected to fill 3 spaces, and calcium are expected to fill 2 spaces, which sums up to 8 cations in the crystal structure. The *actual values* represents how well the oxides fit into the pumpellyite structure. Results that occur at an accuracy of ±0,1 of the *expected value* are considered reliable.

1.4. Chapter 1.4: Clarifications and terms

The aim of this chapter is to define geological and microstructural terms used throughout this thesis, and supplementary, to avoid ambiguity on some geological terms that have been defined differently by several authors, and secondly clarify an often used *phrase* in this thesis.

1.4.1. Phrasing

This thesis presents a *case study* of the Ersfjord granite, with the focus on local structures and a small study area. It is by no means meant to explain all the brittle-ductile structures throughout the Ersfjord granite. In this context, the phrase *"in the Ersfjord granite"* or similar phrases is a reference explicit to this study area, and is by no means a collective term, or name for mesoscale- and microscale structures outside the scope of this study.

1.4.2. Tables with terms and definitions

The following two tables presents terms and definitions (table 1-2) used in this thesis, and commonly used mineral abbreviations (table 1-3):

Table 1-2: Terms and definitions used within this thesis, as defined by Passchier et al. (2005), or as otherwise noted.

Term	**Description**
Bulging recrystallization (BLG)	Process of local migration of grain boundary into a neighbouring grain with a higher *dislocation density*, eventually producing new crystals. BLG recrystallization occurs along the edge of older grains
Cataclasite	Rock composed of mainly angular rock- and mineral fragments, formed principally by continued brittle fracturing and *comminution*
Cataclastic flow	Main deformation mechanism accommodating strains above the brittle-ductile transition. Sliding and rolling of fragments
Cemented	Consolidation through mineral precipitation in pores of the matrix
Comminution	Reduction of solid materials from one average particle size to a smaller average particle size by crushing, grinding and other processes. It happens naturally during faulting in the upper part of the crust.
Dislocation(s)	Line defect(s) in a crystal(s), increasing the internal free energy of the crystal(s)

Dislocation density	Total length of all *dislocations* in a volume of material
Ductility	Describes a solid material's ability to deform under tensile stress i.e. being stretched, or malleability i.e. the material's ability to deform under compressive stress without fracturing (see *plastic flow*) and are dependent on temperature and pressure.
Dynamic recrystallization	Recrystallization during *intra-crystalline* deformation (crystalplastic flow); Divided into three regimes (1) Bulging recrystallization, (2) Subgrain rotation recrystallization and (3) Grain boundary migration recrystallization (Hirth et al., 1992)
Fabric	The complete spatial and geometrical configuration of all components constrained in a rock, and that are penetatively and repeatedly developed throughout the volume of rock under consideration. This include features such as foliation, lineation, lattice-preferred orientation and grain size.
Grain boundary area reduction (GBAR)	Migration of grain boundaries leading to reduction in the total surface area of grain boundaries in an aggregate (see *GBM*). The process operates spontaneously in response to the decrease in internal free energy that a grain aggregate gains by decreasing the area of (high-energy) grain boundaries; it leads to straight grain boundaries and large grains.
Grain boundary migration recrystallization (GBM)	The migration of grain boundaries through a solid crystalline material. It is applied to *dynamic recrystallization* were it produces new grains through migration throughout old grains in response to differences in dislocation density between two grains, and to *static recrystallization* were it lowers the internal free energy of crystals.
Matrix	Fine-grained ground mass in a rock, formed by granulation or dynamic recrystallization, filling the interstices between large clasts of original rock
Mylonite	Strongly deformed rock from a *ductile shear zone*, commonly with a planar foliation and usually with a stretching lineation. Usually show high strain fabric, such as quartz ribbons and porphyroclasts in a finer grained matrix. Formed predominantely by crystalplastic flow (see

	dynamic recrystallization) of the matrix, although some minerals suspended in the matrix may show brittle fracturing.
Neocrystallization	Recrystallization of material through chemical change, resulting in new material with different components or crystalline structure
Plastic flow	Continuous ductile deformation without rapture that accommodate strain below the brittle-ductile transition. Dynamic recrystallization and viscous sliding.
Recovery	Process in a crystal or crystal aggregate that leads to a decrease in the combined length of included *dislocations*, and rearrangement of dislocations into subgrain boundaries (see SGR). The process is driven by a decrease in the internal free energy of a crystal or crystal aggregate. Recovery is also active during the process of *static recrystallization.*
Recrystallization	Rearrangement of crystalline matter to a modified set of crystals by migration and modification of grain boundaries. Recrystallization does not necessarily involve chemical changes. It usually involves a decrease or increase in crystal size.
Shear velocity	Defined as the rate of shear deformation, also called friction velocity
Sintering	The formation of a solid mass of material by heat and/or pressure without melting it. Occurs naturally in minerals where atoms diffuse across grain boundaries, fusing the minerals together and creating one solid material
Shear zone	Planar zone of relatively intense deformation in which progressive deformation is *non-coaxial.*
Static recrystallization	General term for post-deformational *recovery* and *grain boundary migration* processes, driven by remaining *dislocations* and a large surface of grain boundaries. It involves *GBAR* and minor *SGR*- and *GBM* recrystallization and recovery, and leads to removal of undulose extinction, straightening of grain boundaries and grain growth
Subgrain rotation recrystallization (SGR)	Rotation of dislocations into planar arrays separating two volumes of crystalline material with the same composition, but with slightly misoriented crystal lattice, resulting in subgrain boundaries. Subgrains rotate with respect to each other and develops into new grains

Ultramylonite	Extremely fine-grained *mylonite* or mylonite with 90-100 vol% matrix and 0-10 vol% porphyroclasts
Undulose extinction	Irregular extinction of a single crystal under crossed polars due to a distorted crystal lattice with high concentration of defects.

Table 1-3: Table with occurring minerals and constituent abbreviation used within this thesis, after Siivola et al. (version 01.02.07)

Mineral	**Abbreviation**	**Mineral**	**Abbreviation**
Albite	Ab	K-feldspar	K-fsp, Kfs
Anorthite	An	Magnetite	Mag
Apatite	Ap	Plagioclase	plag
Biotite	Bt, Bio	Pumpellyite	Pmp
Calcite	Cal	Quartz	Qtz
Chlorite	Chl	Titanite (sphene)	Ttn, Tit
Clinozoite	Czo	White mica	WM
Epidote	Ep	Zircon	Zrn
Hematite (specularite)	Hem		

2. Part 2: Petrography and structures

This part includes all the results obtained during this *case study* of shear zones and cataclasites within the Ersfjord granite. Both descriptions and quantitative results are presented, and builds the basis for a later discussion.

2.1. Chapter 2.1: Introduction

Herein, a description of the Ersfjord granite will be given based on field observations. These observations will be supported by other authors work (Bergh et al., 2010; Romer et al., 1992; Zwaan, 1992b; Zwaan et al., 1998).

Detailed mapping took place north of the town in Grøtfjord (figure 1-3), where shear zones was identified in the Ersfjord granite (figure 2-1). In addition to these shear zones, cataclastic zones were identified adjacent, following strike of the shear zones.

Chapter 2.3 presents the study of 18 thin sections conducted by means of standard microscopic investigation under transmitted and reflected light, and by scanning electron microscope (SEM). Thin sections were all cut parallel to stretching lineation and perpendicular to foliation. The aim of this investigation was to describe the origin and development of the mapped shear zones, with focus on deformation mechanisms, fabric- and textural evolution and strain indicators.

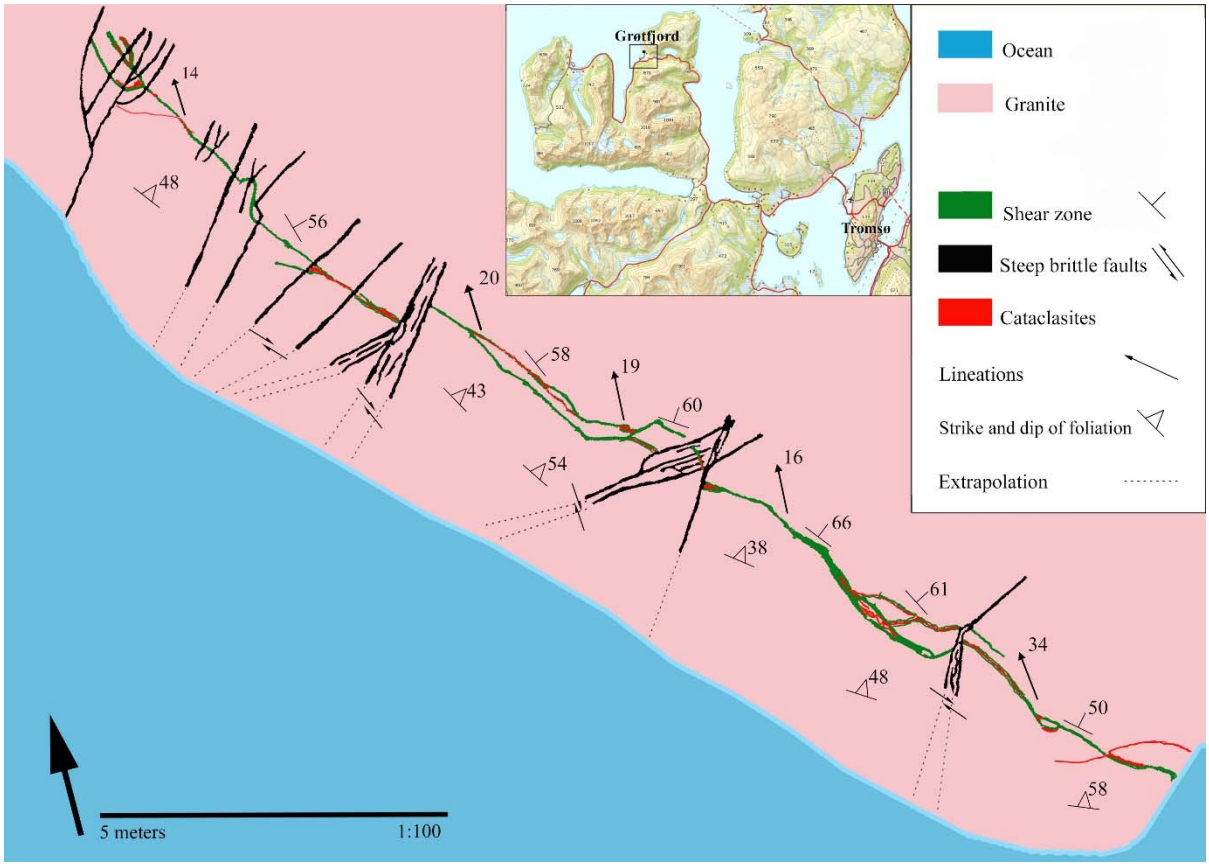

Figure 2-1: The lithologic map created from extensive mapping of the shear zones and associated structures. The general trend of the shear zone is NNW-SSE. The cataclasites dominantly follows the strike/dip of the shear zones and foliation. ENE-WSW steep brittle structures truncates the ductile and cataclastic fabric.

2.2. Chapter 2.2: Field observations

2.2.1. Host rock and fabric

Red-colored granite define this locality, with WNW-ESE striking shear zones and cataclastic zones, a NW-SE trending foliation, and NE-SW conjugated steep brittle faults that truncate the ductile- and the cataclastic fabric. This study is limited to the shear zones and cataclastic zones. The locality comprise of only one lithology, the Ersfjord granite (section 1.2.3.1), which regionally is very homogeneous, but approaching the lithologic contact towards the Kattfjord Complex (i.e., c. 50m north) the rock show signs of alteration, brittle fracturing, and development of foliation. These observations are in accordance with what Bergh et al. (2010) reported when approaching the contact zone.

The Esfjord granite is commonly characterized, either as a light colored, unaltered rock with a clear magmatic texture, or as a distinct red-colored altered rock abundantly crosscut by brittle

fractures. It is mainly relatively coarse grained with 5-15 mm large elongated phenocrysts of K-fsp that are stretched parallel with lineation. The main minerals which can be observed with a hand lens are K-fsp phenocrysts, diffuse plagioclase and quarts aggregates and ribbons. Less abundant minerals are biotite, titanite, calcite and zoizite. Another mm-sized dark mineral occurs scattered through the bulk rock, and is identified as magnetite due to its magnetic signature. Chlorite, epidote and hematite occurs abundantly within shear zones and cataclastic zones. Hematite is also present on fracture planes. These fractures might be related to cataclastic zones because some contain rock fragments.

Most of the exposed granite has undergone some degree of strain, which is apparent from the WNW-ESE foliation (figure 2-6 A-ii), however, there are parts of the granite that show a lower degree of alteration. These parts lay a couple of meters from strain localizations, such as shear zones (figure 2-2 A). It is a homogenously distributed foliation, defined by single shear bands of 3-5 mm with centimeter spacing (i.e., 1-2 cm) between the bands. When looking perpendicular (figure 2-2 B) or parallel (figure 2-3 B) to foliation, near a shear zone, it is clear that the shear zones had a drastic effect on the host rock. The abundance of alteration products (e.g., ep, chl and wm) have increased drastically. Thickness of the shear bands have increased, and thus the mechanical strength of the rock seem to have decreased. A few effects of this alteration is observed in the form of (i) a redder granite, which may be because of hydrothermal alteration, (ii) a decrease in k-fsp and (iii) a change from magmatic to gneiss texture.

The main fabric of the Ersfjord granite contains K-fsp phorphyroclasts enclosed in elongated grains of quartz, epidote, chlorite and micas to form the gneiss texture. Each foliation band produces some offset due to the strain, multiplying this up over a zone of c. 7-8 meters adds up to a significant deformation of the igneous texture. The observed ductile fabric was likely produced while the host rock still was in the ductile regime (e.g., the temperature was high enough not to cause brittle failure). Later, brittle fabrics that truncates the ductile fabric are present, in form of faults and fractures (figure 2-2 B and 2-4 A). The apparent conjugated set of brittle faults form an ENW-WSW brittle system (figure 2-6 C), which displaces the main ductile shear zones.

Figure 2-2: A digital photograph of the host rock. (A) Field appearance of the mostly unaltered rock, the picture is taken a few meters from a shear zone. Red 5-15 mm K-fsp phenocrysts are seen, where white areas are plagioclase and quarts. The foliation bands contains abundant epidote, quartz and chlorite and accessory minerals. Marker=14 cm. (B) A close-up viewing near perpendicular to foliation near a shear zone. The bands are thicker and contains more alteration products. Compass plate=10 cm.

2.2.2. Mesoscopic structures

Mesoscopic structures observed in the Ersfjord granite (1,79 Ga) are ductile, have WNW-ESE striking foliation with a mean dip of 54° (figure 2-6 A-ii) and are presumed to be of Svecofennian age. Foliation bands increase in abundance towards the shear zones (figure 2-3 B), where each foliation band seems to have acted as a local shear plane causing some strain on the bulk rock. This resulted in weaker zones where the abundance of matrix is increased (i.e., ep, chl, qtz, ab and wm). The foliation is partly truncated, and likely reactivated by the ductile strain localization which caused 5-20 cm wide NNW-SSE shear zones with a mean dip of 57° (figure 2-6 A-i). To the NE of the main shear zone, a second shear zone is located, which show the same characteristics (i.e., strike, dip and kinematic signature). The dip of the shear zones appears to follow the preexisting gneiss foliation (figure 2-3 B & figure 2-4 A). The higher strain concentration seems to have caused the damage zone surrounding the main shear zone and extends outwards for 10-15 cm (figure 2-3 B), then subsides to the regular foliation observed throughout the host rock. In the main shear zones, towards the core, the abundance of k-fsp, plag and quartz seems to have been reduced and replaced with abundant ep, chl and white mica forming the matrix. Still, recrystallized qtz, and some Ab and K-fsp occurs.

Faults and fractures truncate the shear zones and the granite shows local signs of alteration, mainly along these brittle faults and ductile shear zones. The shear zones change characteristics along strike, from mostly mylonitic, to cataclastic (figure 2-4 B). All around the main shear zone, smaller zones of cataclastic material are located, which seems to partially follow foliation and partially to truncate it. From studying the brittle structures, two different cataclasites have been observed. They are distinguished by the amount of matrix and the clast size. The first event hosts big angular clasts inside less than 50% matrix by volume and the second contains small clasts within more than 90% matrix by volume. From mesoscopic observations it is difficult to distinguish the two events, but it is possible to infer a crosscutting relationship, where the matrix-poor event is infiltrated by the matrix-rich event (figure 2-5 B).

Antonsdóttir (2006) studied the Rekvika fault zone and identified ENE-WSW striking brittle faults (S_1) in the Grøtfjord area that runs parallel with the Rekvika fault zone, a few km further north. The ENE-WSW brittle structures observed (figure 2-6 C), in this study area (figure 2-1), seems to truncate the foliation, ductile shear zones and cataclasites (figure 2-2 B, 2-3 A, 2-4 A), thus indicating a later affinity than the observed ductile and cataclastic structures. In Grøtfjorden the ENE-WSW brittle structures (figure 2-6 C) have approximately the same

strike/dip and striations (not measured, but observed) as the ones measured in Rekvika by Antonsdóttir (2006), were the biggest difference is a slight rotation towards east with a steeper dip angle.

Figure 2-3: (A) An overview look of a shear zone that slightly turncates the foliation and readly alteres the host rock. The black band that follow the strike of foliation is a cataclasite filled with hematite. The abrupt cut, marked with the black border and half-arrow, are the result of a ENE-WSW brittle fault. (B) Profile view across a shear zone (masked out black area) and cataclastic zone (stippled area; footwall). Dip of the shear zone and cataclastic zone follows the same dip as foliation. The hanging wall have a strongly sheared damage zone of approximately 10-15 cm (stippled area; hanging wall). As moving outwardly from the shear zone, the foliation is subsiding to a minimum.

Figure 2-4: (A) The main mylonitic fabric of a shear zone with abundant Ep, Chl, and WM (stippled area). The black zone in the middle of the shear zone, following strike and dip, is a cataclastic zone. The black half-arrows and the black lines represents the ENE-WSW steep brittle faults. (B) Digital close-up of the mylonitic fabric, inside a cataclastic matrix.

Figure 2-5: (A) Photograph of a qtz vein dextrally displaced by a series of thin fractures. (B) Close up of two different cataclasites: (1) The black stippled area of the picture contains big clasts of host rock and less matrix (matrix-poor). (2) The left part contains smaller clasts and a major amout of matrix (matrix-rich). The foliation bends avay from the main zone on each side, indicating a dextral shearing during movement. Marker=14cm.

2.2.3. Mesoscale kinematic data

Kinematic data have been gathered from orientation data of structures in connection with mineral stretching lineation on shear planes. This data have been used to plot slip-linear stereographic projections (Goldstein et al., 1988) and will be presented here in conjunction with mesoscopic- and microscopic observations.

All of the mineral striations gathered are from the mineralization of mica on shear planes. These secondary minerals form striations parallel to the movement direction, and are as such ideal for obtaining kinematic data. They record only the latest movement and are, combined with shear sense indicators, considered reliable for kinematic studies. The lineations measured have a gathered trend and dip (figure 2-6 B-i-ii), and therefore the sense of slip seems to have been consistent along strike of the shear zones. Lineations from mica striations within the main ductile shear zone were measured and these measurements were used to construct a slip-linear plot for the shear zones (figure 2-6 B-ii). The slip plot suggests an oblique-dextral strike-slip motion; this is supported by the results of the microscopic study of shear sense indicators presented in section 2.4.1.

A centimeter thick and meter long NE-SW striking quartz vein cuts through the foliation and are displaced by a series of thin fractures (figure 2-5 A). The data suggest a dextral strike-slip movement, with top-to-the SW.

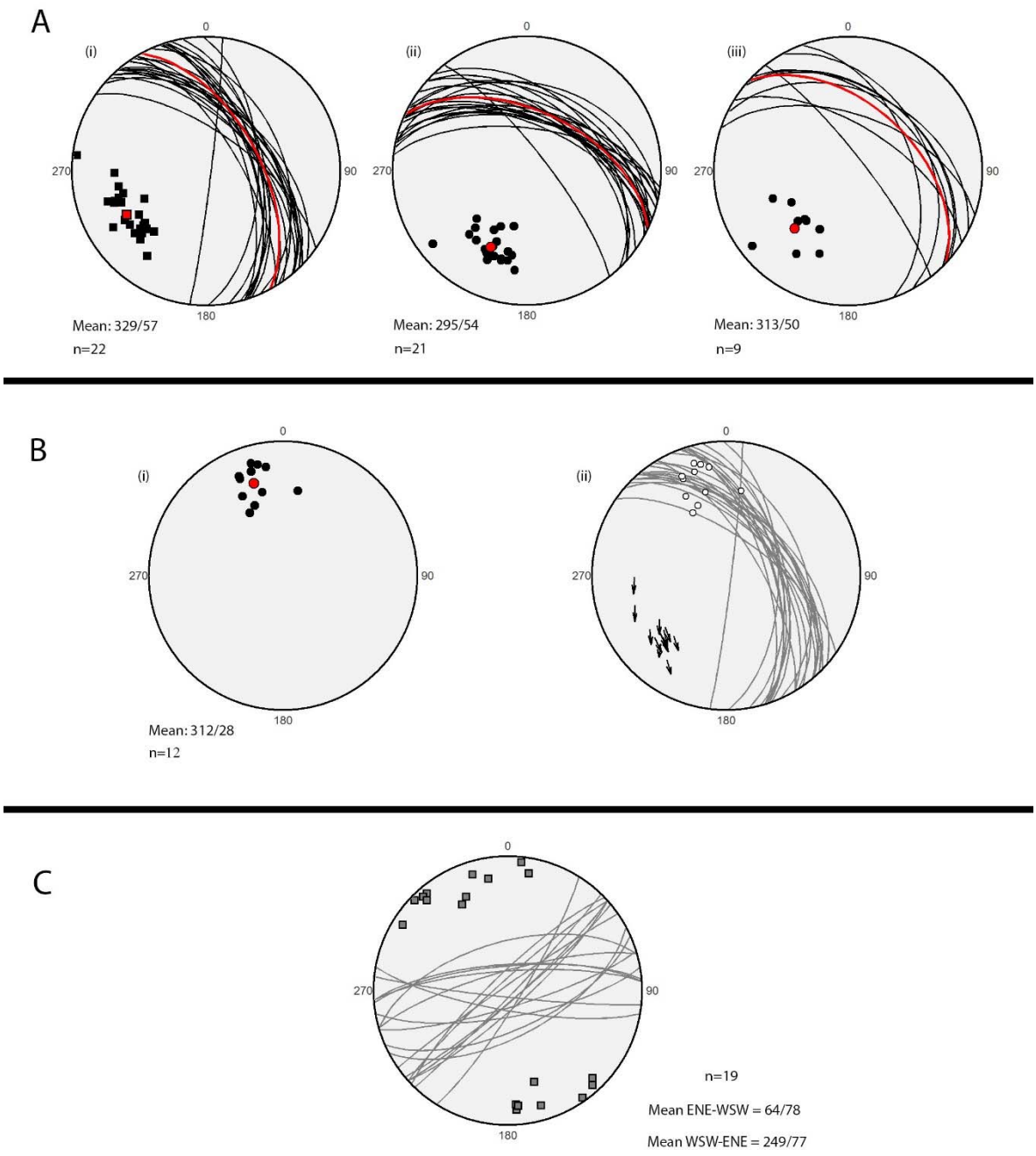

Figure 2-6: Lower hemisphere Schmidt stereo nets of structural elements observed in the Ersfjord granite. The planar elements are plotted following the right hand rule and linear elements are plotted as trend/plunge. (A) The recorded planar elements, where the red data represents the mean value (i) Strike/dip of the main ductile shear zones projected as great circles and poles, (ii) observed foliation of the Ersfjord granite and (iii) recorded strike/dip of the cataclastic zones. (B) Lineations and constructed slip-linear plot. (i) Recorded lineations of the main shear zone. Red circle represents the mean lineation direction of 312/28 out of 12 measurements. (ii) Slip-linear plot constructed using lineations and shear sense indicators obtained, confirming a dextral shearing. (C) Steronet plots of the latest steep brittle faults that truncates the preexisting fabric. This is a conjugated set that forms small graben structures and displaces the ductile shear zone.

2.3. Chapter 2.3: Mineralogy and microstructures

This chapter describes micro fabrics of the Ersfjord granite with emphasis on the deformation structures described in the previous chapter (2.2). Firstly the mineral assemblage will be studied, both for the less deformed areas and for the strain localized areas. Then a microstructural description for the cataclasites will follow. The last part of this chapter will focus on the fabric relationships and deformation mechanisms.

Mineralogy is an especially important element to describe since it can shed light on the crystallization process which created certain mineral assemblages, or alterations to other phases, and stability fields for bulk compositions. For example, these observations can be related to the P-T paths of the rock, since each composition have its own distinct stability field during metamorphism (Spear, 1995). Microstructures such as micro cracks, deformation lamella- and twins, σ- and δ-clasts, "fish-structures", micro folds and S-C fabric are studied using optical microscopy and SEM, and later set into context with the deformation history.

2.3.1. Micro-fabrics of the Ersfjord granite

During the microscopic study, the thin sections were divided into three groups based on the most dominant observed fabrics. Table 2-1 presents the divisions. The foliation is distributed throughout the locality but shows decreasing intensity outwards from the high-strain ductile shearing. Shear planes have cm-scale thicknesses and cm spacing between the bands. The fabrics are divided with respect to the distribution and the intensity of the foliation. *Mylonitic fabrics* occur as 15-20 cm wide zones of fused, concordant foliation bands 1-2 cm wide, each of which is made up of a series of articulated shear zones with lengths of 1-4 meters (figure 1-2). In the *foliated fabrics* the shear planes are not fused together, but occur with cm-spacing between them. The *ductile fabrics* are found in the samples dominated by microstructures which reflect a lower degree of deformation, which seems to occur towards the margins of the distributed foliation. The fabrics are correlative with the positions of the samples within the field area; samples from the shear zones display mylonitic fabrics while samples from the foliated zone display foliated fabrics which grade outwardly to ductile fabrics at the margins of the foliated zone. The mylonitic fabrics, including foliation fabrics are described in section 2.3.2.

Table 2-1(Next page): Table presenting the division of the studied thin section based on observed structures from outcrop and during microscopic study, and dominant microstructures present in each thin section.

Ductile fabrics	Foliated fabrics	Mylonitic fabrics
DP07_1	DP01_2_3_4	DP01_1[2]
DP11_1	DP02B_1_2	DP06A_1
DP02C_3	DP02C_1_2	DP10A_1
	DP09_1_2_3	DP12_1_2_3
[2]Highly foliated → transition to mylonites		

2.3.1.1. Ductile fabrics

K-feldspar (~50%)

K-fsp occurs as 12-15 mm sub- to anhedral inequigranular grains (figure 2-8 A, E, G). The mineral is colorless, biaxial, show 1st order white birefringence and 2Vx angles varies from 50-60°. The undulatory extinction is evidence for dynamic recrystallization. The old grains show abundant healed microfractures (figure 2-16 E-H). These fractures seems like they are hydrothermal fractures due to a new precipitated mineral phase (Chl). K-fsp also show perthitic exsolution due to the significant difference in ionic radii of Na^+ and K^+ (1,32 versus 1,65 Å, respectfully) (figure 2-8 A, G). On cooling, after crystallization, the amount of Na^+ permissible in K-feldspar structure and K^+ permissible in albite both decrease (figure 2-7). As a result, domains of albite nucleate to take up excess Na^+. Formation of albite domains within the K-fsp only requires diffusion of Na^+ into those domains and migration of K^+ out, because the crystal structures are essentially the same. For instance, homogeneous Kfs [$Ab_{40}Kfs_{60}$] at 700°C is stable, because it lies outside the solvus. Following the path (arrow) this composition begins exsolution at 590°C. The first exsolved Albite is $Ab_{85}Kfs_{15}$. At 500°C Kfs composition is $Ab_{28}Kfs_{72}$ and the Ab composition is $Ab_{93}Kfs_{7}$. The requirement for ions to migrate through the crystal lattice tells us that this procedure is temperature and time dependent. Based on the well-developed perthitic texture, slow cooling of the granitic body i.e., either a deep-seated intrusive or a later regional metamorphic event. K-fsp occurs in a few different settings:

1. With poikilitic textures e.g., with white mica, quartz or plagioclase
2. As a breakdown to sodic plagioclase, creating symplectite of vermicular quartz (Myrmekite)
3. As dynamic recrystallized grains with cross hatched twins and straight extinction

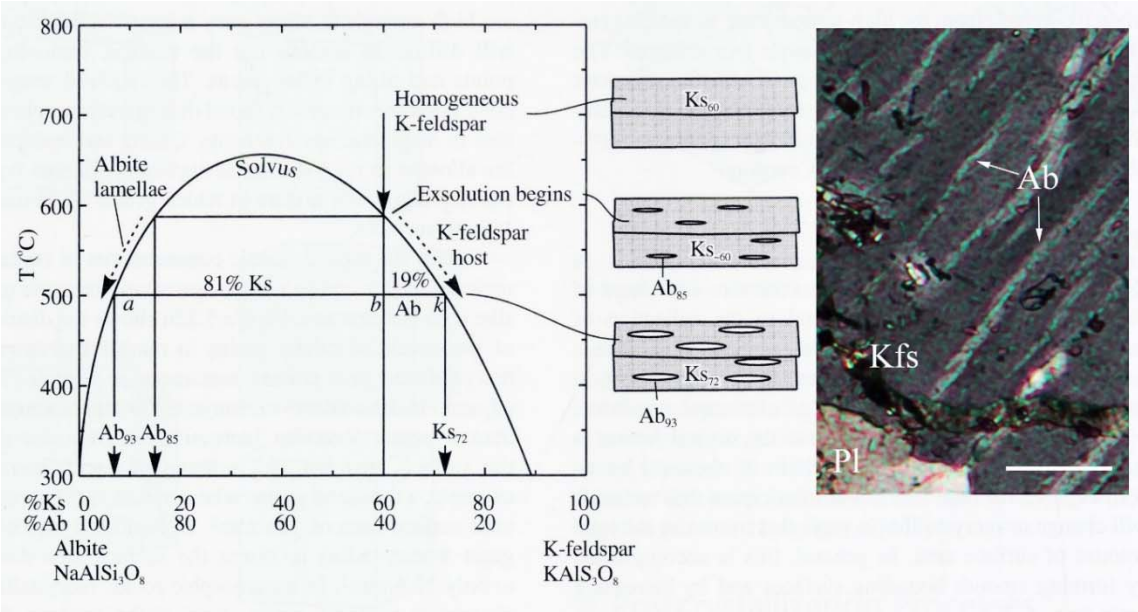

Figure 2-7: Exsolution in alkali feldspar as a function of modal amount for Kfs and Ab. As shown in the picture to the right: Ab lamella within a Kfs grain, as a result of exsolution. Scale bar=500µm. After Smith et al. (1974).

Plagioclase (~15-20%)

Occurs as subhedral 7-9 mm inequigranular grains. The mineral display no pleochroism, is biaxial, with 1st order with/gray birefringence, low relief and inclined- to undulatory extinction. $2V_x$ angle varies from 55-75°. The majority of plagioclase grains show a poikilitic texture with white mica intergrowths, which is a sign of alteration. Plagioclase occurs in a few different combinations (figure 2-8 A, D, E, G, H):

1. In symplectite replacing K-fsp
2. As symplectites with vermicular quartz and K-fsp
3. It occurs as remnant phorphyroclasts in the matrix
4. As dynamic recrystallized grains within the matrix

Quartz (~15-20%)

Quartz is a colorless mineral that occurs, in the Ersfjord granite, as sub-anhedral inequigranular 0,3-0,4 mm grains (figure 2-8 B). Quartz is uniaxial (+) with low relief, low birefringence and no cleavage. The crystals show patchy to undulatory extinction which is a sign of different dynamic processes. The quartz aggregates forms a polygonal-to-interlobate grain boundary geometry, with diffuse grain boundaries (figure 2-8 B-C). The diffuse grain boundaries observed in the optical microscope may be recrystallized grains that are too small to observe. Hirth et al. (1992) conducted a TEM analysis on quartz and identified the responsible

mechanism for the diffuse grain boundaries as strain-induced grain boundary migration. The aggregates itself are slightly elongated, at an angle to foliation and appears in different textural settings:

1. As vermicular qtz in myrmekites
2. As slightly elongated aggregates with decreased grain size at an angle to foliation bands
3. Or as the less deformed, bigger aggregates.

Chlorite (~5%)

In this study, chlorite occurs as fibrous subhedral to acicular 0,15-0,25 mm grains. The mineral is strongly pleochroic, has moderately positive relief, and the color reflects whether it is optically positive or negative, where the optically positive grains appear pale green to light yellow with brown interference. Optically negative grains appear pale green to yellowish green with anomalous weak blue to purple interference colors. Chlorite usually appears as elongated aggregates along fractures, but can be found as sympectites with epidote and titanite as well, maybe from the breakdown of biotite (figure 2-8 D). It also occurs as infill within fractures in K-fsp phorphyroclasts (figure 2-16 E)

White mica (~5%)

The abundance of white mica reflects the breakdown of K-fsp and plagioclase. White mica occurs as subhedral acicular inclusions in the feldspars. The inclusions are randomly distributed and contributes towards weakening of the fabric. The micas are especially abundant within foliation bands, where it locally can be up to ~20-30% of this phase.

Epidote (~3%)

This mineral is recognized by the light yellowish green pleochroism, one good cleavage, and chemical zonation. The mineral is biaxial (-) with moderately high birefringence and moderate relief. The mineral occurs as sub- to euhedral 0,1-0,2 mm grains and occurs in association with chlorite and are abundant in the more deformed areas (figure 2-8 D).

Biotite (<1%)

Almost the entire phase is altered, but there are still a few relict grains left. Biotite occurs as pale brown to reddish brown euhedral grains (figure 2-8 D). The mineral is biaxial (-), $2V_x$

angle of 16°, moderate relief and yields high interference colors in the 3rd or 4th order, but are masked by the pleochroism. Biotite has a single cleavage plane running along its long axis, parallel to foliation. Based on the symplectite with epidote and the abundance of both chlorite and titanite around scattered biotite minerals, these are most likely alteration products.

Opaque minerals (<0,5%)

Idiomorphic crystals have grown on top of the earlier fabric. Because the foliation never bends around the idiomorphic crystal, it can be inferred that the opaque phase has formed post-deformation. The grains are interpreted as magnetite with intra crystalline hematite. This is supported by the magnetic signature of these crystals (figure 2-8 F). The hematite may have formed as the result of oxidation on the grain boundaries and along fractures.

Accessory minerals

Titanite occurs as sub- to anhedral grains with a brown color (figure 2-10 D). The mineral is biaxial with a very high relief and an extreme birefringence, but the color can be masked by pleochroism. Titanite shows signs of chemical zoning as the extinction angle changes across the grain.

Figure 2-8 (Next page): Microphotograph of the mineral assemblage showing the ductile fabric. (A) Symplectite between K-fsp and vermicular quartz intergrowths in plagioclase. Wihite mica is growing within plag due to chemical disequilibrium. Scale bar=1mm. (B) Quartz aggregate with dominating subhedral and anhedral grain boundaries, with signs of straight grain boundaries. Arrows point toward subgrain boundaries. Scale bar=1mm. (C) Anhedral qtz grains with lobate grain boundaries. Arrows point towards a subgrain boundary. Scale bar=100µm. (D) Plagioclase and biotite breakdown to form white mica, epidote and chlorite. Scale bar=1mm. (E) K-fsp grain with mobile subgrain boundary. Myrmekite intergrowths with plag, and on the opposite side plagioclase replacing k-fsp. Scale bar=1mm. (F) Micrograph of the syn-deformational opaque phase with magnietite and heamatite along narrow zones. Scale bar=100µm. (G) K-fsp grain being replaced with plagioclase containing vermicular quartz intergrowths. White mica are aligned in narrow zones. Scale bar=1mm. (H) Plagioclase grain with slightly rotated and bent twins surrounded with small grains of recrystallized plagioclase and k-fsp. White grains are quartz. Scale bar=1mm. Crossed polars on all micrographs.

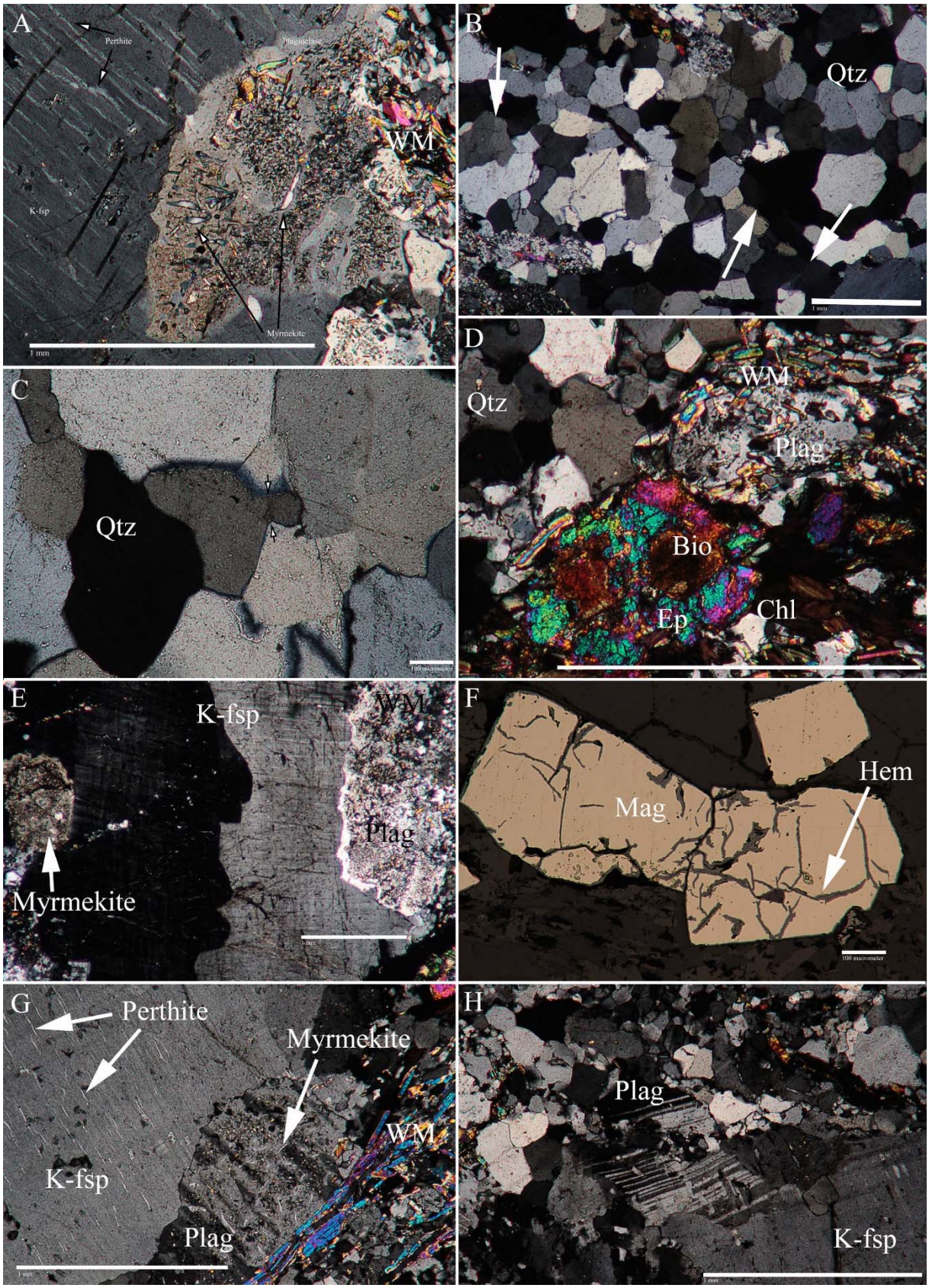
A
Perthite
Plagioclase
WM
K-fsp
Myrmekite
1 mm
B
Qtz
1 mm
C
Qtz
100 micrometer
D
Qtz
WM
Plag
Bio
Ep
Chl
E
K-fsp
WM
Plag
Myrmekite
F
Hem
Mag
100 micrometer
G
Perthite
Myrmekite
WM
K-fsp
Plag
1 mm
H
Plag
K-fsp
1 mm

2.3.1.2. Foliated fabrics

K-feldspar (~15-20%)

This mineral occurs as anhedral inequigranular disseminated 1-1,5 mm grains (figure 2-10 A-B). K-fsp is colorless with low relief and low birefringence showing 1st order white, $2V_x$ angle of 60-70° and has an undulatory extinction. The sub- to anhedral recrystallized grains show good developed cross hatched twins, straight extinction and a $2V_x$ angle of 50-70° with a grain size of 0,1-0,15mm (figure 2-10 D). Some of the biggest k-fsp grains do not show cross hatched twins, but well-developed perthitic textrure, whereas others show well-developed cross hatched twins. This suggests that exsolution (figure 2-7) and Al/Si ordering have taken place. Most K-fsp (excluding hydrothermal growth and diagenesis) crystallize with a Sanidine structure and the highest degree of disorder in the distribution of Al and Si in the tetrahedral sites. As the rock cools the ions progressively migrate through the lattice and ultimately place all Al^{3+} in just the T_{1o} site, all the Si^{4+} is occupied in the T_{1m} and T_2 sites. This process distort the monoclinic lattice – at roughly around 450°C – so all microcline is triclinic, therefore all microcline produced by this process displays a combination of polysynthetic albite and pericline twinning. Considering the $2V_x$ angles combined with the exsolution and order/disorder, the K-fsp are probably a combination of intermediate orthoclase and maximum-intermediate microcline. This indicates that the rock has been subjected to an extended period of slow cooling, and/or regional metamorphism at a later stage. The mineral occurs in different textural settings:

1. With lobate grain boundaries to symplectic plagioclase
2. As relict myrmekite and "old" mozaic grains
3. As new recrystallized grains

Plagioclase (25-30%)

Plagioclase is colorless, biaxial, has low relief, low birefringence with 1st order gray or white colors and a $2V_x$ angle of 60-70°. The 0,6-1 mm grains are sub- to anhedral with good cleavage and inclined- to undulatory extinction. The recrystallized 45-50 µm grains are euhedral- to subhedral with straight extinction, $2V_x$ angle of 60-70° and show a slight elongation parallel to foliation.

1. Plagioclase is replacing K-fsp
2. Occurs as mozaics of old grains with intragranular white mica and epidote
3. And as recrystallized new grains

Figure 2-10 C shows a plagioclase phorphyroclast with intragranular synthetic sinistral microfractures which displace the twins. The tail extending to the upper right shows recrystallized albite indicating dextral shear. A second plagioclase grain (figure 2-10 D) shows chemical replacement by white mica, due to intragranular chemical disequilibrium.

Quartz (15-20%)

The mineral shows no pleochroism, is uniaxial (+), has no cleavage and low positive relief. The 0,2-0,4 mm grains are sub- to anhedral and form elongated equigranular polygonal-to-interlobate grain aggregates parallel to foliation (figure 2-10 F) Quartz occurs in diverse textural settings:

1. As bands with a thickness of one grain and as boudins
2. As slightly elongated monomineralic aggregates
3. As recrystallized zones within the matrix showing distinct shape preferred orientation (SPO)

Foliation (30-40%)

This category lists the minerals present in the foliation, which is a mylonitic to ulramylonitic fabric. See section 2.3.2 for a description.

1. 50-70% Epidote
2. 10-30% Quartz±feldspar
3. ±10% Chlorite
4. ~10% white mica

Chlorite (3-4%)

Chlorite is pale green to light yellowish pleochroic, with low birefringence showing 1st order brownish color. The subhedral to acicular grains form thin bands parallel to foliation, or occurs with radial growth patterns, which may suggest that they grew within open pore spaces (figure 2-10 G).

Accessory minerals (1-2%)

Titanite is yellowish brown and occurs as subhedral, wedge formed, crystals. It has a very high positive relief, is biaxial (+) and show extreme birefringence, but interference colors may be

hard to detect due to mineral pleochroism. This mineral seems to readily alter to leucoxene along grain boundaries, which is mainly titanium oxides±qtz±Ep±others (figure 2-10 D-E).

Using the EDS it was possible to identify scattered pumpellyite, zircon (figure 2-9) and apatite.

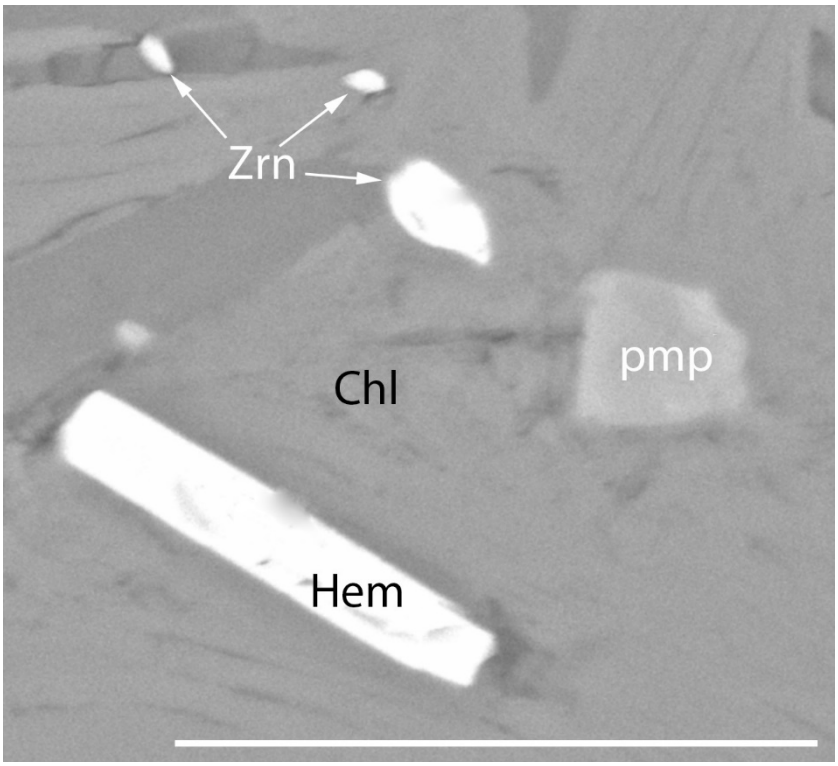

Figure 2-9: EBSD image from a cataclastic zone that cuts through the ductile fabric. Inside the cataclasites a pumpellyite (pmp) grain was identified, surrounded by chlorite. Small zircon (Zrn) grains was also identified. Hematite is the bright area (Hem). Scalebar=25µm. Sample DP12_2.

Pumpellyite

The mineral (figure 2-9 and 2-13) is associated with anomalous green pleocroism with similarities to chlorite. With the optical microscopy it was not possible to see the mineral, but instead favorable locations for it to occurr were identified, such as cataclasites and areas with fluid infiltration. The identification were carried out with BSD-analysis as described in section 1.3.4.1, where the spectrum and the crystal structures are presented in the appendix.

Opaque minerals (<0,5%)

Idiomorphic crystals of syn-deformational growth. They are mainly magnetite, but show an optically red stain along edges, which is a sign of present hematite.

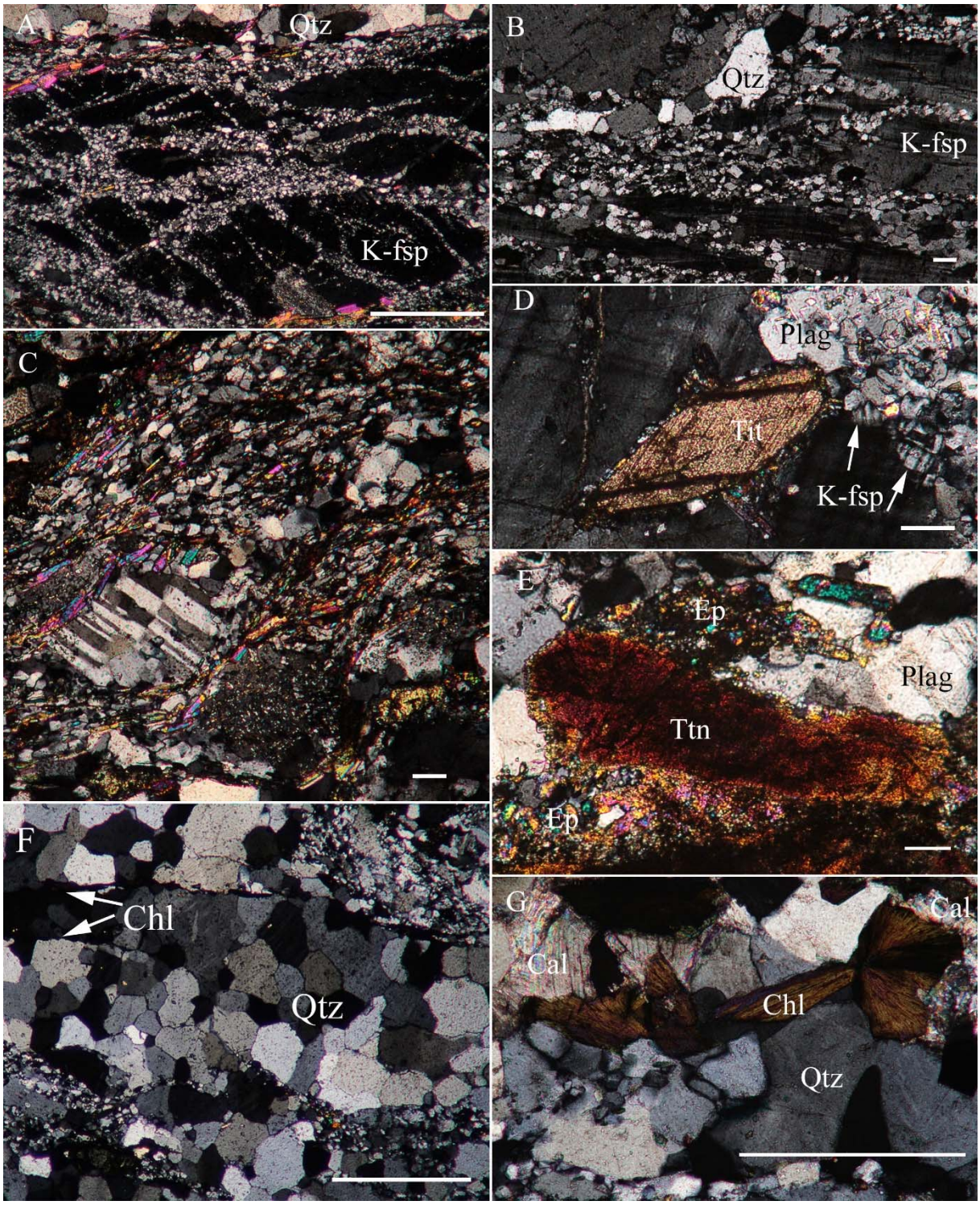

Figure 2-10: Micrograph of foliated assemblages. (A) Disseminated K-fsp phorphyroclast with sections of fine grained albite + quartz domains resulting from neocrystallization. Scale bar=1mm (B) Close up of A; fine grained mosaic of Qtz + Ab. Growth of large Qtz grains. Scale bar=100µm. (C) Twinned plagioclase clast with transverse offset of internal twin boundaries corresponding to displacement along several transgranular fractures, followed by a tail of recrystallized grains. Clasts showing dextral sense of shear. Scale bar=100µm. (D) Chemical breakdown of a Titanite grain within a K-fsp phenocryst in association with plagioclase, precipitating small Epidote grains (sharp colours). Arrows points to dynamic recrystallization of K-fsp. Scale bar=100µm. (E) Chemical breakdown of titanite and plagioclase producing epidote. Scale bar=100µm. (F) Slightly elongated polygonal qtz aggregate with chlorite precipitating parallel to foliation. To some degree the qtz grains exhibit straight grain boundaries. Scale bar=1mm. (G) Radial growth of Chlorite and growth of calcite within a qtz aggregate. Scale bar=100µm.

2.3.2. Ductile Shear zones

Deformation in rocks are not homogeneously distributed. The concentration of strain in planar zones that accommodate movement of relatively rigid wall-rock is the most common pattern of heterogeneous deformation. Strain localization happens because there is a change (e.g., fractures, mineralogical, fluids or grain size reduction) in the host rock resulting in weakening of the rock (Passchier et al., 2005). In initially homogeneous media, shear deformation localizes only when the material supports lower stress with increasing deformation (strain softening). Strain, strain-rate or thermal softening may cause this stress decrease. Changes in deformation mechanisms induced by progressive changes in fabric, microstructure, or composition may permit localization of shear strain (Segall et al., 1986). Deformation in such zones usually contains lateral displacement of wall rock segments with respect to each other. This type of strain localization is known as a shear zone. Geologically, these zones are an important source of information due to the development of characteristic fabrics and mineral assemblages that reflect P-T conditions, flow type, movement-sense and deformation history.

The studied shear zones exhibit signs of later reactivation. The granitic fabrics of high grade microstructures such as symplectites (e.g., myrmekite, dynamic recrystallization and mixing of mineral phases) are common in deformed domains. As strain localizes, foliation gradually intensifies and/or propagates along pre-existing weak zones, into a mylonitic fabric. As time passes, temperature drops and there is a cataclastic event along the earlier formed shear zones. The evidence for a reactivation event is pre-existing foliation inside the cataclasite, with the same mineralogy as the mylonites.

The sense of shear was mesoscopically deduced (2.2.3) from a cm-thick quartz vein that was cut by an mm-thick shear zone and dextrally displaced (figure 2-5 A). This observation was backed up by later microstructural evidence (2.4.1)

2.3.2.1. Mylonites

The terms *mylonite* and *ultramylonite* are strictly structural terms that only refer to the fabric of the rock, and does not give any information on the mineralogical composition. The two different terms are based on modal amounts of matrix, where the latter contains 90-100 vol-% matrix and 0-10 vol-% porphyroclasts. A *mylonite* is a foliated and usually lineated rock that show strong ductile deformation.

In the Ersfjord granite localization of high-strain zones are similar to *mylonite zones* and *mylonitic shear bands*. Usually the contact between a mylonite zone and the wall rock is gradual, but along strike the gradation changes from being abrupt to gradual. This may reflect the possibility that the shear zones propagated along pre-existing heterogeneities (Segall et al., 1986).

Grain sizes observed in the mylonite is usually smaller than that of the wall rock. This may be caused by different mechanisms that accommodates crystal-plastic deformation (2.3.4). Mineralogically the mylonitic- and foliation fabrics are very similar, where the main difference is the abundance of matrix, and the slight difference in grain size. The euhedral-subhedral epidot grains in these assemblages are ~13-18 µm. They show a pale green yellowish pleochroism, and the small grain size preclude observing cleavage, which usually is 001 perfect.

The colorless subhedral-anhedral quartz aggregates are stretched foliation parallel, with straight extinction in new grains and grain sizes varying from 2 orders of magnitude bigger than the epidote grains. These monomineralic quartz aggregates appear as elongated lenses and bands which are fully recrystallized. At a certain point, the aggregates become so long that their area cannot be measured in a single thin section. The width of the layers can decrease to a thickness of a single grain. In the most strained areas the quartz grains within aggregates have an oblique shape preferred orientation (SPO) indicating dextral shear sense (figure 3-4 D). In the low strain areas of the shear zone, where quartz grains have undergone less deformation, they show optically visible subgrains, but this feature is less prominent in the high strain areas and recrystallized qtz grains usually do not show undulatory extinction (Kilian et al., 2011).

K-fsp and plagioclase are nearly completely recrystallized to epidote, chlorite, quartz and white micas, whereas the old fractured grains show big Albite lamella, which reflect the exolution process creating the perthitic texture. Porphyroclasts throughout the matrix is common, which are remnants of resistant mineral aggregates of a size larger than the grains in the matrix. The developed foliation wraps around porphyroclasts which usually creates σ-clasts that can be used to infer sense of shear (figure 2-10 C and 2.4.1). Differences in rheology between constituent minerals; relatively hard minerals forms porphyroclasts, while soft ones form part of the matrix (Passchier et al., 1986; 2005). Magmatic plagioclase in the protolith is pseudomorphically replaced by fine grained plagioclase (Ab and Oligoclase) intergrown with minor amounts of white mica and epidote. Undeformed plagioclase aggregates are consistently intergrown with

white mica along the cleavage direction. With the onset of deformation, the white micas seems to align parallel with shearing (Kilian et al., 2011).

The matrix of the mylonite consists of epidote, quartz, chlorite, white mica and with accessory plagioclase and k-fsp, calcite, titanite and opaques; the grain size of most phases is <20 µm, which is considered to be the equilibrium grain size. The different phases in the mylonite are not homogeneously mixed. A layering consisting of mixed phases can be observed. Fine grained plagioclase (Ab) and to a variable degree of recrystallized k-fsp are mixed with epidote, chlorite and quartz. Non-recrystallized K-fsp clasts are rarely preserved in the most deformed areas.

2.3.3. Cataclasites

Cataclasites are formed by brittle fracturing and comminution during faulting and are divided into incohesive- and cohesive cataclasites. Incohesive cataclasites usually occurs in faults that have been active at shallow crustal levels where the wall rock and included fragments commonly show polished surfaces (i.e., slickensides and slickenfibres), which can be used to determine movement direction and shear sense. The cohesive counterpart of the rock is due to crystallization of minerals along the fracture planes (e.g., precipitation from a fluid). Commonly observed minerals include quartz, epidote, calcite and chlorite; or k-fsp if a fluid solution is highly alkaline. The k-fsp only crystallize if fluid infiltration into a freshly comminuted rock is limited. These metamorphic rock types are usually subdivided on the basis of the relative abundance of matrix:

1. Protocataclasite: Matrix takes up less than 50% of the total volume
2. Mesocataclasite: The matrix occupies between 50 and 90% of volume
3. Ultracataclasite: More than 90% matrix

Fragments of all sizes occur in the Ersfjord granite, from sub mm- to cm scale, where the smallest grains are rounded and the bigger grains are angular. Cataclasites usually show a gradual transition of decreasing brittle deformation intensity distal to the core zone. A very abrupt decrease in brittle fracturing intensity is observed along strike, from only 40-50µm width up to 1-2 mm, depending on which mineral aggregates are adjacent to the cataclastic zone (figure 2-12 A). The damage zone contains a mass of fractured and partly ductile fabric, where initiation seems to have happened by brittle fracturing and infiltration of fluids which initiated dynamic recrystallization along the, now healed fractures. Adjacent quartz aggregates exhibit

the thinnest damage zones, where feldspar aggregates shows the widest. This is due to the mechanical strength of minerals at low temperatures (figure 2-11). Around 350-300°C qtz aggregates becomes stronger than feldspar aggregates and both deforms by brittle fracturing. One possible explanation for this is that feldspar grains have cleavage planes that reduce its strength. This observation suggests that at least one catclastic event occurred in the lower greenschist facies.

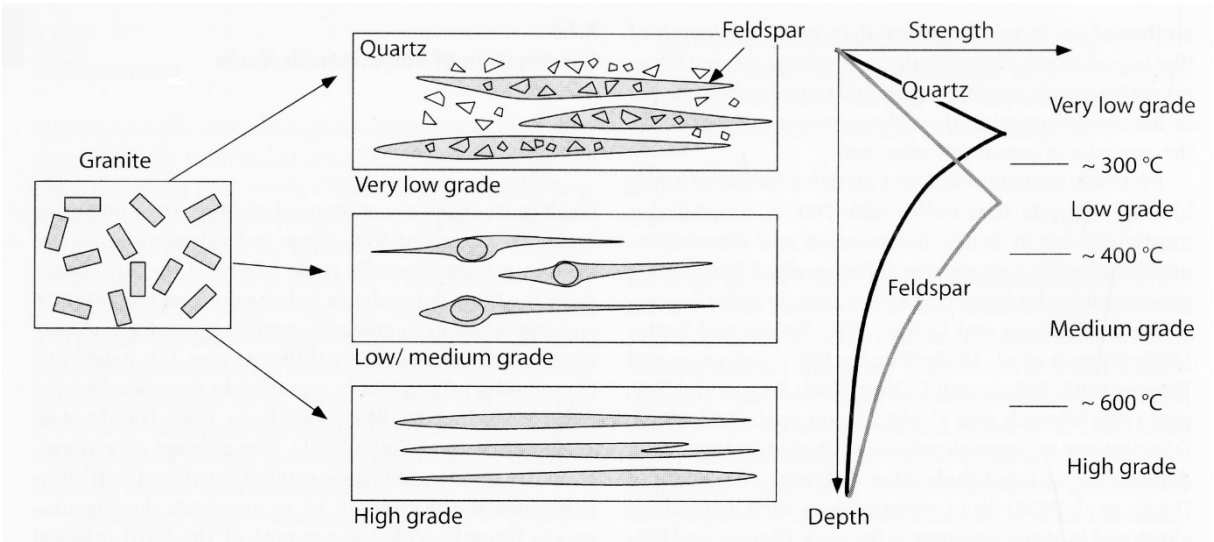

Figure 2-11: To the left; graphical presentation of deformation structures for quartz and k-fsp in a granite, based on depth. To the right; graph illustrates brittle (linear) and ductile (curved) deformation behavior of qtz and k-fsp as a function of strength and depth. At very low grade both minerals deform by brittle fracturing and cataclasis, and feldspar the weaker phase. At low to medium conditions qtz deform by dynamic recrystallization, and fps is the stronger phase developing core-mantle structures. At high grade, both phases deform by dislocation creep and have similar strength. After Passchier et al. (2005)

The studied cataclasites is a mix of protocataclasites, and ultracataclasites in the more deformed areas. No systematic fabrics have been observed e.g., foliated cataclastite. Random distribution of clasts and matrix are common, and it is observed that protocataclasites are intruded by ultracataclasites (figure 2-5 and2-12). Criteria for cross-cutting are used to differentiate between the two events i.e., protocataclastic material are hosted inside ultracataclastic material. Another important criteria is that the ultracataclastic matrix is much more iron rich, as seen from reflected light microscopy (figure 2-12 B). This means that precipitation and healing occurred, since it requires that the first event (completely-) crystallized, and/or that mixing had not a major effect. The presumed low viscosity of the ultracataclasite must have experienced relatively large strain rates, whereas the presumed viscous protocataclasite remained relatively undeformed (Moreira da Silva et al., 1996). In figure 2-12 the microphotograph illustrates that protocataclasites are intruded by the more iron rich ultracataclasites, which results in clasts of ultracataclasites hosted inside protocataclasite. These two different types can be separated as

two temporal cataclastic events, where the latter represents the final stage of brittle deformation, with injection of ultracataclasites into the earlier protocataclasites.

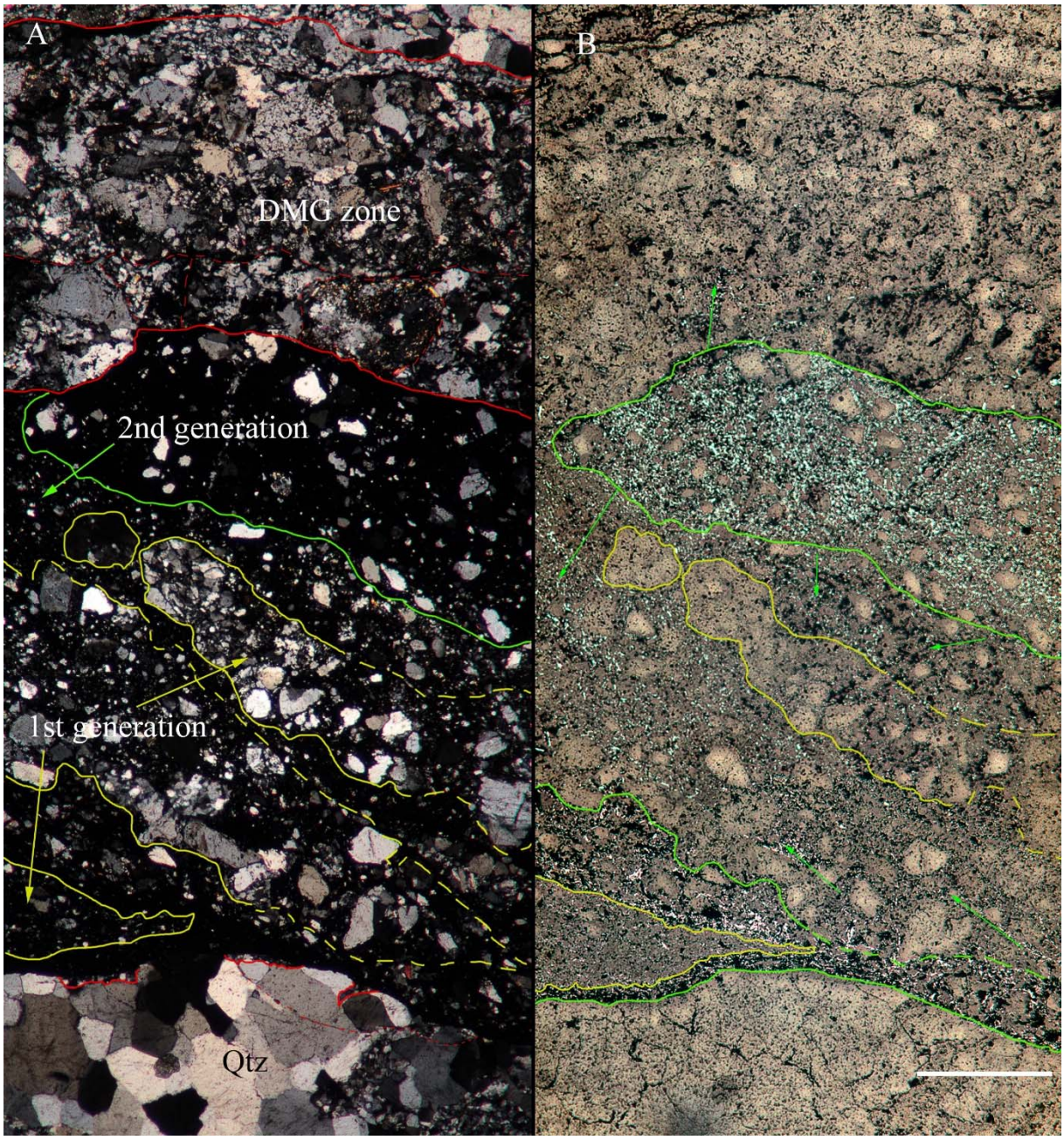

Figure 2-12: Common microstructure of the cataclasites in x-pol (A) and reflected (B) light microscopy. (A) An overview across a cataclastic zone in which two generations of cataclasis is observed. First generation protocataclasis (yellow aggregates. with arrows pointing toward first generation aggregates) is hosted within the second generation of ultracataclasis (green areas, and in between yellow areas, green arrow). The red area illustrates the semiductile damage zone. Stippled lines show cracks within the damage zone. (B) The two generations are distinguished from each other by the presence of iron rich fluid infiltration, recognized by the metallic colored needle shaped heamatite crystals within the green areas. The arrows point toward fluid infiltration into the damage zone along fractures and towards the first generation aggregates. Scale bar=1mm.

2.3.3.1. Mineralogy and textures

In thin sections the ultracataclasites are always followed by an opaque phase within the matrix. The opaque minerals are needle shaped and randomly distributed throughout the matrix (figure 2-15 B3). Some places opaque minerals are infiltrating into fractures in the damage zone and/or diffusing into the semibrittle fabrics of the damage zone. This can be seen from reflected light microscopy where hematite occurs inside the semibrittle deformation fabric (figure 2-12 B). The fabric of the protocataclasite is dominated by a majority of big sub-rounded to angular clasts where some show signs of fracturing into multiple clasts (figure 2-15 A1). These clasts are comprised of quartz (50%), feldspar (20%), epidote (20%) and white mica (10%), with local variations up to c. 90% epidote (figure 2-15 C1), within a matrix composed of c. qtz (60%), and epidote/chl (10-40%) and ±heamatite (30%) with local variations up to 50% heamatite and 30% chlorite where infiltration of ultracataclasites occurs. The size of the clasts varies from c. 5 mm to < 100 µm.

The second generation of cataclasites comprise of rounded to sub-angular clasts with a size of c. 2mm to < 1 µm. With a modal content of qtz (80-90%) and feldspar (10-20%), with some accessory chlorite and epidote, within a matrix of hematite (70-80%), quartz (15-25%) and chlorite/epidote (5-15%) (figure 2-15 B).

Clasts within all generations have a preexisting foliated texture which developed pre-cataclasis, simultaneous with the ductile shearing. This temporal relationship is important when distinguishing between the two phases (i.e., ductile and brittle deformation). Mineralogically the clasts comprise of stretched quartz ribbons, epidote, chlorite, and to some degree feldspars. Some clasts show S-C mylonitic fabric, created during ductile shearing. Another observation is that epidotization occured pre-cataclasis, because some clasts is comprised of ~90% epidote with ~10% quartz/fsp (figure 2-15 C2). This indicates that ductile shearing and significant fluid flow occurred pre-cataclasis, and that cataclasites propagated along the weaker pre-existing ductile fabric.

At the subsiding stages of cataclasis fluid infiltration precipitated chlorite throughout the brittle structures and caused retrograde reactions between idiomorphic epidote and surrounding chlorite, resulting in formation of pumpellyite along strike of the cataclasites (Indrevær et al., 2014b). The observed pumpellyite during this study is forming as reaction rims around epidote grains and in association with fluid infiltration, where it is hosted inside precipitated chlorite

(figure 2-9; 2-13). The occurrence of pumpellyite suggests that temperature dropped to sub-greenschist facies through the late stages of deformation.

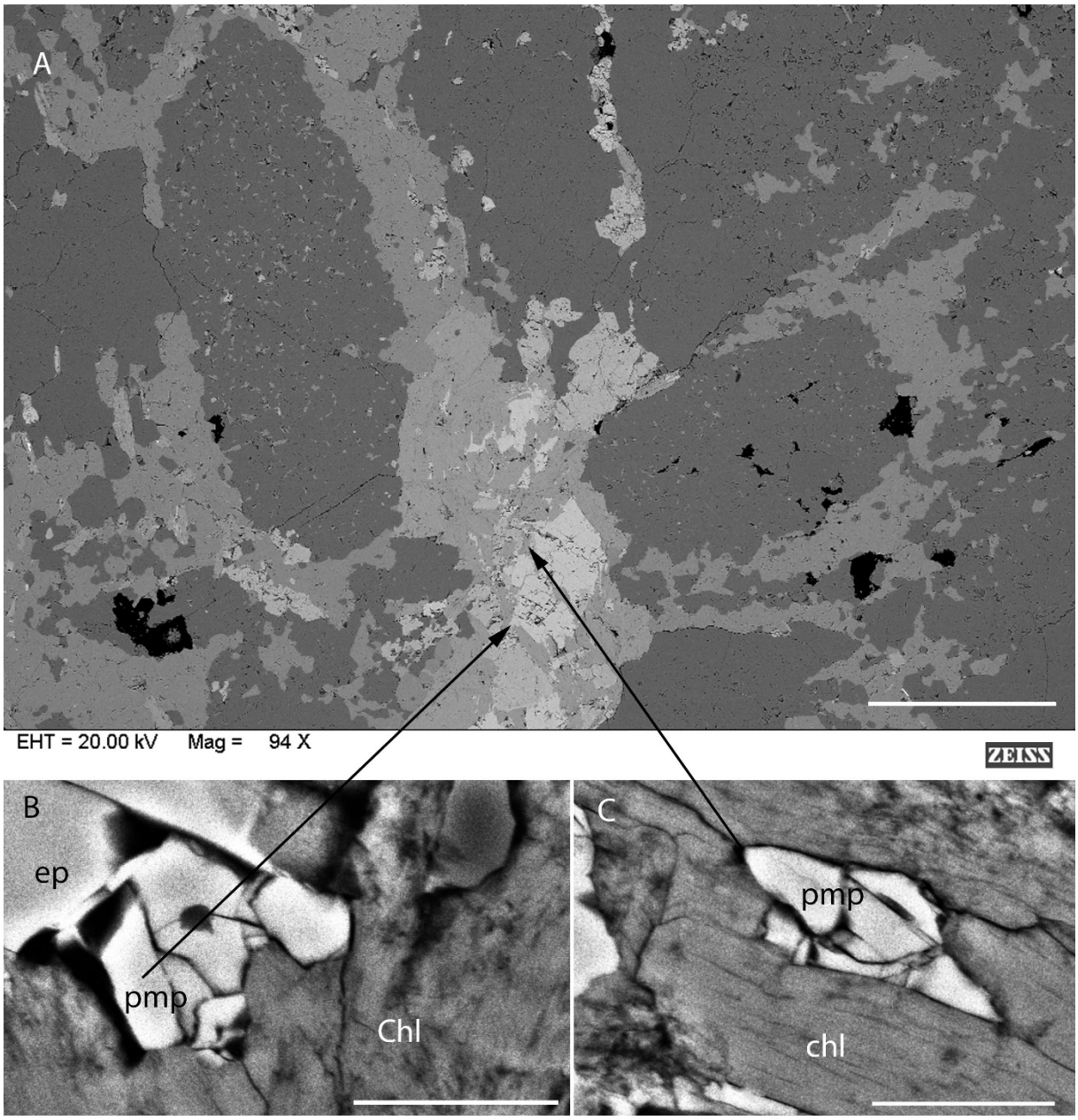

Figure 2-13: By using EBSD analysis pumpellyite was identified in association with fluidized fractures filled with epidote and chlorite. (A) Overview look of a fracture, where the old epidote is fractured, and chlorite and epidote precipitated. Scalebar=500µm. (B) Close up of the area where the arrow points to; pumpellyite forms around epidote grains in contact with chlorite. Scalebar=25µm. (C) A pumpellyite grain hosted within a matrix of chlorite. Scalebar=25µm.

Pumpellyite forms at temperatures ranging from c. 250-300°C (Spear, 1995), thus suggesting that temperatures decreased below c. 300°C during late stages of cataclasis. Further this yields a minimum pressure during late stage faulting of c. 220 MPa, which corresponds to a depth of

c. 8-8,5 km, assuming an average density of granites 2,65-2,75 g/cm^3 in the upper lithosphere, consistent with the minimum pressure stability field of pumpellyite (figure 2-14).

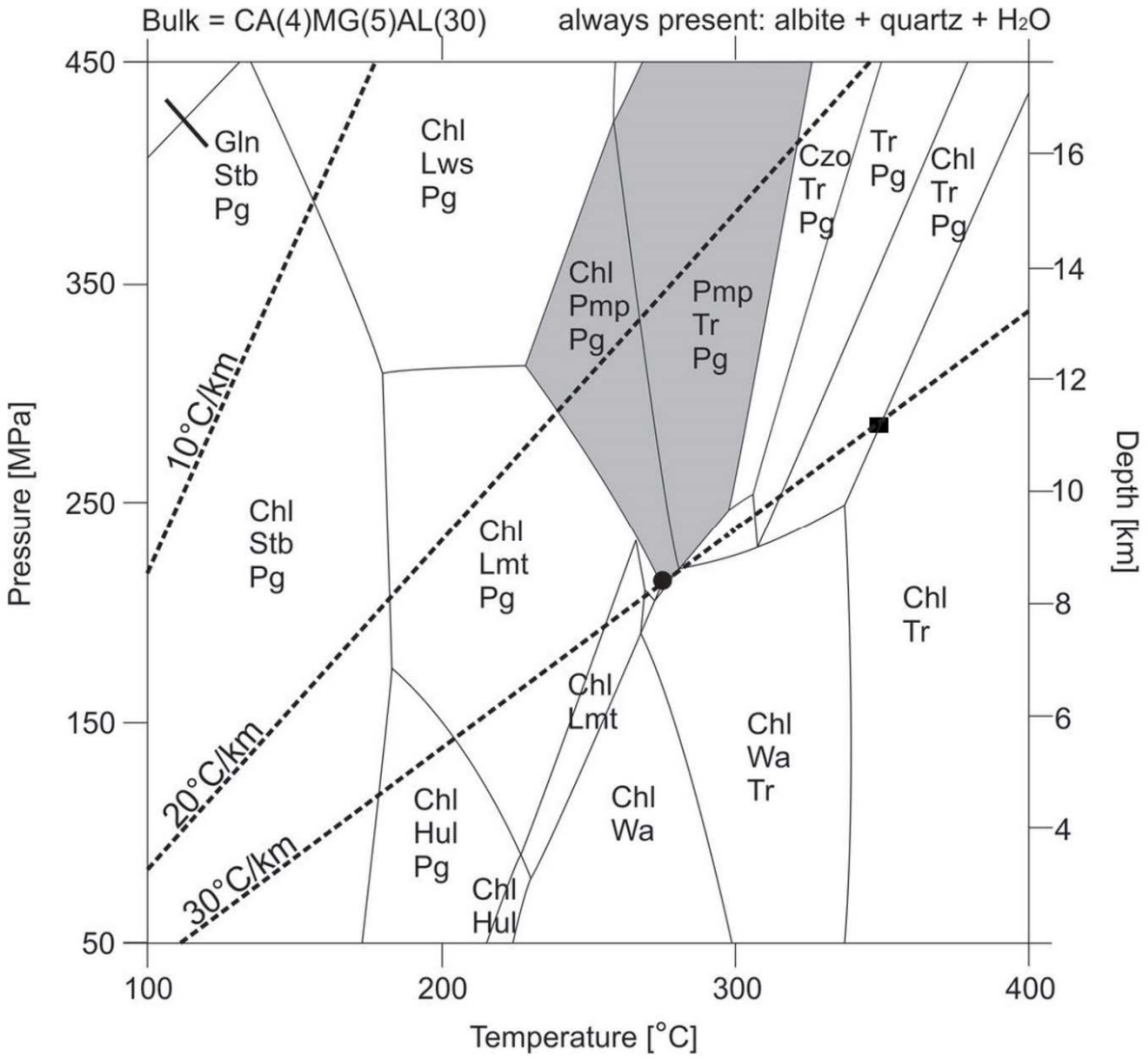

Figure 2-14: P-T diagram showing mineral assemblages and stability field of a CMASH system at low metamorphic grade assuming an average meta-MORB composition. Dashed lines are geothermal gradients and the shaded area marks the stability field of pumpellyite. Black square indicates maximum P-T conditions for early-stage cataclasites and black circle indicate the minimum P-T conditions during late-stage faulting. Abbreviations: Chl=Chlorite, Czo=Clinocoizite, Gln=Glaucophane, Hul=Heulandite, Pg=Paragonite, Pmp=Pumpellyite, Lmt=Laumonite, Lws=Lawsonite, Stb=Stilbite, Tr=Tremolite, Wa=Wairakite (mod. after Indrevær et al. (2014b)).

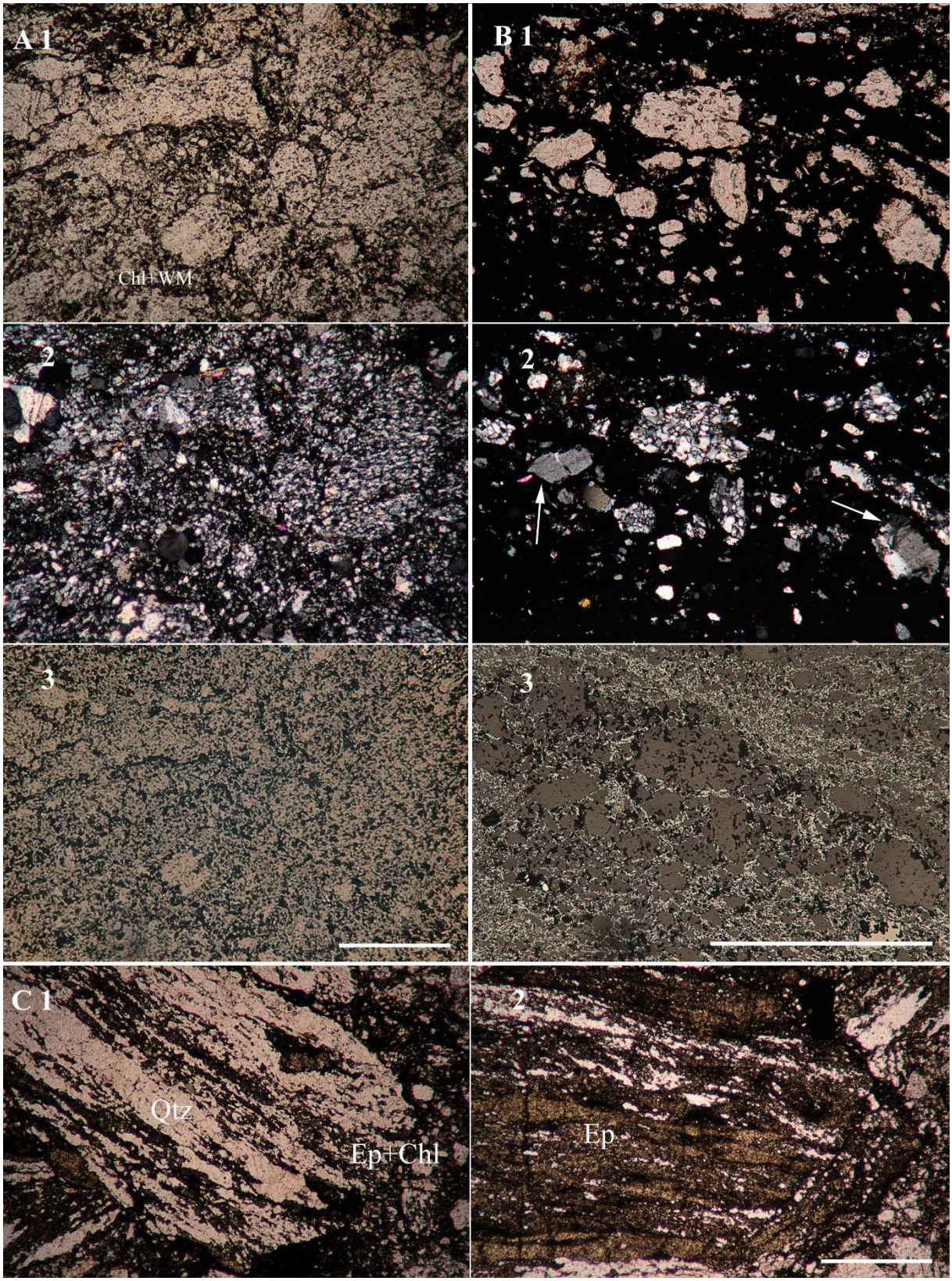
A 1
Chl+WM
B 1
2
2
3
3
C 1
Qtz
Ep+Chl
2
Ep

Figure 2-15 (Prev. page): Microstructural differences between protocataclasis and ultracataclasis. Scale bar=1mm in all examples. (A) Protocataclasis illustrating abundant clasts with chlorite and white mica in the matrix. Clasts comprise of quartz and feldspar, where micas form shear planes within the clasts. 1) Refracted light, 2) crossed polars, 3) reflected light. (B) Ultracataclasis comprising of abundant quartz clasts and some feldspar clasts (picture 2. white arrows) hosted within an iron rich matrix containing of c. 70-80% heamatite. 3) Needle shaped heamatite crystals, possibly specularite, formed hydrothermally. Clasts are generally smaller within the ultracataclasite, comparing (A) and (B). 1) Refracted light, 2) crossed polars, 3) reflected light. (C) 1) Demonstrating a quartz rich clast, with epidote and chlorite, both inside the clast and within the matrix. 2) Epidotized clast containing abundant microfractures.

2.3.4. Deformation mechanisms

In crustal rocks the most important deformation processes are dislocation creep and diffusion creep. An increase of the internal free energy of crystals are due to the generation of dislocations. To compensate for this effect, grain boundary migration recrystallization is active which reduces the internal free energy by increasing the grain boundary area, and thus reducing the grain volume, storing energy at the mineral grain surface. The product of this process is organized dislocations into subgrain boundaries; as the process continues the missorientation across the subgrain boundary will increase until it becomes a new grain with reduced size. This process is known as subgrain rotation recrystallization (regime 2 of Hirth et al. (1992)), and acts to reduce the mean grain size.

As the overall grain size is reduced and the rock is still in the ductile regime a transition to diffusion creep deformation becomes important. This mechanism causes the migration of crystal defects through the lattice of a crystal, part due to vacancies. If a crystal is subject to a greater degree of compression in one direction relative to another, defects migrate to the crystal faces along the direction of compression. The diffusion of vacancies through a crystal lattice may happen in a number of different ways:

1. Nabarro-Herring creep occurs when vacancies move through the crystal (grain)
2. Coble creep is a mechanism in which vacancies move along dry grain boundaries
3. Granular flow happen when the rock deforms to accommodate space problems from simultaneous grain boundary sliding
4. Pressure solution is similar to *Coble creep*, where material moves along grain boundaries in a solution

2.3.4.1. Dynamic recrystallization

Quartz

In the mylonite quartz aggregates are fully recrystallized and appear as elongated objects with grain size corresponding to the shear zone fabric, and are aligned to the foliation (figure 3-3 A). The earliest quartz grains show patchy and sweeping undulose extinction, suggesting deformation of the crystal lattice. The complete lack of chessboard patterns indicates that temperatures during deformation were below the α-β transition at c. 573°C. In this temperature regime quartz behaves ductile and dislocation glide (300-400°C) is dominant along basal glide planes in the (C)<a> direction, but no bulging recrystallization is observed. This may be caused by fluid circulation, or brittle deformation. Dislocation creep (>300°C) aid the deformation, but were probably the dominant deformation mechanism during higher temperature regimes with prism m<a> and m<c> slip. The prism glide planes are generally thought to be operative at higher temperatures (>amphibolite facies), but may be active in greenschist facies condition where fluids infiltrate. Fluids are known to reduce the critical resolved shear stress for prism glide (Hippertt, 1998). In the high strain areas subgrain rotation recrystallization is dominant, and quartz aggregates show signs of grain-mobility with lobate grain geometry, which can lead to highly mobile grain boundaries (Passchier et al., 2005). This suggests that grain boundary migration swept through entire crystals to remove dislocations, and possibly subgrain boundaries as well (Hirth et al., 1992).

Subgrains develop from the margin of quartz aggregates and progress to the core, forming aggregates of fully recrystallized quartz. Size of new grains are usually the same as the old grains, indicating subgrain rotation recrystallization. These aggregates produce notable grain shape fabric (SPO) consistent with the overall shear sense. With progressive deformation towards the center of the shear zones, the quartz aggregates are progressively stretched to form layers of polygonal quartz, with decreasing grain size. During dislocation creep of quartz aggregates, fluids seems to seep into the aggregates along grain boundaries enhancing recrystallization and resulting in precipitation of chlorite, epidote and white mica. Fluid infiltration seems to be present during dislocation creep of the quartz aggregates causing separate quartz bands foliation parallel.

Figure 2-16 A-D illustrates what occurs with increasing strain, as the aggregates undergo dislocation creep they are elongated and thinned. When this process becomes difficult (e.g., at low temperature and/or abundant matrix), a switch in deformation mechanism to diffusion creep

occurs, causing static recrystallizing in the quartz aggregates during progressive deformation of the matrix, resulting in straight grain boundaries. The recrystallized quartz aggregates forms monomineralic layers in the ultramylonite with a width of one grain. Recrystallization progressively reduced grain size towards the ultramylonitic phase mixture of c. 20 µm. Some of the monomineralic quartz bands show deformation marked by intrafolial folding (figure 2-16 C). Hippertt et al. (1998) reported that quartz grains deformed in this manner always had the basal planes parallel to the folded surface, indicating that basal <a> slip operated during fold development. The presence of these intrafolial folds may reflect the rehologically different bands in the mylonites (e.g., qtz, feldspar and mixed phases), and suggests that ductile stretching of the qtz bands was not sufficient to accommodate progressive strain, leading to the observed microfolds. Locally qtz aggregates are completely disintegrated and mixed with the matrix, deforming by diffusion creep processes such as granular flow and precipitation processes (figure 2-16 D).

As temperatures likely decreased to around 300-400°C, a constant production- and grain size reduction in the matrix, is likely to have caused a switch in deformation mechanism from dislocation creep to diffusion creep. This switch of rheology, causes quartz to become the strongest phase (figure 3-3 and section 2.4.2), and diffusion creep to be the dominant deformation mechanism, through granular flow and pressure solution precipitation processes.

Figure 2-16 (Next page): Microphotographs of different deformation mechanisms and microstructures. Scale bar on picture A-G=1mm, picture H=100 µm (A) Recrystallized qtz aggregates through subgrain rotation, resulting in new grains. Straight grain boundaries suggests static recrystallizing. Micaceous bands penetrate the aggregate, creating weak areas. (B) With progressive deformation the quartz aggregates split up into foliation parallel bands. (C) Monomineralic quartz layer creating a z-fold with strain shadows behind the fold hinges (stippled areas). Dextral sense of shear. (D) Shape preferred orientation (SPO) of disintegrated quartz layers, mixing with the matrix. Qtz long axis show apparent anticlowise rotation, with respect to shear plane (horizontal). Dextral sense of shear. (E) Overview of deformation structures within k-fsp, where dynamic recrystallization to albite occurs along perthite, which is later crosscut by hydrothermal fractures (associated with early stages of cataclasites) and an extensional fracture filled with quartz and precipitated radial chlorite and heamatite (associated with late stage cataclasis). (F) Stippled line outlining the extensional fracture from picture (E). (G) Cataclastic fracture (associated with late stage cataclasis) filled with chl+qtz+hem cutting the early stage hydrothermal fractures. (H) Bulging recrystallizing of K-fsp, later cut by annealed hydrofracture.

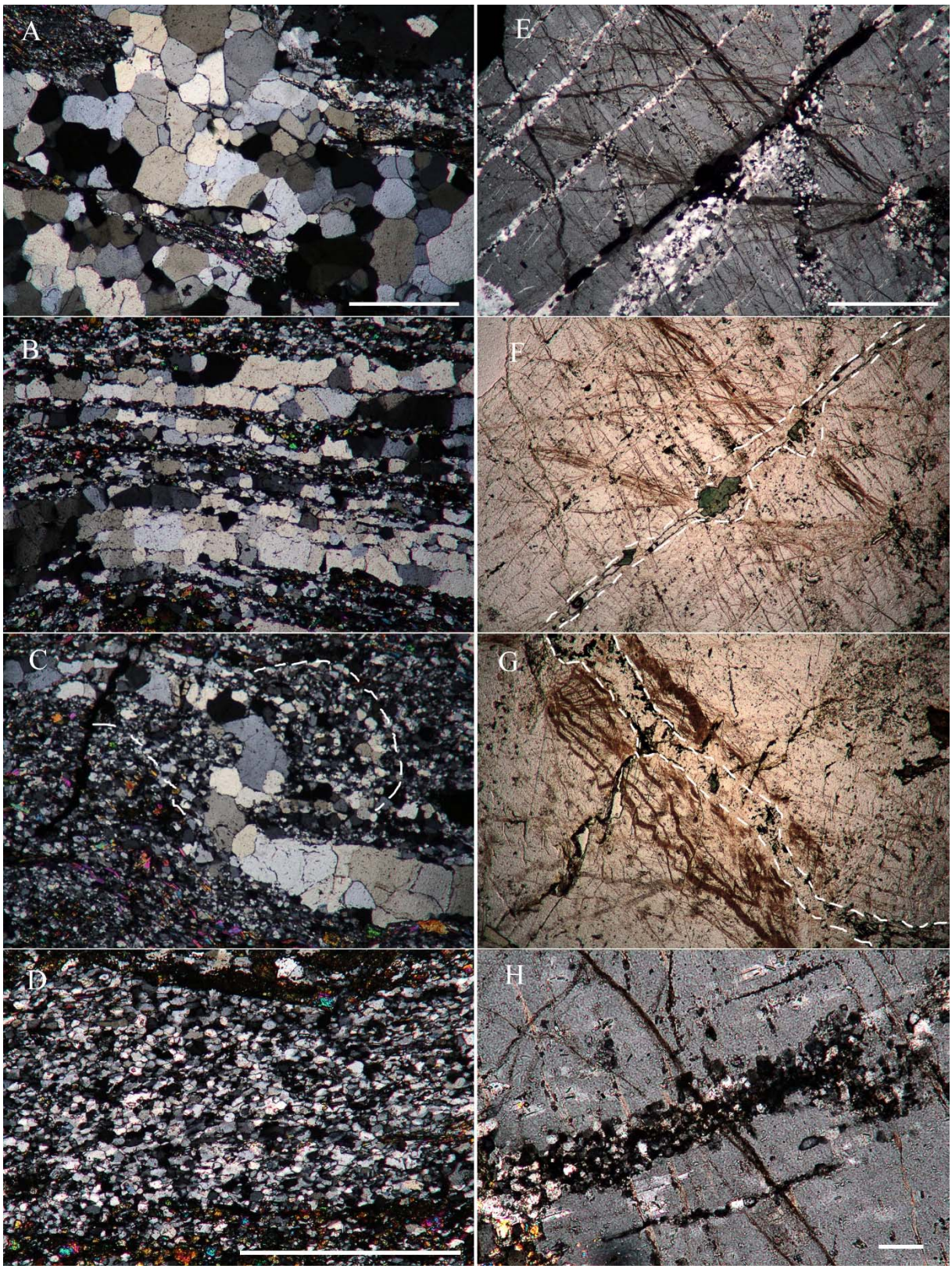
A
E
B
F
C
G
D
H

Feldspar and mica

Deformation behavior in plagioclase and K-feldspar is rather similar and therefore the feldspars are treated together (Passchier et al., 2005). Although dynamic recrystallization is observed to occur at temperatures as low as the upper greenschist facies (c. 450°C), fracturing of feldspars continues to be important for deformation even into the granulite facies (Fitz Gerald et al., 1993). These observations are in agreement with easy fracturing along the excellent cleavage directions in feldspar.

The fractures in feldspars are examples of brittle behavior where deformation has been discontinuous. Once fractures have developed sufficient for chemical reactions to be initiated, it is likely that deformation became continuous and was not cataclastic in any sense. Fracturing may have initiated deformation of the big phenocrysts by allowing intragranular chemical reactions to initiate, creating new grains. The early fractures do not continue into the matrix; instead the deforming phorphyroclasts may simultaneously show brittle and ductile characteristics in different regions.

The most prominent deformation feature of plagioclase, due to intragranular chemical disequilibrium are the small inclusions of white mica and epidote associated with neocrystallization. Plagioclase also contains bent twins, undulatory extinction and microfractures (2.3.1). An important feature during recrystallization of feldspar is the compositional change at clast margins and near fractures. Newly formed grains are significantly more albitic than the parent grain. Recrystallization of K-fsp also produce albitic plagioclase, similar to reports by Fitz Gerald et al. (1993).

Prominent perthite and flame perthite in K-fsp indicates that the phenocrysts were a principal source of K^+ ions to form mica during deformation. The role of micas is very important in both the initial and advanced stages of progressive deformation. Biotite seems to have retrograded to chlorite, white micas and may have been a minor constituent to the formation of epidote. Excess ions may have been transported away with a fluid phase. Common deformation mechanisms for micas are pressure solution, fracturing, kinking and folding. Chlorite are observed along incipient foliation planes defined by mica, suggesting that these foliation surfaces were a locus for fluid activity. This fluid activity probably favored the softening reactions (section 2.3.4) that produced very fine grained white mica from the original plagioclase grains. The mica-producing softening reactions in plagioclase are more intense along grain boundaries and intragranular microfractures that are in contact with mica-rich

domains, confirming that fluid circulation was present along the micaceous bands. Along these bands micas are orientated with their basal planes parallel with foliation and therefore in a position of easy slip. This sequential process appear to constitute a feed-back mechanism that progressively increase strain accommodation in the micaceous bands, resulting in plagioclase breakdown and interconnections between adjacent mica bands.

Matrix phases

Fine grained albite is a product of dynamic and chemical recrystallization of feldspar along grain boundaries and microfractures. The plagioclase remains at a constant size throughout the mylonite and ultramylonite, but their shape change towards more elongated grains. A few porphyroclasts are scattered throughout the matrix, surrounded by smaller grains of recrystallized material creating core-mantle structures (figure 2-10 C; figure 3-5 A). The homogeneous distribution of grain size for the feldspars within the matrix, suggests a process of replacement or dissolution and precipitation during deformation. This microstructure indicates diffusion creep. K-fsp grain within the matrix usually forms recrystallized layers intermixed with the other matrix phases. The plagioclase in these layers may partly be from myrmektic origin or perthitic. Diffusion creep processes is the dominant deformation mechanism in the monomineralic fine grained K-fsp aggregates. Grain size and grain shapes are very similar to that of plagioclase.

The grain size of recrystallized white micas remain relative constant in the mylonite and ultramylonite. Dislocation creep microstructures in the micas are not homogeneously distributed throughout the strain localization. In the mylonite micas form interconnected layers and show bending, kinking and fish microstructures common for crystal plastic deformation. In the ultramylonite the mica are randomly scattered which suggests that, with increasing strain, portions of mica underwent dissolution-precipitation processes. Similar distribution of mica have been reported by rocks undergoing diffusion creep (Kilian et al., 2011), thus the observed mica structures suggests that there is a change in dominant deformation mechanism from dislocation creep to diffusion creep deformation in the ultramylonite.

2.3.4.2. Cataclastic flow

On a mesoscale (2.2.2) it is evident that cataclastic deformation happened. This is seen from the field observations of brittle fractures filled with rock fragments and precipitation of hematite along the fault planes (2.3.3). Fractures of different length and width occurs, causing grain size reduction by fragmentation. The pre-existing fabric is more or less obliterated where the intensity of fractures is high.

On a microscale the clasts show abundant microfractures which reflects the predominant deformation mechanism. As progressive cataclasis happen, a distribution of clasts sizes is developed that allows sliding of clasts past each other, resulting in comminution (see 1.4.2). When this happens deformation is accommodated by continued sliding and rolling of fragments, known as cataclastic flow. On the microscopic scale cataclastic and crystal plastic deformation features coexist. However, in the absence of recovery processes and widespread recrystallization near the frictional – viscous transition, effective pressure (hence friction) is expected to control the strength of the cataclasites (Hirth et al., 1994).

Comparing the mesoscopic structures with the microstructures, the boundary between cataclastic fault rocks and the ductile shear zones is quite abrupt, where brittle structures are well visible, but in the optical microscope this transition is followed by a thin zone of semibrittle flow (i.e., a damage zone). In the damage zones the rock behave very cohesive, and fractures propagate near orthogonal outwards (i.e., into the host rock) causing more deformation. Dynamic recrystallization and precipitation is abundant, cementing together the partly fragmented zone. Because friction controls the deformation, the zones do not widen too much, which is a direct result of easier frictional gliding than progressive cracking. Referring to the Mohr-Coulomb envelope (figure 3-7), differential stresses may be too low to reach a critical shear stress to make new cracks, as well as the abundance of water, the frictional forces are reduced, and gliding is easier.

2.4. Chapter 2.3: Micro-kinematic data and results

This chapter contains a description of deformation related microstructures and shear sense indicators. The identification and interpretation of micro-kinematic data is used as a part of the shear sense and deformation mechanism determination.

2.4.1. Sense of shear

Many reliable shear sense indicators can occur in thin sections, helping to establish movement directions. Through optical microscopy of thin sections, microstructures that give reliable shear senses have been found (Hanmer et al., 1991). A short description of the different shear sense indicators follows.

S-C fabrics

As described by Lister et al. (1984), Shimamoto (1989) and , it occurs both in the shear zones and the foliation bands within the studied Ersfjord granite. In both the studied locations S-C fabrics are found in areas of qtz and chorite, were the S-direction is marked by thin chlorite bands following the maximum elongation of the qtz aggregates, while the C-direction (i.e. slip plane) is defined by the long axis of white mica (figure 2-17 A).

Mica fish

These are produced by either bending of mica grain edges, so that they are given the shape of σ-clasts (Lister et al., 1984) or pressure solution with lateral growth by precipitation of dissolved material (Passchier et al., 2005). An example of a chlorite-fish is seen in figure 2-17. Interpeded as lateral growth along the shear plane, giving it the “fish” structure.

σ-clasts

These unrotated clasts of material develops tails by either pressure solution followed by precipitation, or dynamic recrystallization of clast material (Passchier et al., 2005; Simpson et al., 1993). Occurrence of such shapes are found in (1) plagioclase, (2) K-fsp and (3) quartz aggregates undergone recrystallization (figure 2-10 A, C; 3-2 A, B; 3-5 A).

Rotated porphyroclast

These are pre-deformational clasts (i.e. remanants from the protolith fabric) that rotate and deform during progressive deformation and usually creates stress drops behind the clasts (i.e.

strain shadows) due to inhomogeneous deformation, in respect to the sense of shear, resulting in solution precipitation (Passchier et al., 2005). These clasts are found in the mylonites, were the matrix is anastomosing around the clasts. Figure 2-17 B show titanite clasts rotating with the sense of shear creating domains of strain shadows were solution precipitation occurs.

Quartz shape fabric

Quartz SPO are commonly used as shear sense indicator (Kilian et al., 2011; Lister et al., 1984), with inclined grain long axis in relation to foliation. An apparent anticlockwise rotation of the grain long axis (De Ronde et al., 2004), with respect to the shear plane, is indicative of a dextral shear sense (figure 2-16 D). This fabric has been found in the ultramylonite, where monomineralic qtz bands have disintegrated.

Displacement markers

Passive shear sense indicators, such as the displacement of grain boundaries and splitting of grains on opposite sides of the cataclastic zone (figure 2-18), were used to determine the sense of shear in the cataclasites. The displacement of the grain boundaries and the characteristic splitting of the grains indicates a dextral sense of shear, consistent with the mesoscopic observations (2.2.2)

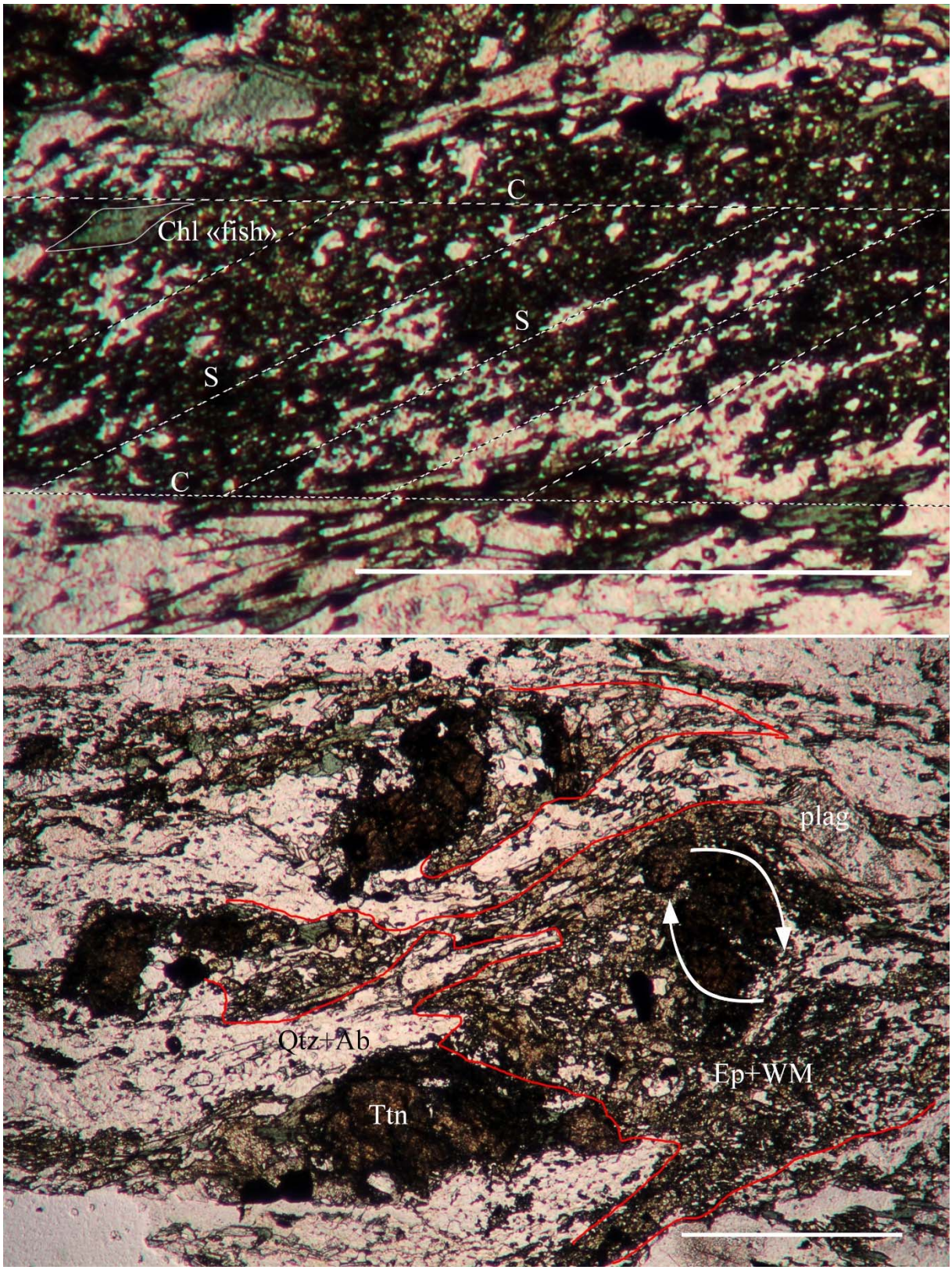

Figure 2-17: Indicators of dextral shear sense. Scale bars=1mm. (A) Microphotograph of S-C fabric in a mylonite, where S-direction is marked by precipitation of chlorite along maximum elongation of qtz aggregates. A mica "fish" developed by pressure solution with lateral precipitation along C-direction. (B) Rotated titanite porphyroclasts, developing strain shadows, with respect to the sense of shear.

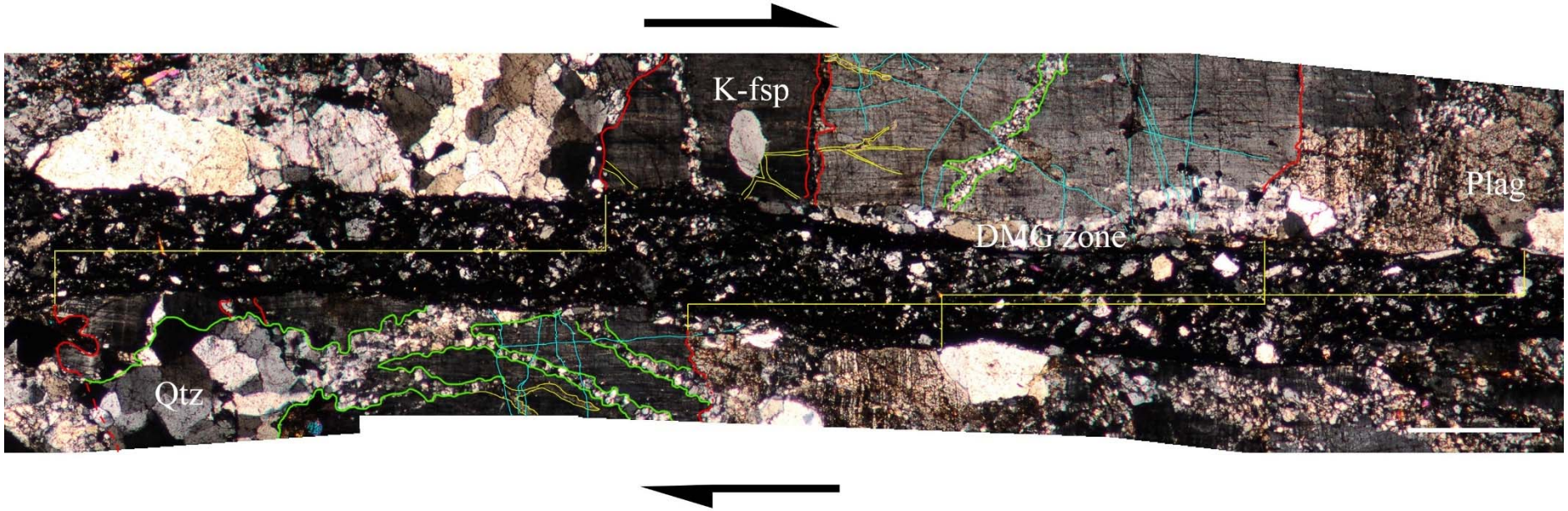

Figure 2-18: Combined microphotographs show dextral displacement for a cataclastic zone in the Ersfjord granite, based on microstructural displacement markers. Yellow bars illustrate the minimum dextral displacement from passive markers on opposite sides of the cataclastic zone. Green- and yellow areas show incipient recrystallization and healing along early fractures, where static recrystallization in quartz rich areas has occurred. Red areas marks grain boundaries. Blue areas outline late brittle fractures which occurred after the main cataclasis. This is evident because the fractures cut the damage zone. Plagioclase exhibit abundant fractures, in which white mica grow due to chemical disequilibrium, and bent twins. Scale bar=1mm.

2.4.2. Strain and deformation mechanisms

Within this chapter results from the strain analysis will be presented. First, shear strain estimations from the ductile shear zones will be presented, then flow stresses and strain rates estimated, will be presented, followed by calculations of fabric trajectories estimating the displacement within the foliation. And last, shear strain and slip-rate for the cataclasites will be presented.

2.4.2.1. Shear strain within the ductile shear zones

During dynamic recrystallization or chemical reactions, strain markers are absent and strain analysis in the strict sense is not possible (De Ronde et al., 2004). However, it is observed that the shear zones of the Ersfjord granite develops shape fabrics that track deformation in a similar way as strain markers would (figure 2-19): aspect ratio R* and rotation of rigid aggregates increase (i.e., α* decreases) for increasing amount of deformation. Therefore, fabric variations of recrystallized quartz aggregates are used as an indicator of the finite shear strain; this can be done because quartz is present throughout the entire shear zone interval (diagram 2-1).

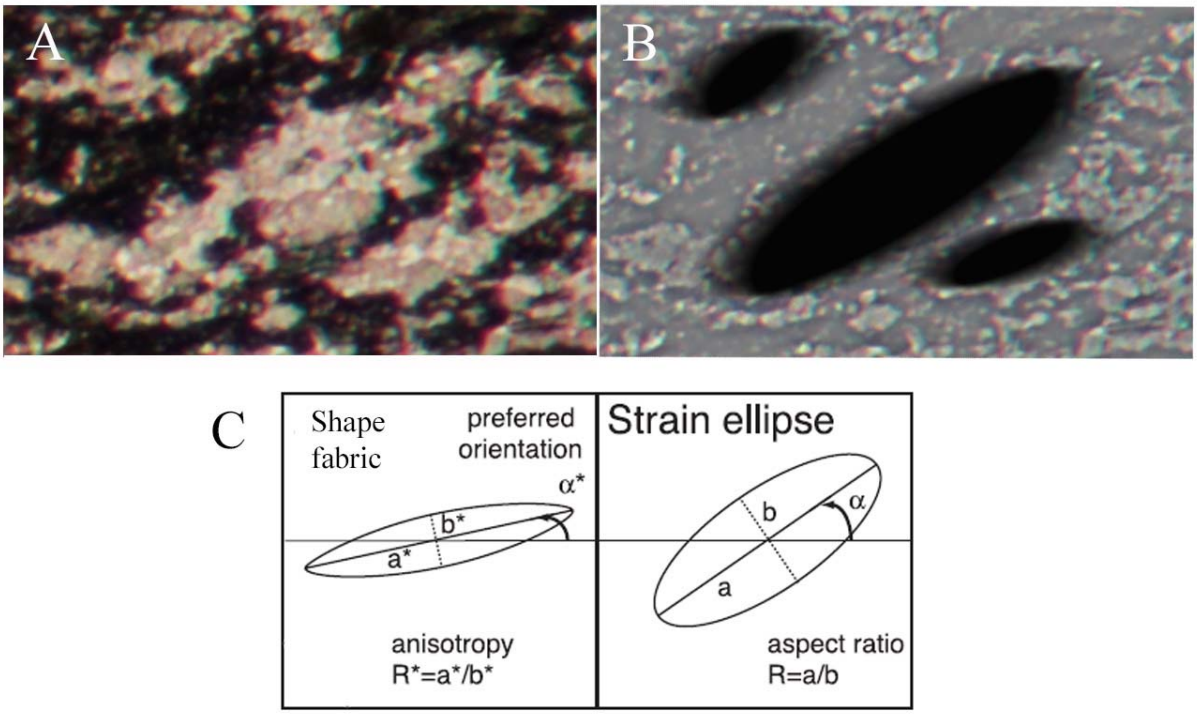

Figure 2-19: Strain analysis of shaped fabrics. (A) Micrograph of homogeneous dynamic recrystallized qtz aggregate. Dark areas are reaction products. Dextral shear sense. (B) Masked out aggregate areas, overlaid with the sape and orientation of the strain ellipse (black areas). (C, left) Fabric parameters: Anisotopy R and shape-preferred orientation α* (angle of the long axis with chosen reference line, in this case horizontal). (C, right) Equivalent parameters of the strain ellipse for simple shear: Aspect ratio R and angle α between the long axis of the strain ellipse and the shear direction. Base of image (A, B) 500 µm.*

Forty seven recrystallized quartz aggregates were measured and used to estimate the finite shear strain (see methods 1.3.3.1). If the average rotation and elongation of the recrystallized qtz aggregates are considered, with respect to the reference line, as the orientation of the finite strain ellipse (figure 2-19 C), local shear strain distribution from fabric anisotropy can be estimated across the shear zone. De Ronde et al. (2004) used the R* and α* to qualitatively calculate shear strain. Measurements of R* is a more robust criteria to use in the calculations, because accurate measurements of small angles are difficult. Therefore, only fabric anisotropy R* of quartz aggregates are used for the calculations. In natural deformed rocks it is impossible to consider thinning (i.e., area loss in 2-D at the ends of a sample), so a treatment of only simple shear deformation is calculated using equation [7] of Ramsay et al. (1983) p.295,296 described in section 1.3.3.

Results for the fabric anisotropy are presented intable 2-2, where R* values corresponding to the highest density of points, fromdiagram 2-1, are chosen for the shear strain calculations. These finite shear strain values should correspond with a high concentration around an angle α, which explains the rotation of the rigid clasts for the corresponding shear strain. The calculations are done accordingly to equation [5] in section 1.3.3.

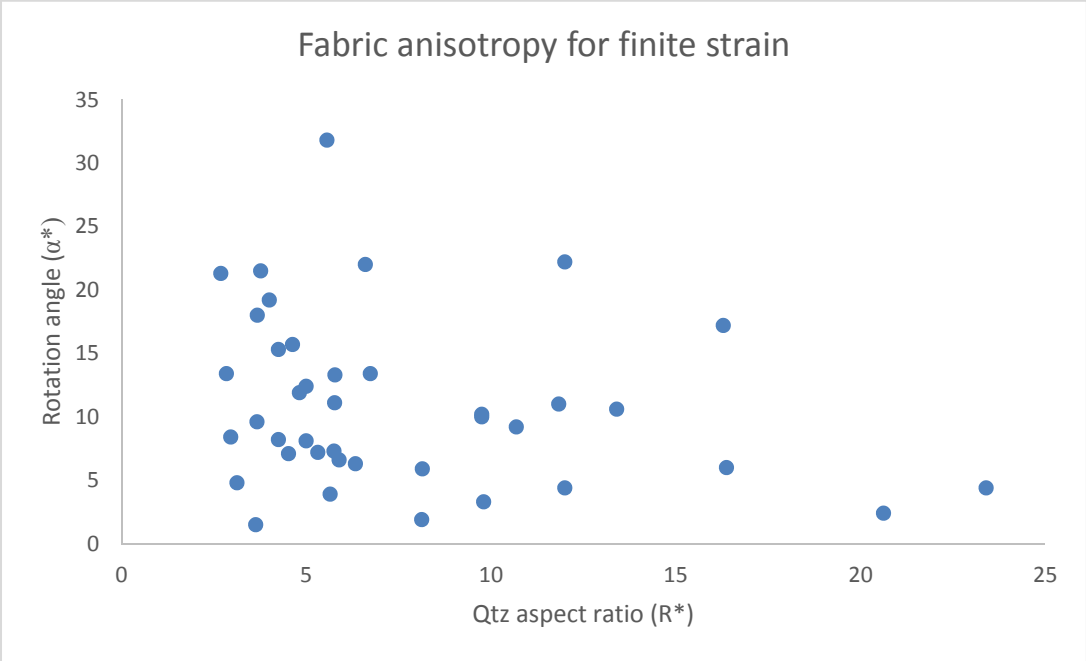

Diagram 2-1: The diagram show aspect ratio (R) variations of rigid qtz aggregates across a shear zone, in respect to a reference line (parallel to shear plane). As the rotation angle (α*) decrease the aspect ratio increase, which translates into higher shear strain (n=47).*

Table 2-2: Calculated (eq. [5] and [7]) shear strain γ for a given fabric anisotropy R*, and expected rotation angle α for given γ**

R*	**γ* [7]**	**α [5]**
5	1,79	24,1
12	3,18	16,1
22	4,48	12,0

From table 2-2 and diagram 2-1 it is apparent that the expected rotation angle (α) does not correspond to the measured rotation angles α*, for the corresponding aspect ratio R*. This difference may be caused by viscosity contrasts within the shear zone, where rigid particles rotate faster and are exerted to less deformation. Or the rigid aggregates (figure 2-10 F) break up along weak zones that already lie on an acute angle with the shear zone, resulting in recrystallization nearly parallel with the shear bands (figure 2-20) (discussion in section 3.3.1).

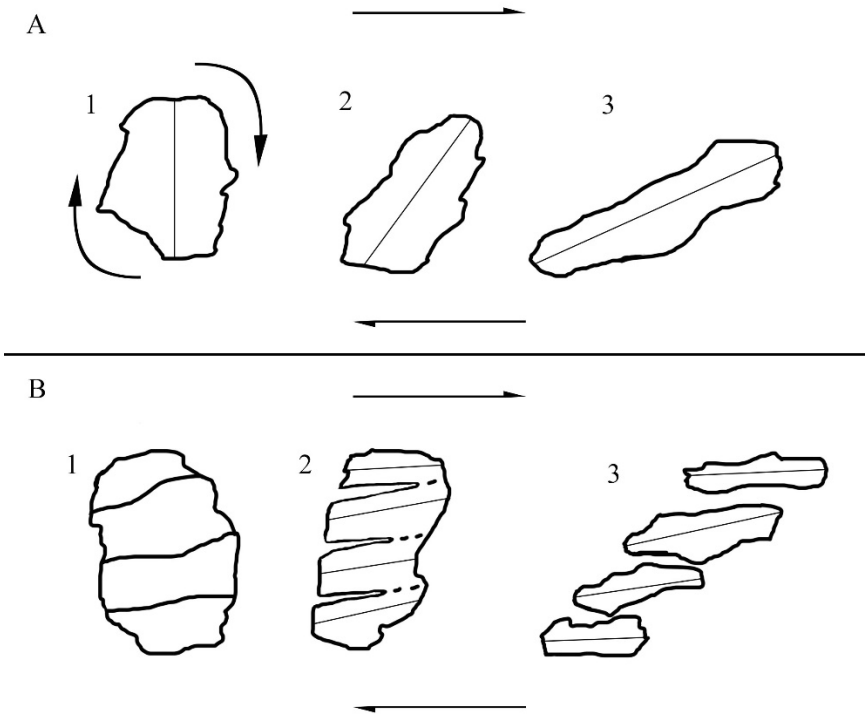

Figure 2-20: Modell illustrating three different mechanisms which can produce the wide spread of rotation angles of quartz aggregates to a certain shear strain. (A) Stepwise rotation of a quartz aggregate (Stage 1: ± 1:1 aspect ratio). During progressive rotation and recrystallization the aspect ratio increase with increasing shear strain (stage 2-3), thus decreasing α. Or the rigid aggregates rotate quickly within a less viscous matrix causing a wide spread in the rotation angles α* (only step 1) and producing smaller aspect ratios (step 2). (B) In stage 1 the quartz aggregate contains foliation parallel chlorite bands, which acts as weak zones with increasing shear strain (stage 2), and thus the aggregate begin to break up parallel to these chlorite bands producing separate qtz aggregates with an already acute rotation angle α* (step 3).*

2.4.2.2. Flow stress and strain rate estimation for the ductile shear zones

Flow stresses and strain rates have been estimated using the equations presented in section 1.3.3. The flow stresses has been calculated for each of the grain size populations, resulting in a minimum and maximum estimate. The strain rates have been estimated using the minimum and maximum results from the calculated flow stresses for each population of margin and interior grain sizes.

Table 2-3: Grain size measurements of qtz aggregates within the ductile shear zone. The four populations represents different recrystallization regimes, where the largest grains represent recrystallization along margins, and the smallest grains represent recrystallization in the interior.

Margin n=169 Interior n=101	**Margin**		**Interior**	
	long	short	long	short
Grain size [µm]	301	254	115	78

The measured grain sizes along the margins are bigger than for the expected deformation mechanism for subgrain rotation recrystallization after regime 2 of Hirth et al. (1992). The margin grain sizes were expected to lie within the transition for grain boundary migration and subgrain rotation recrystallization, at 100-150 µm (Stipp et al., 2002b; Stipp et al., 2010), but show a size fraction 2-3x larger than expected (figure 2-21).

The grain sizes of the interior lies within the subgrain rotation recrystallization area. With a grain size of c. 70-100 µm it plots in the middle of the expected grain size frequency for subgrain rotation (Stipp et al., 2010), and within the expected temperature range of around c. 350-400°C (figure 2-21).

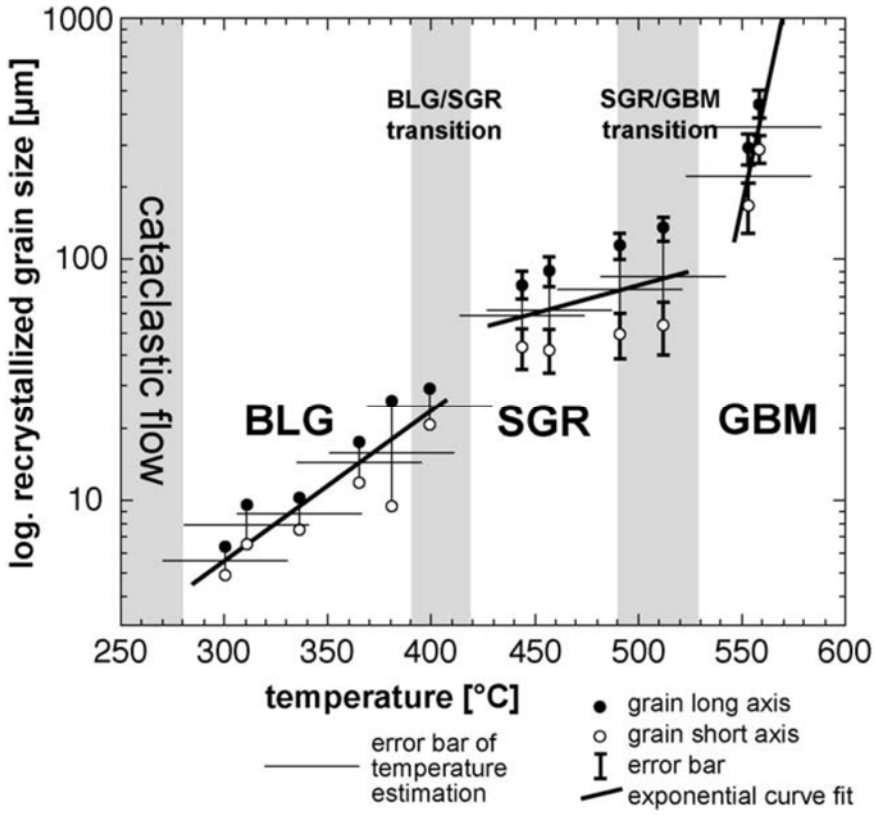

Figure 2-21: Diagram of recrystallized grain size versus temperature and expected recrystallization method (after Stipp et al. (2002b).

Flow stresses and strain rates were estimated based on the measured grain sizes (table 2-3), following the methods highlighted in section 1.3.3, and presented in table 2-4.

Table 2-4: Flow stresses and strain rates calculated for the populations of margin and interior grains. The strain rate is calculated using the minimum and maximum values from the flow stresses. Equations and constants are presented in section 1.3.3.

	Equation	Margin	Interior
Flow stress avg.	1	7,73	18,28
Flow stress median	1	**7,69**	**17,80**
Flow stress avg.	2	11,75	33,75
Flow stress median	2	11,69	32,85
Flow stress max	2	12,55	**38,95**
Flow stress avg.	Twiss (1977)	**14**	30,5
Strain rate min	3 (a)	$4{,}05*10^{-18}$	$1{,}16*10^{-16}$
Strain rate max	3 (a)	$4{,}50*10^{-17}$	$\mathbf{2{,}67*10^{-15}}$

The flow stresses calculated varies some with the use of the different paleopiezometers, but it is still evident that the interiors of the shear zones were subjected to higher flow stresses (average: 33,75 MPa) than the marginal areas (average: 11,75 MPa). This is a direct result of the finer grain size measured in the interior of the shear zone. The low flow stresses may be caused by an overestimation of the grain sizes from the paleopiezometers at such large grain fractions, especially for the margins. Flow stresses in the range of c. 10 MPa may indicate post deformational grain growth (Hirth et al., 2001), as observed in quartz grains from these shear zones (figure 3-5 B), which displays triple junctions and straight grain boundaries.

Strain rate estimations varies with the use of different constants and are generally slower than the expected values of these temperature regimes (Stipp et al., 2002a). The implications of this is that strain partitioning into the matrix happens, and that the rigid quartz aggregates statically recrystallize (i.e., are rheological passive). The basis for this implication are all the triple junctions and straight grain boundaries observed within the quartz aggregates. Another explanation for the slow strain rate could be the large grain fractions by them self, but this do not reflect the triple junctions and straight grain boundaries observed. Figure 2-22 A illustrates a temporal model of a shear zone in the Erfjord granite where the interior is subjected to higher shear strain rate than the margins, this implies that the margins are expected to be statically recrystallizing much earlier than the interior, thus resulting in bigger grain sizes. Figure 2-20 B illustrates why strain rates measured are so slow. During progressive deformation strain softening occurs, creating a bigger viscosity contrast of the rigid quartz aggregates relative to the weak matrix minerals (e.g., ep, chl, wm), resulting in grain growth of the qtz aggregates during progressive deformation, in the form of static recrystallization. This is possible if dislocation creep is difficult in the aggragates, and deformation is accommodated by diffusion creep within the matrix.

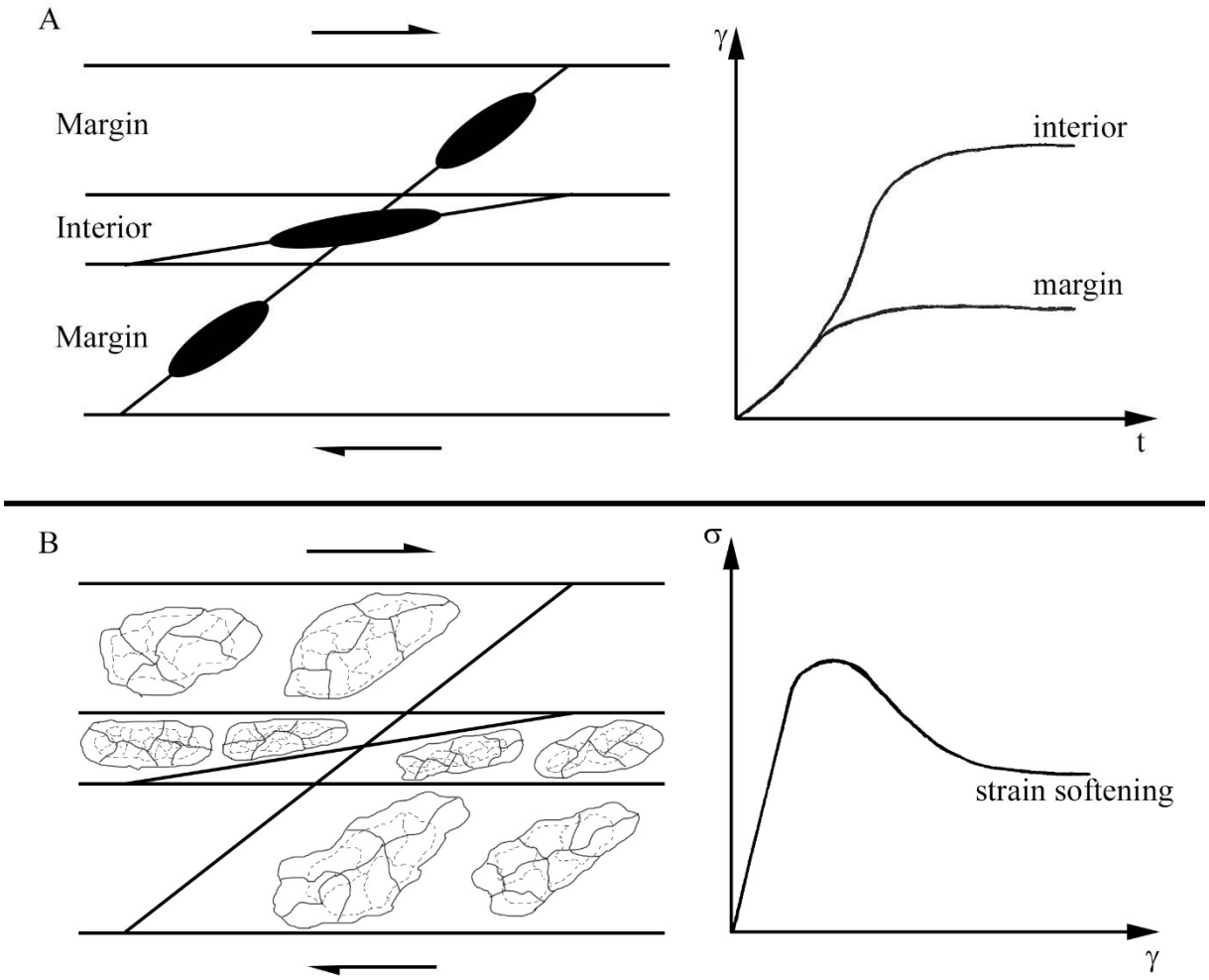

Figure 2-22: The models show a section of the dextral shear zones in the Ersfjord granite. (A) Black ellipses are illustrating the difference of the finite strain ellipse, from the margin to the interior of a shear zone. The graph is illustrating temporal shear strain [γ] concentration into the interior of the shear zones compared to the margins. (B) Static grain growth of quartz aggregates throughout the shear zone, reflecting the different deformation mechanism in the aggregates compared to the matrix, resulting in different mechanical work rate [$\dot{W}$]. Stippled lines represents the original grain sizes, whereas solid lines represent the annealed sizes. The graph illustrates material softening, resulting in locally elevated strain under constant stresses.

2.4.2.3. Fabric trajectories within the ductile foliation

For three cross section within the foliation of the Ersfjord granite it was constructed fabric trajectories and isogons for estimating the apparent displacement of a shear band, and try to determine the total displacement of the foliated area. For the methods used in the construction of fabric trajectories and calculations, see section 1.3.3 and the appendix for the raw data. Table 2-5 show the measured results across three different cross sections.

Table 2-5: Calculated shear strain (γ) from the inclination angles (Θ) using equation [5]. Three cross sections were constructed and the distance [mm] from the foliation boundary (reference line) to each point on the isogons, where the inclination has the same value, was measured.

Cross section:		X_1		X_2		X_3	
Data series:		data1	data2	data3	data4	data5	data6
Θ	γ						
10	5,49	4,45	5,2	3,05	5,5	3,2	3,9
20	2,38	3,25	5,55	2,25	5,75	2,5	4,45
30	1,15	2,2	6,45	1,1	6,5	1,2	5,45
40	0,35	1,7	6,75	0,6	6,75	0,7	6,05

On the basis of data from the cross sections in table 2-5, a graphical presentation (diagram 2-2) illustrating the area in between the data series corresponding to that cross section, show displacement (e.g., area between data1+data2 show displacement in cross section X_1 etc.) within a shear band for the foliation in the Ersfjord granite.

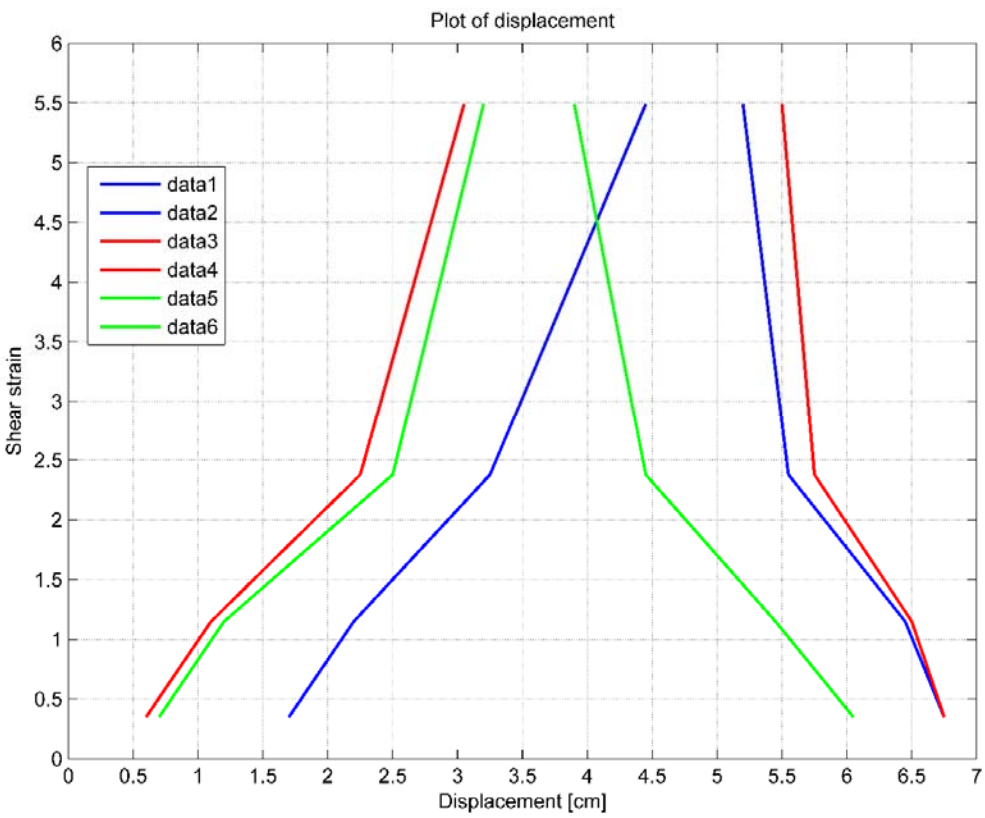

Diagram 2-2: The area in between data series with the same color show apparent displacement for a shear band within the foliation. The data is taken from Table 2-5. Cross section: X_1=data1+data2, X_2=data3+data4, X_3=data5+data6+data5$_{ext}$+data6$_{ext}$.

The apparent displacement was determined by box counting under the graphs, where the results are presented in table 2-6.

Table 2-6: The apparent displacement for the three defined cross sections, and calculated shear strain across the shear band.

Cross section	Width [mm]	Displacement [mm]	Shear strain [γ]
X_1	73	132,5	1,82
X_2	73	202,5	2,77
X_3	73	125	1,71

For determining the true displacement observed within the foliation in the study area, a scaling factor of 0,01493 (see 1.3.3.2) was applied to the calculated apparent displacements fromtable 2-6, resulting in actual displacements of:

Table 2-7: True displacement estimates for a single shear band within the foliation in the Ersfjord granite.

	Cross section	Displacement [mm]
D_{min}	X_3	1,87
D_{max}	X_2	3,00
D_{avg}	average	2,30
D_{median}	X_1	1,98

Using the results from the true displacement calculations for a single shear band, it was possible to infer a total displacement for the foliation in the study area. It is assumed that the finite shear strain is homogeneously distributed across the ductile foliation, on the basis of mesoscopic observations from section 2.2.2. The estimated true displacements represent a minimum value because locally the shear strain varies to some extent (table 2-6). On a mesoscopic scale the width of the foliation is quite constant, with minor variations up to a meter. These zones of thinning may be the source of the elevated shear strain values, resulting in larger displacements. The estimated total displacement for the foliation using D_{med} and a width of 7 meters is $\mathbf{D_{min} \approx 14m}$ with a maximum displacement up to $\mathbf{D_{max} \approx 21m}$.

2.4.2.4. Cataclastic failure

In the following section, microstructural evidence for high pore pressures equal to, if not exceeding, lithostatic pressure (σ_3) during cataclasis will be presented (figure 3-7) alongside shear strain calculations.

Using the data from table 2-8, obtained while identifying *displacement markers* in section 2.4.1 (figure 2-18), a minimum shear strain for the cataclasites were calculated according to the relationship given in section (1.3.3.3).

Table 2-8: Calculated minimum shear strain of cataclasite, following equation [8].

Displacement [mm]	**Width [mm]**	**Shear strain [γ]**
4,26	0,86	**4,95**

Comparing the ductile shear strain (section 2.4.2.1 and 2.4.2.3) with the cataclastic shear strain, it is apparent that bulk shear strain is 2-3x larger, which may be expected since brittle faults are commonly more localized.

The methods used for estimating the fluid flow velocity and the fault slip rates are presented in section 1.3.3.4. The basis for these estimations are the occurrence of injected ultracataclasites into protocataclasites (2.3.3;figure 2-12) and the occurrence of diluted k-fsp clasts within the fluids as discussed in section 3.2.3. The results are presented graphically in diagram 2-3. For injection of cataclasites, they need to be fluidized and must have been injected as the fractures opened or slipped. The slip-rates varies with the variable fluid density, but assuming the same density as Indrevær et al. of 1000 [kg/m^3] (Indrevær et al., 2014b), a value of c. 0,5-0,6 m/s (black- and blue graphs), for the 100µm grain size fraction, is obtained; whereas for the 50µm grain size fraction a value of 0,1-0,2 m/s (cyan- and magenta graphs) is obtained. It is very rough estimates, and as stated above, it may also reflect the slip rates. These values, assuming a fluid density of 1000 [kg/m^3], gives a value of c. 0,1-0,6 m/s slip rate.

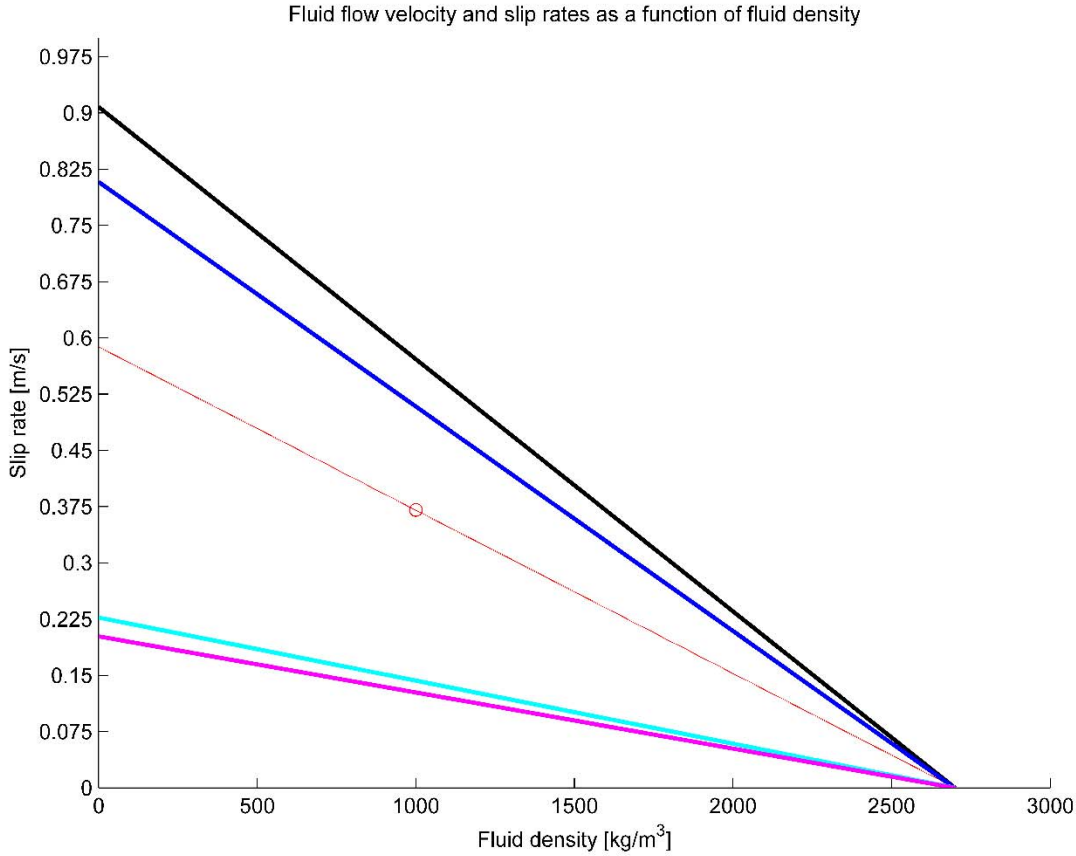

Diagram 2-3: The estimated slip rate of the cataclasites as a function of fluid density. (Black graph) Estimated at 350°C using a dynamic viscosity of 0,0648 centipoise and grain size of 100µm. (Blue graph) Estimates done for 350°C with a dynamic viscosity of 0,0728 centipoise and grain size of 100µm. (Red graph) Estimates done by Indrevær et al. (2014b), with a inferred fluid density of 1000 [kg/m^3]. Used as a basis of comparison. (cyan graph) estimations done using a grain size of 50µm and 0,0648 centipoise. (magenta graph) 50µm grain size and 0,0728 centipoise.

3. Part 3: DISCUSSION

3.1. Chapter 3.1: Introduction

This part will discuss the results obtained during study of the Ersfjord granite and associated dutile, semi-ductile and cataclastic shear zones, where mineral assemblages and fabric relationships will lay the basis for determining metamorphic conditions during deformation. A combination of mesoscale- and microscale observations are used to infer the sense of shear during deformation and, if possible, correlate shear zone development and structural evolution to established deformation events in the West Troms Basement Complex.

3.2. Discussion of petrography and structures

3.2.1. Alteration and precipitation assemblages

Pristine granites usually have a high quantity of biotite in the undeformed fabric, but this altered granite show less than 1%. Altered host rock due to progressive deformation is found throughout the strike of the shear zones and cataclastic zones. Large amounts of precipitated hydrothermal minerals combined with the characteristic red staining of the granite, implies that fluid flow along the fault zones may have been considerable (Indrevær et al., 2014b). The occurrence of epidote, chlorite and mica minerals are common where strain localized, whereas hematite and other iron oxides are widespread along brittle surfaces. Different types of minerals precipitate along surfaces, with changing temperature. During P-T conditions and fluid compositions characteristic for intermediate to deeper levels of faulting, mineral precipitation and hydrolysis of feldspars and mafic minerals are common (Bruhn et al., 1994), following these important chemical reactions:

(1) $3KAlSi_3O_8 + 2Ca^{2+} + H_2O = Ca_2Al_3Si_3O_{12}(OH) + 3K^+ + H^+ + 6SiO_2$
(K-fsp) (Ep) (Qtz)

(2) $3KAlSi_3O_8 + 5Mg^{2+} + 8H_2O = Mg_5Al_2Si_3O_{10}(OH)_8 + 2K^+ + 3SiO_2$
(K-fsp) (Chl) (Qtz)

(3) $Ca^{2+} + CO_2 + H_2O = CaCO_3 + 2H^+$
(Cal)

In reaction (1) K-fsp may be substituted with plagioclase as reactant (Bruhn et al., 1994). A change in temperature, pressure and fluid composition drives the reactions and controls which minerals precipitate. The *foliated fabrics (2.3.1.2)* and the *ductile shear zone (2.3.2)* have mineral assemblages that occurs when K-fsp, intermediate plagioclase, biotite and magmatic titanite are altered, in the presence of fluids, to more Albite-rich plagioclase, epidote, chlorite, and quartz, according to reaction (1) and (2). During these reactions excess ions are dissolved into the fluids and may precipitate as calcite (3), white micas, and/or iron oxides, or the ions may be transported with the fluid flow and precipitate at different sites.

Around retrograded biotite grains, chlorite, titanite and white mica occurs, which suggests that high temperature biotite contained some impurities in the crystal lattice (e.g., titanium; see figure 2-8 D for breakdown products). With decreasing temperatures, the crystal lattice cannot sustain high amounts of impurities, therefore they diffuse through the lattice and are dissolved in fluids; the fluids eventually precipitate new mineral phases.

Considering the abundance epidote and no occurrence of clinozoisite, this suggests an oxidizing alteration and/or precipitation environment. This is backed up by the fact that the iron oxide phase is hematite which contains Fe^{3+}-ions, the same that goes into the epidote structure. There are three possibilities for an iron enriched phase, either (1) the iron originates from dissolution of epidote and retrograding biotite during progressive deformation and/or from hematite precipitated within feldspar pores (red staining), (2) iron enriched fluids (e.g., through the Kattfjord Complex) infiltrates the host rock, (3) a combination of the prior suggestions where iron rich fluids infiltrates the host rock precipitating iron oxides, and simultaneously dissolves epidote and feldspar grains, sustaining the iron enrichment. During the cataclasis precipitation of iron oxides are abundant, usually as specular hematite along faults and fractures, which enhances the theory of an iron enriched fluid infiltrating the host rock during the brittle event. It seems most likely that, during cataclasis, permeability increases and large amounts of fluids may circulate through the volume of rocks along faults, fractures and lithological boundaries (e.g., towards the Kattfjord Complex), which makes the third possibility most plausible.

3.2.2. Petrographic constraints on alteration

Shear zones tend to localize because of an inherent instability such as a heterogeneity due to strain softening (Poirier, 1980) or extensional precursor structures (Segall et al., 1983; Simpson, 1986), this is likely because it requires less energy to localize along precursor structures than to

form new weak zones. In the studied Ersfjord granite shear zones, the existence of preexisting alteration structures was inferred based on prior mesoscopic observations (2.2.2) (e.g., a foliation truncated by obliquely localized shear zones and cataclasites). Generally, the difference in strain across a shear zone can result from (1) a gradient in the shear strain rate while the whole shear zone is deforming or (2) from localization of deformation in the internal parts at later stages of deformation (strain softening), or (3) temporal widening of the shear zone due to strain hardening, so that outer parts represent later strain increments. The third possibility can be excluded here because the shear zones seems to re-activate earlier fabrics and the fact that strain hardening in the center of the shear zones is very unlikely. This is backed up by the fact that the alteration products (3.2.1) are considered to be weak minerals that easily accommodates strain by dynamic processes. The two first possibilities are end members, where natural developed shear zones may result from a combination of both. A change in shear strain rate can be caused by a change of rate controlling parameters (e.g., SPO, permeability, viscosity and bulk diffusivity) or a switch in the controlling deformation mechanism. As most of these parameters in the Ersfjord granite shear zones are strain-dependent or developed during microstructural evolution (e.g., reaction products and SPO) it is assumed that developed structures along the strain gradient primary record progressive strain history (2). Implications based on this is that microstructures near the core of the shear zone primarily record later structures, whereas the microstructures near the margins represent earlier stages of deformation history. The weakening of the rock occurs toward the shear zone center caused by grain size reduction and phase mixing (increase of matrix) where the magmatic minerals are recrystallized to epidote, chlorite, white mica, calcite, quartz, and partly to albite and k-fsp.

On the other hand, if the shear zone was initiated by precursor structures (e.g., faults, micro cracks etc.), the whole rock volume must have been affected. The fact that shear zones are overprinted by elevated fluid circulation suggests that widening and propagation of narrow, cataclastic zones after ductile initiation is more likely. This implies that cataclastic failure may have developed during an abrupt strain increase and elevated fluid pressure, causing weakening effects and increased reaction rates (Kilian et al., 2011), further enhancing deformation.

3.2.3. Fabric relationships

Workers have shown that syn-tectonic granites often record a history of decreasing-temperature fabrics overprinting developed fabrics during pluton crystallization (Miller et al., 1994; Paterson et al., 1989; Tribe et al., 1996). The nature of developed fabrics is likely to reflect the

ambient thermal environment of the host rock during emplacement (Schofield et al., 1998). In the case of cooling paths for syn-tectonic bodies, it is necessary to establish the timing of deformation relative to the degree of crystallinity of the pluton i.e., fabrics corresponding to partial crystallization and crystal plastic strain, which defines two fabrics: (1) Those formed during magmatic flow where aligned crystals lie in an undeformed matrix, and (2) those formed during solid-state deformation (Hutton, 1988; Paterson et al., 1989).

To clarify, the definitions can be subdivided on the basis of the rheological critical melt percentage (RCMP), which separates fabrics dominated by free rotations within a surrounding melt (pre-RCMP), and those where stress is transferred across grain boundaries, through a framework of touching crystals (post-RCMP). Post-RCMP fabrics are formed entirely in a sub solidus condition with 10-50% estimated melt remaining, where solid-state deformation is dominant. Temperature regimes for controlling solid-state deformation are based upon different deformation processes for various constituent mineral phases (Tribe et al., 1996).

The undeformed Ersfjord granite is mostly homogeneous with preserved magmatic fabrics where large phenocrysts of k-fsp are hosted in a more fine-grained groundmass. Nearing the margins of the granite it contains sheared, mylonitized and local hydrothermally altered sections. These sections of deformation are recognized by a steeply dipping L-S fabric, defined by recrystallization of magmatic fabrics, and SPO of mineral aggregates along foliation, and alignment of phenocrysts, which are stretched out into the long axis of the finite strain ellipsoid. The L-S fabric indicates early deformation fabrics (e.g., flattening and constrictional strain), where the dextral shear zones and associated cataclasis represents subsequent overprinting. Similarly, the Ersfjord granite is internally cut by NNW-SSE dextral shear zones (figure 2-1) that seems to be related to the Late Carboniferous-Early Triassic rifting and opening of the North-Atlantic Ocean. The dextral (2.4.1) shear zones (2.3.2) contain S-C fabrics defined by intense deformation with stretched phenocrysts (σ-clast) defining sub-solidus grain scale dextral kinematic indicators, and where recrystallized chlorite and white mica defines a mineral stretching lineation (2.2.3).

One of the most important factors when assessing the fabric evolution is the relative amount of time the pluton takes to cool through a given temperature interval. Figure 3-1 illustrates possible time-temperature evolution paths for plutons emplaced into ambient host rock conditions. Initially the cooling path has a gentle slope reflecting the slow cooling of the pluton during assembly and infiltration, as magma is still being added and crystallization is taking place,

releasing latent heat. Once the pluton have solidified it will start cooling towards the ambient country rocks with greater thermal gradients, giving rise to faster cooling rates.

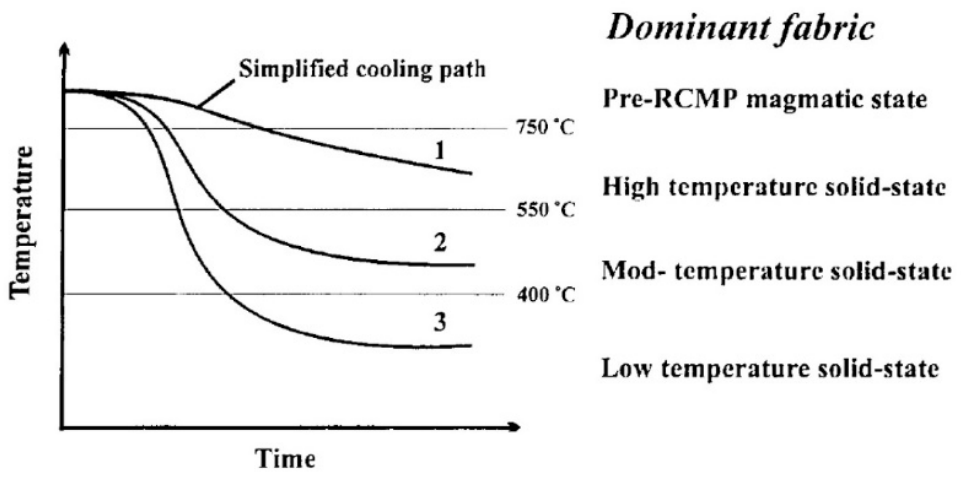

Figure 3-1: Relative time-temperature cooling curves, showing the retrograde temperature evolution paths for plutons emplaced into (1) high temperature (c. 750-550°C); (2) moderate temperature (c. 550-400°C); and (3) low temperature (c. <400°C) host rocks (after Schofield et al. (1998)) Abbreviation: RCMP=Rheologically critical melt persentage.

Considering a pluton emplaced at high ambient country rock temperatures will reside for an extended amount of time above 550°C. If continued deformation persisted with constant strain rates during cooling, the pluton would be dominated by fabrics formed at pre-RCMP and high temperature (>550°C) conditions. By comparison, a pluton emplaced into low ambient country rock temperatures would be dominated by pre-RCMP fabrics and low temperature solid-state fabrics, with little high-to-moderate temperature fabrics (Schofield et al., 1998). This seems to be the case for the studied Ersfjord granite, where high temperature pre-RCMP- and low temperature fabrics dominate.

3.2.3.1. Brittle-Ductile and Brittle-Plastic relationship

The remnant magmatic minerals are dominated by high temperature deformation microstructures and have deformed in a ductile manner, forming shaped fabric such as σ-shaped phorphyroclasts and shape preferred orientations. This early fabric is overprinted by later shear zones, resulting in S-C bands and the formation of abundant matrix, which seems to enhance deformation and recrystallization in the cores, reflecting the progressive strain history (3.2.2).

During pre-RCMP crystallization quartz and calcium-rich plagioclase start to crystallize together with K-fsp creating the poikilitic texture with quartz and plagioclase grains hosted within K-fsp phorphyroclasts. As the temperature decreases the high temperature plagioclase becomes unstable and start to pseudomorph into more sodium-rich plagioclase with intergranular growth of micas and epidote, creating intermediate poikilitic textures. This pre-RCMP crystallization is displayed as magmatic phenocrysts of k-fsp with lobate boundaries towards plagioclase. The K-fsp seems to be formed in a relatively low strain domain due to the high melt percentage (>50 %), where strain is accommodated through the fluid phase due to the melts much lower viscosity. Approaching the RCMP, more strain can be accommodated by the solid state due to the increasing interconnectivity of the crystals. Heterogeneities may become more important in accommodating deformation, because they enable easier slip (e.g., along micro cracks). During the relative high temperature, core-mantle structures may develop, SGR and GBM and sintering may occur, creating phenocrysts.

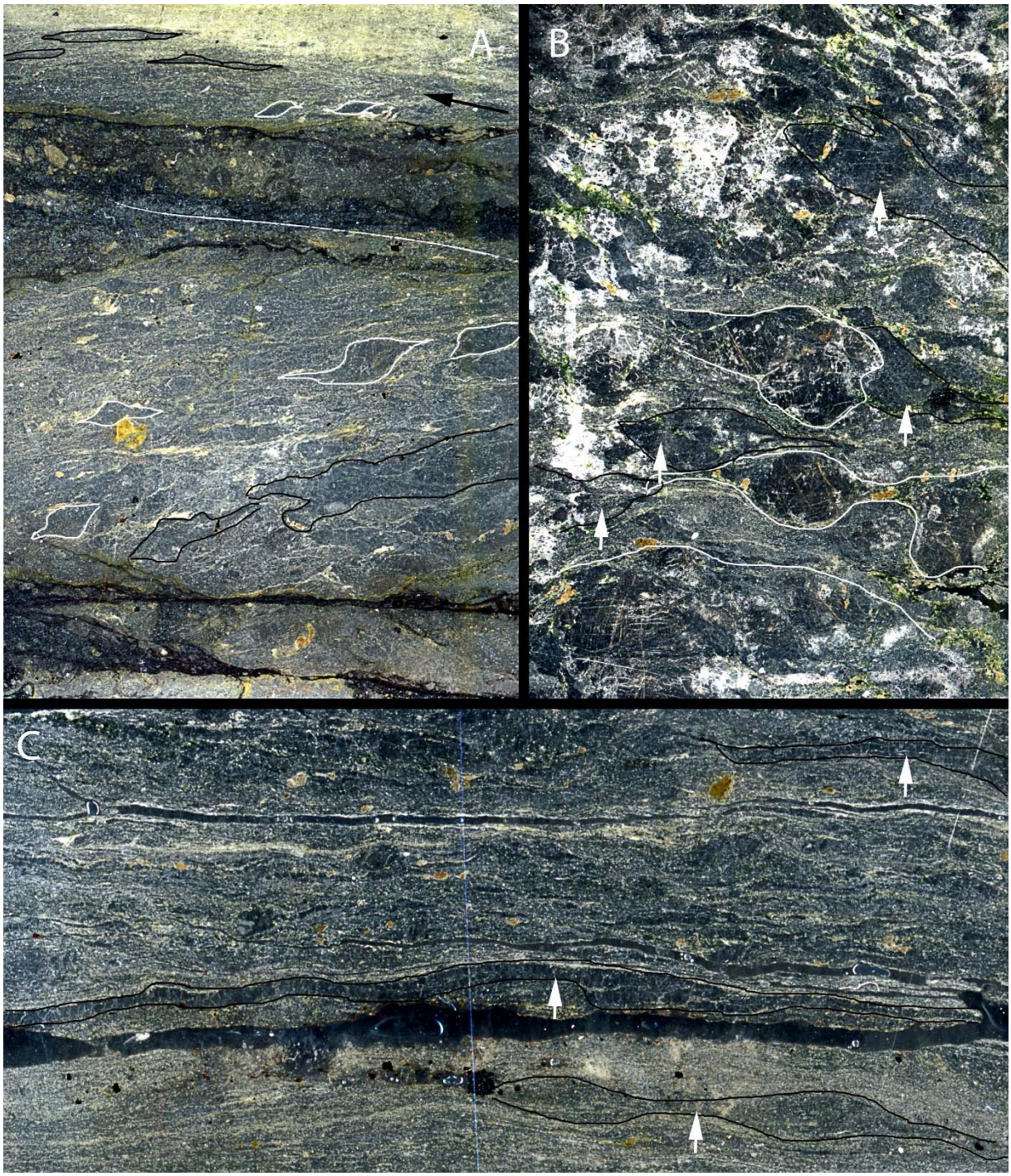

Figure 3-2: Micrograph of the dominant fabrics of the Ersfjord granite (scans of thin sections, plane light). Black areas are quartz aggregates (indicated with white arrow), and white areas are K-fsp. All examples displays dextral shear sense. (A) Cross section of a transitional frabric from mylonitic to ultramylonitic (the green area, indicated with a black arrow). Cataclastic zones truncate the ductile fabric. Phenocrysts of K-fsp displays dextral shear sense (masked white areas), qtz aggregate show elongation sub parallel to the shear bands, and parallel within the transition zone (masked black areas). Base of image=2,7 cm. (B) Section of less deformed fabric where remnants of high temperature textures are present. The viewed section of K-fsp phenocrysts makes up a network of interconnected crystals, white areas are recrystallized plagioclase into mica, and new plag grains. The quartz aggregates show slight elongation. Horizontal shear planes are present. Base of image=2,7 cm. (C) Mylonitic fabric illustrating boudinaged quartz aggregates and continuous monomineralic qtz bands (masked black areas) extending the whole width of the thin section. The bottom part show ultramylonite where qtz bands have thinned to a width of one grain, and are some places completely disintegrated, to form a part of the matrix. The big fracture is a flaw in the thin section. Base of image=3,5 cm. Sample: (A)=DP01_1, (B)=DP02C_3, (C)=DP12_3.

Solid state fabrics dominate below the RCMP, when melt percentage is above 10% and below 50%. High temperature post-RCMP fabrics include core-mantle structures, where k-fsp phenocrysts seems to dynamically recrystallize to form a mantle with surrounding small grains. Intermediate plagioclase seems to replace k-fsp due to the instability of K^+ and Na^+ in the crystal lattice, creating a perthitic appearance. Early microfractures have developed in feldspars (Olesen, 1987), this is evident from the many generations of healed microfractures (figure 2-16 E-H). The recrystallization along these microfractures sometimes result in disseminated phorphyroclasts with strain free quartz and albite along the microfractures (figure 3-4 A-B). K-fsp also develops lobate myrmekitic intergrowth with quartz (figure 2-8 A, E, G). Plagioclase show ductile bending of the twins (figure 2-8 H), and micas show fish structures (figure 2-17 A). These high temperature solid-state deformation structures represents the ductile and plastic regimes, where dynamic recrystallization is dominant (i.e., the minerals do not fracture), but can be shaped with respect to the local stress regimes.

The moderate-to-low temperature post-RCMP fabrics have overprinted the high temperature structures, and are dominant throughout the samples. Quartz shows subgrain- and grain boundary migration features, such as heterogeneously distributed strain, which enhances deformation. These strain differences may also play a role in the transition from ductile to brittle deformation. As temperature drops, the minerals can accommodate less strain before brittle failure is reached, resulting in cataclasites (rock fragments within a matrix), or a semi-ductile behavior where the onset of shearing is controlled by fracturing, where the formed clasts deform plastically within the fluid phase (figure 3-3). This illustrates the brittle/plastic relationship where clasts are formed by cataclasis at the propagating fracture tips and deformed plastically within the shearing fluid. This may happen because of viscosity contrast between the fluid phase and the clasts, which have approximately the same temperature as the ambient rocks (i.e., greenschist facies; low-to-moderate cooling gradients; figure 3-1). With the widening of the shear zones the shear velocity increases and thus applied shear stress increases, causing more deformation of the clasts. The clasts will flow like liquids, though very slowly, and are therefore described as being viscoelastic.

Figure 3-4 A-B illustrates k-fsp phorphyroclasts initially deformed by brittle fracturing where precipitated quartz and epidote have mixed along these fractures. The phorphyroclasts also show signs of flame perthite enhancing the theory of fluid circulation and high pore pressure. Figure 3-4 C show an overview look of plastic- and fluid-phase mixing, where the fluids seems to shape the plastic clasts.

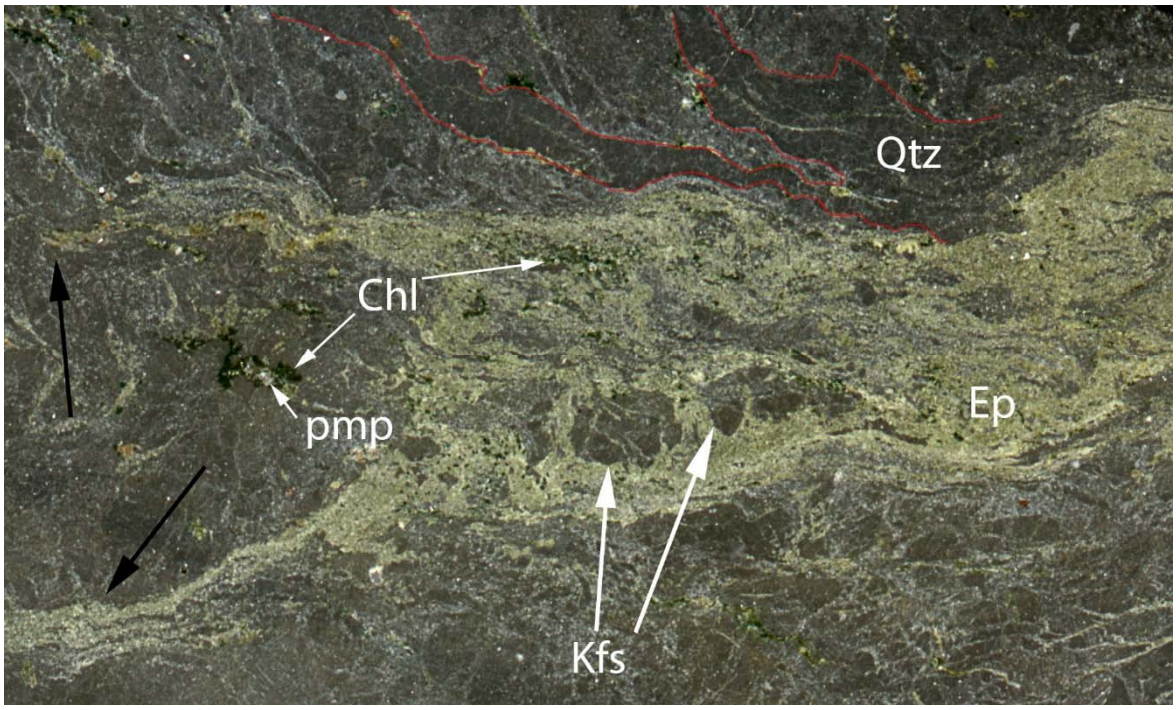

Figure 3-3: Micrograph scan across a brittle/plastic regime. Black arrows represent areas with fluid infiltration into brittle fractures, propagating the cataclastic zone. Kfs clasts (white arrows) deforming plastically within the propagating fluidized (abundant Ep) zone. Qtz aggregates are stretched and boudinaged, because it being the strongest phase (red areas). Chl precipitate along fractures and within the fluidized zone. Pmp precipitate in association with chl+ep+fluid. Base of image=3,5 cm. Sample: DP07_1

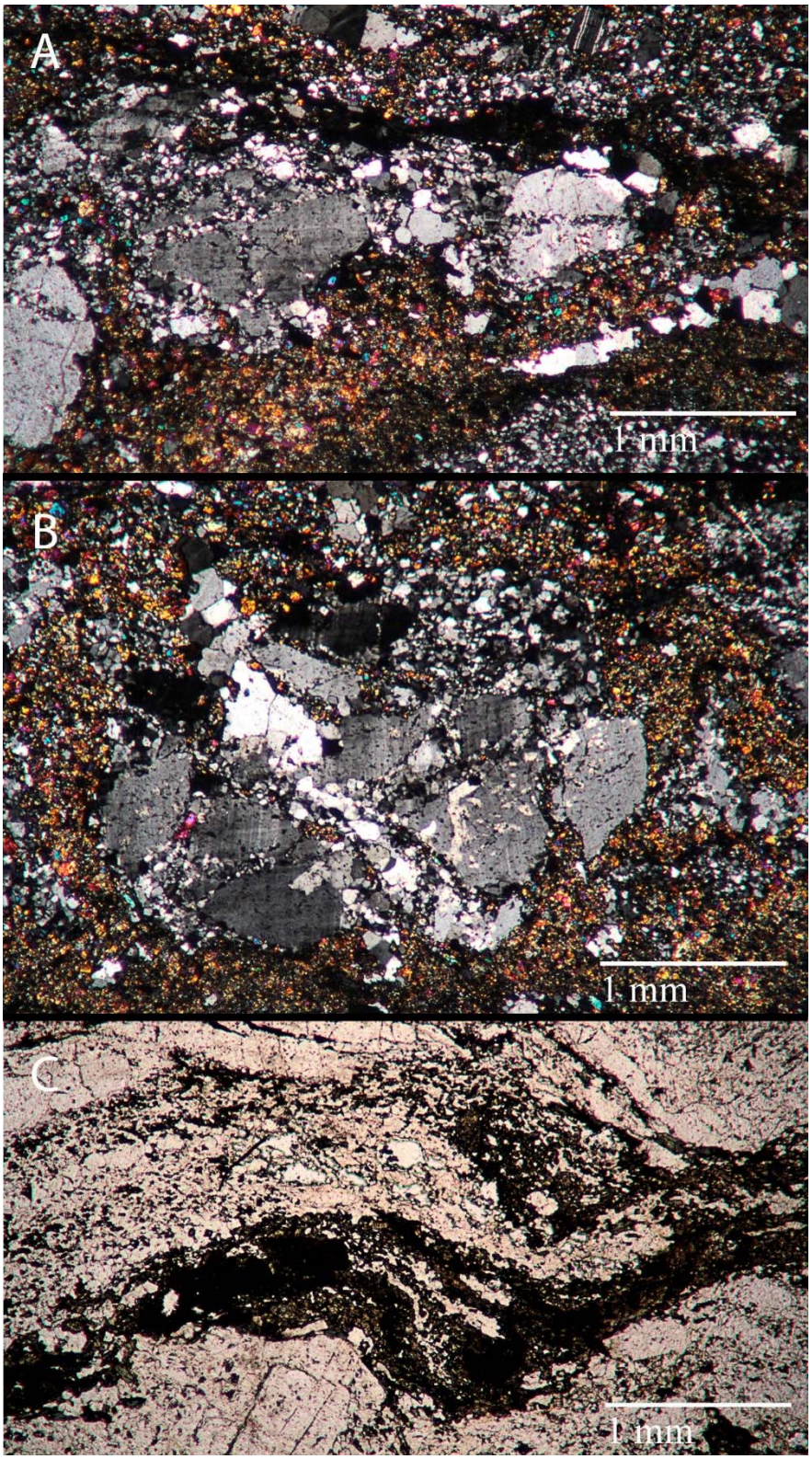

Figure 3-4: Micrograph of initially semibrittle clasts deforming plastically. (A) Clast of K-fsp deforming initially by brittle fracturing, then plastically by dynamic recrystallization into new k-fsp and qtz. (B) Possible hydrofracturing and dilution in phorphyroclast K-fsp due to high pore pressure and precipitation of qtz along fractures. Flame perthite texture on k-fsp further suggests hydrothermal alterarion. (C) Overview of plastic deformation of clasts within a fluid phase. Scale is the same for all micrographs. Sample: DP07_1

3.3. Chapter 3.3: Strain analysis and deformation mechanisms

This chapter discusses the microscopic and mesoscopic elements identified in association with the shear zones in the Ersfjord granite. The mesoscopic elements will be discussed in close relation to the microscopic observations, in order to shed light on the strain history.

The solid state flow of rocks is commonly simulated by extrapolating steady state laboratory flow laws for monomineralic aggregates to natural strain rates and temperatures in the lithosphere. This is valid if one mineral phase is sufficiently weak or abundant with respect to the other minerals to actually control the rheology of the rock, and if the microstructure and rheology of the rocks do not vary greatly with strain (Handy, 1990). The fabric of the Ersfjord granite develops sigma shaped clasts of K-fsp in a weaker quartz, feldspar, and white mica matrix, this rheological setup reflect Handy (1990) domain 2 and domain 3 rheology (figure 3-6), where near all strain is accommodated through the matrix due to the mineral strength contrast (>10:1,figure 3-5). Once a steady state microstructure is developed (e.g., reactions have completed or grain sizes are stabilized), further strain or temperature differences can change the strength contrast between constituent minerals. For example, figure 2-10 A-B, 3-5 and 3-6 show incipient dynamic recrystallization of the domain 3 microstructures, where K-fsp (strong phase), is recrystallized to form weak phase minerals such as quartz, albite, epidote, chlorite (i.e., retrograde reactions in section 3.2.1), resulting in more matrix. This produces a change in the rheology and the strength contrast (figure 3-6 B-C) where the initially weaker quartz is boudinaged, and so the fine grained reaction products (e.g. mica and epidote) in the matrix are inferred to be weaker. These reactions result in a switch from domain 3 clast-matrix behavior to domain 2 boudin-matrix behavior. A consequence of this evolution is that the load-bearing framework rheology (i.e., strong phase of k-fsp phorphyroclasts) is suppressed, and therefore drastic strength drops are observed in the Ersfjord granite (i.e. strain softening; figure 2-22), as a result of breakdown of the unstable phorphyroclasts.

Ductility is enhanced during grain size reduction via dynamic recrystallization of the weak phase with respect to the strong phase. This results in greater accommodations of strain into the weak phase and thus exerts a disproportionately large weakening effect on the bulk strength of the aggregate. Low flow stresses and high fluid pressures seem to induce brittle failure and to reduce bulk strength of the phorphyroclasts. The observed effect of the stresses exerted on the

bulk rock is the foliation. It is a product of reducing the size of stronger, less active phases (e.g., K-fsp phorphyroclasts), so that their average spacing is increased. The result is an increase in the amount of matrix grains surface area in contact with the surfaces of other matrix grains. The increase in contact decreases the stress concentration in the weak matrix, therefore reducing the energy expended on the aggregate for a given increment of strain and consequently decreasing the strength of the matrix (Handy, 1990).

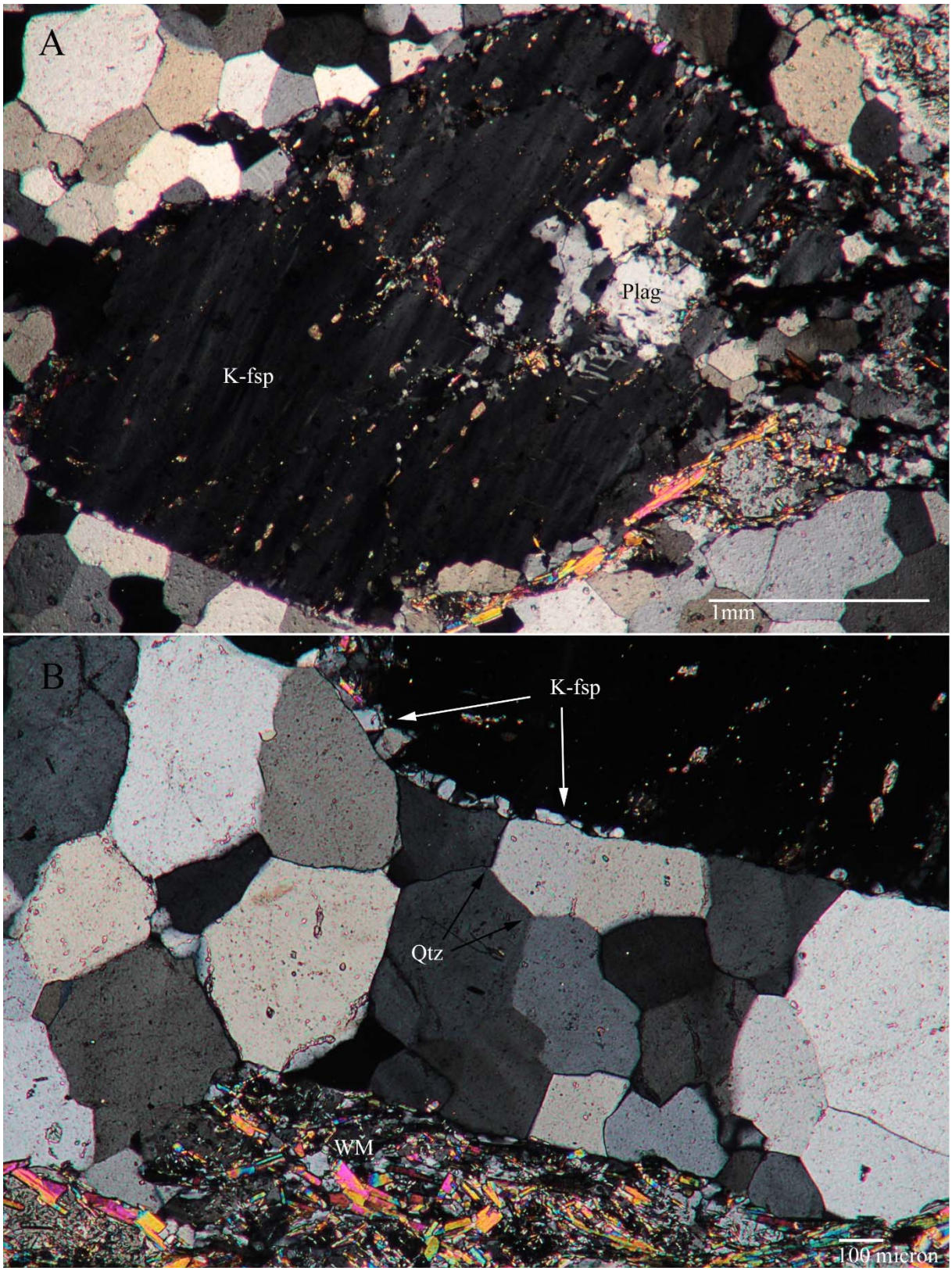

Figure 3-5: Micrograph of K-fsp phorphyroclast within a completely recrystallized qtz layer. (A) K-feldspar grain illustrating the strength contrast, where surrounding qtz are recrystallized due to strain partitioning into the weaker phase. (B) Close up of (A); the K-fsp clast shows small, dynamically recrystallized grains (white arrows) formed by local stress concentrations, whereas the surrounding qtz aggregate is statically recrystallized, forming straight grain boundaries and triple junctions (black arrows).

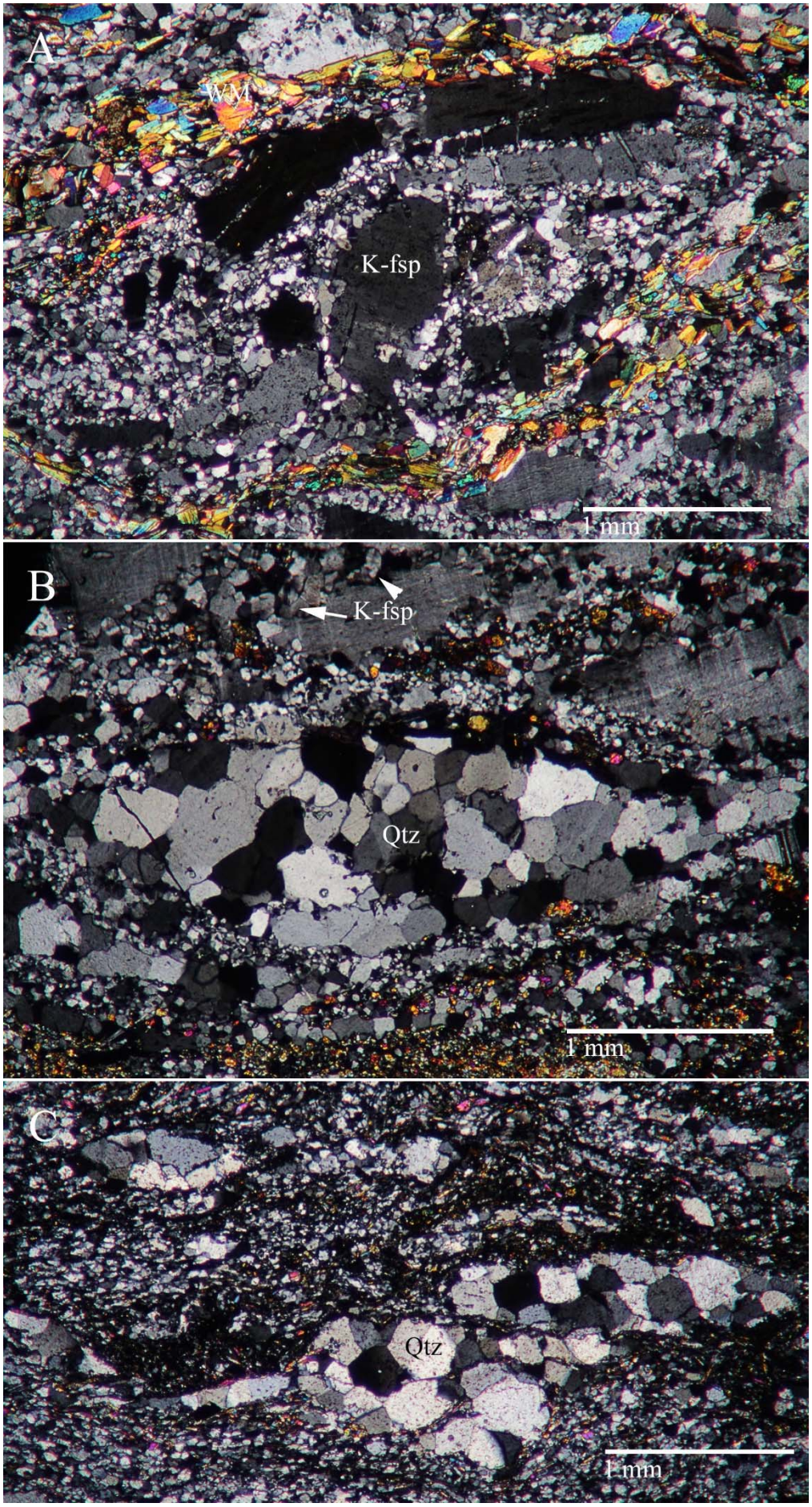
A
WM
K-fsp
1 mm
B
K-fsp
Qtz
1 mm
C
Qtz
1 mm

Figure 3-6 (Prev. page): Micrograph of microstructural changes during discontinuous deformation, showing a transition from domain 3 to domain 2 rheology. (A) Dynamically recrystallized matrix of qtz, albite and white mica containing k-fsp clasts undergoing neocrystallization. (B) Elongated qtz boudin surrounded by reaction products. K-fsp recrystallizing to matrix minerals. (C) The initially weaker qtz in Figure 3-5 is now slightly stronger than the neocrystallized matrix.

3.3.1. Ductile shearing

The kinematic pattern of the structures seems to be characterized by a polyphase strain history, reflected by the early developed foliation, the through going ductile shear zones, and the cataclastic event(s). Each of these phases seem to have developed significant inhomogeneity within the Ersfjord granite, and may reflect kinematic changes during evolution.

The ductile foliation in the Ersfjord granite is tentatively interpreted as late Paleoproterozoic deformation fabrics (1.2.2.5; table 1-1), mainly caused by NE-SW contraction during upper greenschist facies deformation at >15 km depth, in conjunction with an increased transpressive component, along the Paleoproterozoic crustal margin (Armitage et al., 2005; Bergh et al., 2010). The contact between the Kattfjord Complex and the Ersfjord granite is mylonitized by sinistral strike-slip shear zones (Bergh et al., 2010), which show the same kinematics as the Senja shear belt and the Mjelde-Skorelvvatn shear belt (figure 1-3). The contraction produced a 7-8 meter wide and weak zone, defined by L-S fabric (3.2.3), which accommodated displacement up to 10's of meters (section 2.4.2.3). This early ductile fabrics show signs of fluid circulations, which may be explained by either meteoric fluids derived from the upper continental crust during orogen parallel shortening or from fluid circulation along the lithological boundary.

The mesoscopic observations (2.2) and microstructural results (2.3) supports that the studied fault zones have acted as fluid conduits during shearing and faulting, precipitating epidote, chlorite, hematite and calcite along the shear zones. The precipitated minerals reflects the persisting greenschist facies metamorphic conditions during shearing and faulting. Fluid infiltration is initiated along plagioclase grains where chemical disequilibrium causes recrystallizing to micas during retrograde conditions (figure 2-8 D). The intermediate plagioclase are chemically unstable at lower temperatures and readily alters to other mineral phases (section 3.2.1), enhanced along grain boundaries and cleavage planes where fluids infiltrate. As this process continues and more mica is formed, fluids follows these zones of alteration, resulting in continuous bands of mica and reaction products from the deformation of

the host granite. The studied fault zones show evidence of fluid flow within both the interior- and marginal zone, where a network of mica bands witness that fluid circulation in the core must have been considerable, at least periodically. Mesoscopic observations around the dm-thin shear zones, bear witness to subsiding fluid circulation distally from the shear zones, illustrated by the red stained granite. This may be a result of fluid circulation during the formation of the foliation, which surrounds the shear zones on both sides, or it may be a more restricted fluid flow, compared to the fluid flow along shear zones and veins, possibly occurring along grain boundaries and/or smaller fractures (figure 2-16 E-G) reflecting the early stages of cataclastic failure seen in the K-fsp phorphyroclasts. This observed contrast of alteration in the two different fluid domains, suggests that fluid flow may not have been simultaneous, and thus reflects different stages in deformation.

The strain softening processes constrained during strain localization along the preexisting Paleoproterozoic foliation developed through going shear zones, with distinct characteristics for reactivation of the earlier weak fabrics. This can be seen from the slight difference in strike and the almost coinciding dip (figure 1-6; 2-6 A). Since the planar fabric of the foliation mainly consists of platy mica minerals, where easy slip is enabled along their basal axis, strain is accommodated parallel, resulting in a dip coinciding with the foliation. The slight difference in strike may be a result of heterogeneities along the preexisting fabric, which enables easier slip at a slight angle. These asperities may have been interconnected rheological inactive k-fsp phorphyroclasts, deflecting the propagation of the shear zone, or shear bands transferring the propagation from one foliation layer to another, or microcracks, or elevated porosity; each of these differences are capable to changing the direction of propagation, because deformation propagates along the way of easiest slip.

During progressive deformation a finite strain history develops, which is documented through this work (2.4.2). Recrystallized quartz aggregates was used to calculate the flow stress and the strain rate during deformation. The low values obtained for strain rate ($<10^{-15}$) is very unlikely during formation of mylonites (see section 3.3.1.1), and suggests that static recrystallization have been active during progressive deformation. This is recognized by the large grain size fraction (>78 µm <300 µm) measured, and backed up by the straight grain boundaries and triple junctions in the quartz aggregates (figure 2-10 F, 2-16 A-C, 3-5 B).

Indications for shear sense was first observed during field work, where a quartz vein was dextrally displaced by a series of thin fractures (figure 2-5 A), and later established by

microstructural evidence (section 2.4.1) for the ductile shear zone. The first assumption made regarding the sense of shear for the ductile shear zones, assuming the same kinematics as the displaced vein, was that these shear zones were connected to a compressional event (e.g., the Caledonian orogeny). Taking into account the mineral stretching lineation, with a trend and plunge of 312/28 (figure 2-6 B), the shear zones classify as oblique-convergent with a strike-slip component being dominant over the dip-slip component. This sense of shear coincides with a compressional environment such as could be expected from an orogeny.

Although this sense of shear could be caused by an orogeny such as the Caledonian, the mineral assemblages and deformation observed reflect pressure and temperature conditions that occur much shallower. In order to identify the metamorphic conditions to which the present day surface would have been subjected during the Caledonian; the depth of the shear zones were extrapolated backwards in time using the following assumptions:

1. The present surface was at a depth of 11km at the start of rifting (2.3.3)
2. Exhumation occurred at a rate of 40m/Ma; this was calculated by Indrevær et al for the outer islands of the WTBC during the rifting interval (Indrevær et al., 2014b)
3. The exhumation rate has been constant from at least the time of the Caledonian through the time of the rifting

It was determined that, if the metamorphism were to have occurred in association with the Caledonian Orogeny, the present-day surface would need to have been at a depth of at least ~19km. This would place it in the upper amphibolite facies based on the geothermal gradient that were established in section 2.3.3.1. Although the samples contain remnants of the amphibolite facies (biotites, as described in 2.3.1), the dominant mineral assemblages are those of the greenschist facies (outlined in sections 2.3.1 and 2.3.2 and discussed in 3.4); using the geothermal gradient of 30°C/km (2.3.3.1), these would be formed at depths of ~11km (290MPa). Because of this, it is believe that the dominant metamorphic facies minerals were formed in association with the rifting, while the remnant amphibolite facies minerals are associated with earlier metamorphism or were initially present in the pluton protolith itself.

3.3.1.1. Static recrystallization during progressive deformation

Grain size differences can be explained through rate of mechanical work and the ability of the rock to either dissipate or store energy. When the bulk strain rate is dominated by diffusion creep, the quartz aggregates grow at the same rate that occurs by normal grain growth under

isostatic conditions. When the dominant deformation mechanism is dislocation creep, the matrix grain size is reduced at a rate that varies directly with the product of stress and strain rate. This relation is independent of whether the rate-controlling mechanism of recrystallization is subgrain rotation or grain boundary migration. Thus, reduction rate is proportional to mechanical work rate (Austin et al., 2009):

$$\dot{W} = \sigma\dot{\varepsilon} \qquad [13]$$

where $\dot{W}$ is mechanical work per unit volume (*power*), σ is flow stress and $\dot{\varepsilon}$ is strain rate.

This mathematical relationship suggests that the grain size gradients observed in natural deformed shear zones would not require a change in flow stresses, but could be a product of strain softening (figure 2-22 B), resulting in locally elevated strain rates under constant stresses.

The rate of dissipation are dependent on the relative partitioning of energy between diffusion creep and dislocation creep, and the efficiency of each process. It is assumed that all *power* derived from diffusion creep is dissipated. If inputted *power* is accommodated only by diffusion creep, grain growth rates are not modified, whereas if some portion of the inputted *power* is partitioned into the material microstructure (e.g., qtz aggregates) increasing the internal free energy during dislocation creep, static recrystallization may occur (Austin et al., 2009; Austin et al., 2007). Both experimental observations, and theoretical considerations suggest that the proportion of energy stored in the microstructure may vary between 0-40%, depending on materials, strain, strain rate and temperature (Austin et al. (2009) and ref. therein).

Thus grain size evolution during deformation seems to be controlled by the relative contribution of dislocation creep and diffusion creep. When stresses are relatively low (table 2-4) and assumed constant throughout deformation, grain aggregates undergone dislocation creep may have grain boundary energy stored in the microstructure, causing static recrystallization which is dictated by mechanical work done per unit volume $\dot{W}$ [13] during deformation. Considering that the high strain areas are deforming by diffusion creep (e.g., figure 2-22; interior of shear zones), all mechanical work rate [13] is dissipating (e.g., heat loss), suppressing grain growth in the matrix.

Grain growth during progressive deformation is thus possible if considering the mechanical work rate, and storing of grain boundary energy in the qtz aggregates, resulting in grain growth simultaneously as the matrix deforms. For instance, if the quartz aggregates is generating dislocations during deformation, the internal free energy of the qtz is increasing, and thus, it

would try to compensate with grain growth through grain boundary area reduction (GBAR) (Passchier et al., 2005), lowering the internal free energy. This only happens if the rock is capable of storing dislocation creep energy, and thus requires diffusion creep to accommodate the bulk deformation. If the deformation were accommodated through dislocation creep processes, the internal free energy would be brought towards equilibrium because it is much more efficient than GBAR, and limited static recrystallization would occur. This explains the abundance of static recrystallization microstructures in the quartz aggregates (figure 2-8 B; 2-10 F; 2-16 A; 3-5), and further explains the slow strain rates and relatively low flow stresses calculated (table 2-4). Considering the difference in grain sizes from the margin and the interior of the shear zones (table 2-3), it is obvious that the marginal areas were exposed to prolonged static recrystallization, which is a direct result of the strain softening and concentration of strain accommodation in the interior of the shear zones (figure 2-22).

3.3.2. Semi-ductile to brittle faulting

Pore pressure is one of the controlling factors of crustal strength where increasing pore pressure will effectively decrease the confining pressure (i.e., overburden pressure) resulting in weakening of the affected rock. Depending on the differential stress, fracturing will occur perpendicular and/or parallel to foliation as pore pressure approaches lithostatic values (Lucas et al., 1995).

For minerals to precipitate on faults- and fracture surfaces, the fluid pressure must have exceeded the normal stresses acting on the fracture plane. Normal stresses acting on a surface varies with its orientation in relation to the stress field and, is at a minimum for surfaces normal to σ_3. Resulting in a pore pressure that need to equal the confining pressure in order to open fractures.

Figure 3-4 A-B illustrates a k-fsp phorphyroclast that show evidence for fracturing and dilation of the clast, interpreted in the form of fracturing and injection of fluids and precipitation of quartz. The flame perthite enhances the theory of fluid circulation. In order to inject fluids and dilate the clast, the pore pressure needs to equal or exceed the confining pressure. Injection of ultracataclasites into protocataclasites (figure 2-12) is perhaps a more reliable argument as it requires that pore pressure were sufficiently high for opening veins during deformation. As a minimum, pore pressure must have reached lithostatic values. Radial growth, and thus post-

faulting, of chlorite within the semiductile and cataclastic fabric suggests that it has grown into open pore spaces (figure 2-10 G, 2-16 E-F). For pores to exist at depth, the pressure must have been equal to the confining pressure, as a minimum.

At temperatures of minimum 350°C during early stages of faulting, as inferred from the mineral assemblage and dominating subgrain rotation recrystallization microstructures, quartz should dynamically recrystallize through grain boundary bulging (figure 2-21), regime 1 after Hirth et al. (1992). Quartz in the studied fault zones show undulatory extinction, but completely lack dynamic recrystallization microstructures, which suggests that either strain rate was high ($>10^{-12}s^{-1}$), or that fluid pressures were elevated in order to induce fracturing as seen in the k-fsp (figure 2-16 E-H), and in qtz (figure 2-18). If strain rates were to exceed $10^{-12}s^{-1}$ it would require differential stresses of more than 300 MPa at c. 350°C, following qtz flow law from Stipp et al. (2002a). Such build-up of high stresses are expected to produce some crystal plastic deformation, but the complete absence of such microstructures suggests that the studied rocks in this area of the Ersfjord granite quickly reached critical stress state, most likely of elevated pore pressure (Indrevær et al., 2014b).

Pressures indicated for early stage faulting at c. 350°C, extrapolating the established maximum geothermal gradient of 30°C/km (figure 2-14), yields a depth of c. 10-11 km depth, which corresponds to minimum pressure of c. 290 MPa during early stages of faulting. Based on the results presented above about pore pressure, a minimum estimate is inferred to 290 MPa during early stage faulting. A common Mohr-Coulomb failure criteria was calculated to illustrate the effect for high pore pressure on the rock (figure 3-7). Differential stress was calculated to 40 MPa. This result coincide closely with the calculated flow stress during ductile shearing (table 2-4).

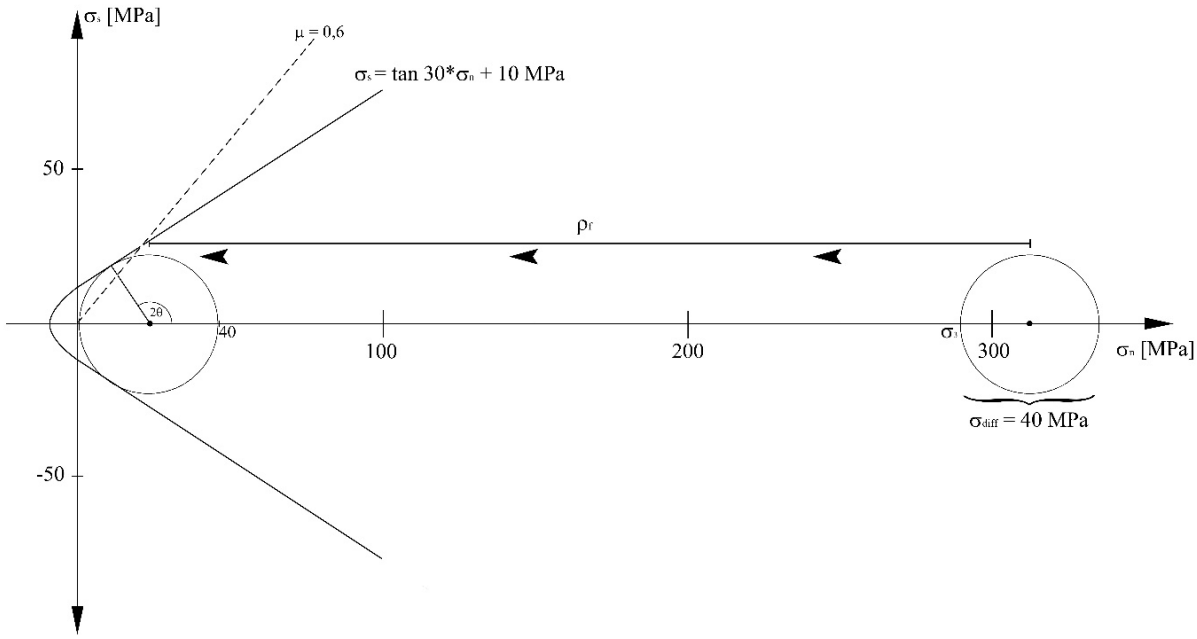

Figure 3-7: A common Mohr-Coulomb failure criterion. Stippled line represent a common frictional coefficient for rocks. Calculated stress conditions during faulting, where the evidence for lithostatic pore pressure (σ_3=290 MPa) suggests that the differential stress did not exceed c. 40 MPa.

The cataclasis is at least partly controlled by frictional gliding (section 2.3.4.2). Where elevated pore pressures bring the state of stress to a critical level causing hydro fractures, either parallel and/or perpendicular to the existing foliation (figure 2-16 E). This results in an abrupt drop in the pore pressure, bringing the state of stress below the critical fracturing point, enabling easier frictional gliding than continued faulting. As this frictional gliding process comes to a halt, cementing processes in the damage zone can effectively seal off parts of the fracture system, which brings temporal changes to the fluid flow and brings the pore pressure up to critical levels again, causing more fractures. This very dynamic process may have repeated itself, nucleating over a regional area (figure 1-2), as witnessed in the Rekvika fault zone, Tussøya fault zone, Bremneset fault zone and Kvaløysletta-Straumsbukta fault zone (Antonsdóttir, 2006; Indrevær et al., 2014b; Koehl, 2013). A common feature for all of these fault zones, and related fractures, are hydrothermal alteration and precipitation of epidote, quartz, chlorite, calcite and hematite along fracture surfaces, and in the matrix of the cataclasites. Cross-cutting relationships, such as shown in figure 2-16 E-F, illustrates that hydro fractures formed first and may have enabled frictional gliding, and were later cut by extensional fractures composed of qtz±chl±ep±hem associated with late stage cataclasis. At least two generations of cataclasites were identified (section 2.3.3; figure 2-12). Both cataclasites show the mineral assemblage

qtz+fsp+ep+chl+ttn+hem±ap±cal±wm (Table 1-3). Pumpellyite (figure 2-9 and 2-13) got introduced when the P-T conditions allowed reaction between ep+chl+fluid forming pmp+fluid during subsequent fracturing and cataclasis.

3.4. Mineral assemblage and metamorphic conditions

The protolith to the mineral assemblages is the massive Ersfjord granite, and covers about 80% of the northern Kvaløya (1.2.3.1), it is mostly homogeneous, with local heterogeneities such as strain localizations and hydrothermal alterations (3.2.1).

During optical microscopy study it was possible to determine the mineral fabrics (2.3.1, 2.3.2, 2.3.3) for four different metamorphic conditions, resulting in a retrograde metamorphic evolution. These fabrics can be divided into groups based on the majority of microstructures observed. (1) The first type of fabric is where microstructures of the *ductile fabric (2.3.1.1)* dominates. Samples containing this type of fabric were associated with foliation bands anastromosing around layers of rheologically inactive feldspar phorphyroclasts. (2) The second type of fabric is dominated by foliation bands (2.3.1.2). (3) The third fabric is dominated by mylonites (2.3.2.1), and ultramylonites in the cores of the ductile shear zones. (4) The cataclasites (2.3.3) is the final fabric, reflecting the change from ductile deformation to brittle fracturing.

(1) The minerals dominating this fabric are mostly dynamically undeformed k-fsp phorphyroclasts that show signs of diffusion through the crystal lattice, resulting in formation of perthite. Further quartz and plagioclase grains occur inside some phorphyroclasts, this is interpreted as magmatic growth during the crystallization of the pluton, and reflects the pre-RCMP fabric (section 3.2.3). Since the formation of perthite requires diffusion of ions through the crystal lattice, it is dependent on time, which suggests that either magma was being added through an extended period of time, or that magma intruded into high temperature ambient rocks (section 3.2.3 and figure 3-1), giving rise to an initially slow cooling gradient. Dynamic recrystallization fabrics developed during cooling, which includes myrmekite (plagioclase breakdown and reaction with quartz and k-fsp), and neocrystallization of plagioclase, forming mica and epidote. K-fsp and plagioclase may have undergone minor recrystallization through subgrain rotation recrystallization and grain boundary migration (figure 2-8 E, G, H; 2-10 D), whereas quartz dominantly deforms

by dislocation creep (figure 2-8 B-C). Implications based on this fabric is that the Ersfjord granite intruded into low- to moderately temperate ambient rocks (figure 3-1), because of the dominating retrograde reactions, the readily recrystallizing plagioclase, and the lack of biotite. The studied heterogeneities were most likely subjected to retrograde deformation.

(2) Foliation bands have a mineral assemblage of epidote+quartz+albite+chlorite±white mica±titanite±apatite±calcite, reflecting greenschist facies metamorphic conditions during strain localization, and is considered a transition from a clast-bearing fabric to a boudin-matrix behavior, where a switch in strength contrast occurs. In this type of fabric a continuously generation of matrix results in a switch in the dominant deformation mechanism, from dislocation creep of the aggregates too diffusion creep in the matrix

(3) The greenschist facies assemblage is also present throughout the ultramylonites, suggesting persisting greenschist facies metamorphism with progressive deformation. The majority of the mineral assemblage throughout the deformed areas suggests that the studied area cooled relatively fast towards the ambient country rock temperatures, at c. 400-500°C, resulting in two dominating fabrics: 1. pre-RCMP- and 2. low temperature post-RCMP fabrics, enhancing the theory of an extended magma infiltration into an low/moderately temperate ambient host rock. In this phase, grain size equilibrium is reached of c. 20 µm and deformation is accommodated through diffusion creep processes such as granular flow and pressure solution precipitation. The qtz monomineralic layers are either folded or disintegrated, and some rheological inactive quartz boudins/aggregates are statically recrystallizing, due to the ability of storing deformation energy through active dislocation creep processes.

(4) Minerals found throughout the cataclasites are abundant epidote, heamatite and chlorite; in which the clasts contain minerals and fabric from the earlier ductile deformation. Chlorite show radial growth, and epidote show idiomorphic grain boundaries. Where both observations suggests persisting greenschist facies conditions during deformation. The presence of greenschist facies minerals inside the cataclasites is indicative of a minimum temperature during formation at c. 350°C, based on the observed microstructures and mineral assemblage. Epidote grains showing idiomorphic grain symmetry indicates that greenschist facies temperatures were reached prior to fracturing. Undeformed radial growth of chlorite inside the cataclasites suggests that these conditions persisted throughout early events of brittle deformation.

Later fault movements introduced more hydrothermal fluids into the system (figure 3-3), initiating chemical reactions between existing chlorite and epidote, resulting in the formation of reaction haloes around the epidote grains, comprised of pumpellyite (figure 2-13 B). Pumpellyite is a sub-greenschist facies mineral and forms at temperatures ranging from c. 250-300°C, suggesting that temperature conditions decreased below c. 300°C during late stage faulting.

3.4.1. Metamorphic conditions

Microscopic results obtained during this study are the main basis for determining metamorphic conditions. Estimates of depth and shear zone formation (P-T conditions) was established by focusing on deformation mechanism, mineral assemblage and timing of deformation in the shear zones. It is observed four different deformation conditions which can be used to infer a P-T-t path. The high temperature pre-RCMP (>650°C), which may relate to the crystallization of the Ersfjord granite, high temperature post-RCMP (>500°C) fabrics produced during increased cooling towards ambient country rock temperatures, thus leaving little evidence, and the low temperature post-RCMP (<450°C >300°C) fabrics. Low temperature fabric dominates throughout the Ersfjord granite shear zones, indicating that the majority of the ductile deformation happened through greenschist facies metamorphism close to the brittle-ductile transition. The presence of pumpellyite suggests a minimum temperature of c. 275°C, corresponding to the lowest stability field of 220 MPa (8-8,5 km depth) during late cataclastic movements (section 2.3.3.1 and figure 2-14).

Quartz grains within the interior of shear zones recrystallized into sizes expected for subgrain rotation mechanisms for temperatures around 350-400°C, whereas the marginal areas show 2-3x the expected grain sizes (2.4.2.2), which suggests that grains in the margin was subjected to either higher temperature mechanisms, such as grain boundary migration, or they simply was subjected to an extended period of static recrystallization caused by the strain softening mechanisms and partitioning of working rate (section 3.3.1.1; eq. [13]). Due to the possibility of prolonged injection of magma, it is likely that the quartz crystals initially was relatively large and as cooling progressed they recrystallized to sizes close to the marginal grain sizes (table 2-3), reflecting the high temperature post-RCMP fabric, which may have caused the weak foliation during early stages of low strain deformation (3.2.3). As deformation progressed and

localized, some of the original marginal aggregates, now being the interior, got recrystallized at c. 350-400°C causing abundant subgrain rotation recrystallization microstructures.

Compiling this data into a P-T-t path suggests that the pluton started too cool relatively slow as mangma got injected through a prolonged time resulting in growth of k-fps phorphyroclasts and relatively big quartz grains. When magma infiltration completed, the pluton started to cool with an increased thermal gradient due to the low/moderate temperate ambient country rocks, leaving little microstructural evidence from this event. Possible deformation structures from this temporal evolution may be the weakly developed foliation due to flattening strain, resulting in an L-S fabric (3.2.3). As temperatures decreased toward upper greenschist facies of c. 400-500°C, the thermal gradient lowers due to reaching ambient country rock temperatures and cooling slows down, which reflects the large amounts of greenschist facies deformation. This relatively long period causes a change in the strength contrast (3.3), from a rheological strong clast-bearing framework, of k-fsp phorphyroclasts, towards a boudin-matrix behavior in quartz, which occurs because the spacing between the phorphyroclasts increase, resulting in wider micaceous bands, causing an increased area for neocrystallization of chemically unstable phases (plagioclase and K-fsp). With the decreasing temperature the k-fsp clasts starts to deform brittle, which may enhance fluid circulation because of increased porosity and permeability, resulting in a feed-back process of generating more matrix and thus causing easy nucleation of deformation (i.e., increase strain rate) and the onset of local cataclastic failure. This failure may have occurred with increased strain rate during constant stresses and easy slip, or because of the sealing off of fluidized sections of the shear zones, creating elevated pore pressures. The minimum temperature inferred during late stage fault movements are c. 275°C at 220 MPa (8-8,5 km depth), due to the occurrence of pumpellyite.

3.5. Chapter 3.5: Comparison with similar setting

Antonsdóttir (2006), who was the first to study these fault zones, and especially the Rekvika fault zone, suggests that fault activity can be characterized by intense brittle deformation and the development of cataclasites, which is overprinted by low metamorphic hydrothermal alteration and precipitation of quartz, chlorite, epidote and hematite. These observations are partly in accordance with the results during this study. The biggest difference being that Antonsdóttir (2006) was studying structures of higher crustal levels, mainly developed in the

brittle regime. Brittle structures observed during this study are in accordance with previous work done in the region (Antonsdóttir, 2006; Davids et al., 2013; Indrevær et al., 2014b; Koehl, 2013), where cataclasites associated with post-Caledonian structures occurs (section 1.2.5). This study document that brittle structures acted as fluid conduits during faulting, resulting from elevated fluid pressure, followed by precipitation of hematite along the fracture surfaces. Consequently leading to enhanced fracturing and dilution of the phorphyroclasts (figure 3-4 B) and injection of ultracataclasites into protocataclasites (figure 2-12). This have been a highly dynamic event where the observed ultracataclasites was injected into the protocataclasites (figure 2-12) due to the elevated pore pressures.

Considering the temperature of 350°C and c. 11 km depth; the studied ductile shear zones in the Ersfjord granite lies within the transition zone for plastic- and brittle deformation, and is interpreted as reflecting the plastic deformation regime developed at a very early stage of the Late Carboniferous-Early Triassic rifting. Whereas the cataclasites represents the brittle deformation during the same regional kinematic event at a higher crustal level, where the latest fault activety is documented to have occured at c. 275°C at about c. 8-8,5 km depth, and are in accordance with cataclasites described by Indrevær et al. (2014b).

The observed ENE-WSW striking set of conjugated brittle faults (2.2.3) described within this work, are interpreted as being the same structures Antonsdóttir (2006) described as S_{1a} and S_{2b} during NW-SE orthogonal extension, and are tentatively inferred as being synchronously or slightly following the ductile shear zones, located at lower crustal levels, studied in Grøtfjorden. The implications of the truncating ENE-WSW steep brittle structures are either that they, and thus the Rekvika fault zone, are younger than the ductile and cataclastic structures studied in Grøtfjorden, or that they formed slightly following the formation of the Rekvika fault zone during late stage faulting, which were later than the shear zones and cataclasites observed in this study. Or they are not associated with the formation of the Rekvika fault zone and are of another brittle origin.

During the Late Carboniferous, and associated with early stages of rifting and the opening of the North Atlantic Ocean, an interpreted regional progressive clockwise rotation of the extension regime produced the Rekvika fault zone (Antonsdóttir, 2006), also produces local incremental WNW-ESE oblique-compression as evidenced by dextral simple shear strain localizations (2.2; 2.3.2; figure 2-1). A rotation of the regional oblique-extension strain regime are capable of producing local synthetic oblique-compressive shear zones within a local

compressional regime (figure 3-8). Continuous oblique extension may thus have developed the observed shear zones below the BDT-zone, whereas the observed ENE-WSW brittle structures either excise downwards- and outwards from the Rekvika fault zone, and thus truncates the ductile fabric, simultaneously as the NNW-SSE synthetic compression, or they are caused during continued rotation and are of a later affinity.

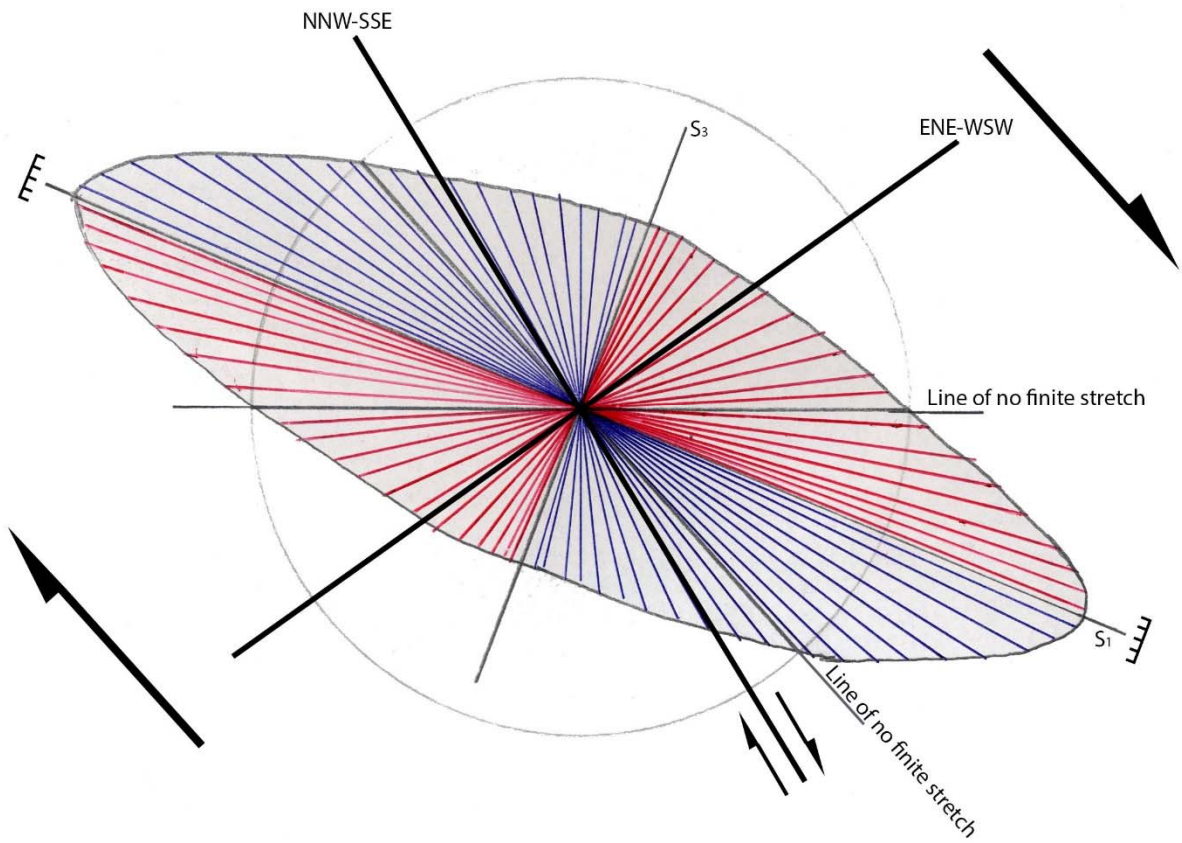

Figure 3-8: Model for the progressive clockwise rotation of the regional strain ellipse, from Late Carboniferous to Early Triassic (maksimum-minimum age based on ages obtained by Davids et al. 2013). This produced NNW-SSE revers shear zones within a local compressive regime (blue area), and ENE-WSW extension faults within a local extension regime (red area).

3.6. Chapter 3.6: Timing of shear zone development and structural evolution

The studied Ersfjord granite shear zones occurs within a regional horst bounded by the Vestfjorden-Vanna and Troms-Finnmark fault complex, linking up the SW Barents Sea margin with the mid-Norwegian passive margin (section 1.2.5; figure 1-5). The margin developed during widespread NNE-SSW right stepped normal faults, interconnected with ENE-WSW

striking faults and auxiliary WNW-ESE trending fracture systems that show an oblique-dextral strike slip motion (this study). The NW-SE trending foliation observed during this study was tentatively interpreted as late Paleoproterozoic fabrics, which have been reactivated during the Paleozoic-Mesozoic rifting. Peak rift activity occurred during Permian through early Triassic (Davids et al., 2013). During this time the initial rifting evolved to a full passive margin (Faleide et al., 2008). The geothermal gradient established in this paper of 30°C/km is common for the upper continental crust, but considering that geothermal gradients for rift environments can reach c. 50°C/km (Indrevær et al. (2014b) and ref. therein), implies that the observed faulting either occurred during early phases of rifting along the SW Barents Sea margin, or that faulting was located along the rift flanks without elevated geothermal gradients.

The onset of the rifting caused brittle faulting or ductile shearing depending on the crustal depth of the structures at that time. The brittle-ductile transition occurs when the Mohr-Coulomb for brittle failure intersects the frictional sliding curve and this is thought to have happened due to elevated pore pressure, as described above (figure 1-1, 3-7). Considering this, it is apparent that the ductile shear zones developed at either depths equivalent of ductile deformation or during periods of lowered pore pressure, as discussed above for a cyclic occurrence of cataclasites, but there is no cyclic occurrence of ductile deformation (i.e., ductile overprints of the cataclastic fabric). Interpretations of this is that strain first localized at depths that allowed ductile deformation, resulting in the dextral shear zone at P-T estimates of c. 11 km and 350°C. With progressive deformation, and perhaps elevation of the thermal gradient due to exhumation, pore pressures caused brittle faulting along the already weakened zones because of strain softening processes during ductile shearing. Geochronological data from Davids et al. (2013) supports a single faulting- and hydrothermal event in western Troms, that would have taken place during the Late Carboniferous-Early Triassic rifting in association with the formation of the Rekvika fault zone (maksimum age of Late Carboniferous), and the progressive clockwise rotation of the regional extension regime (section 3.5). Their AFT data provides evidence for a minimum age constraint for main faulting of c. 200Ma, whereas their $^{40}Ar/^{39}Ar$ age data indicates an age of c. 280-250 Ma and a temperature of about 350-200°C for the hydrothermal event. Both the observed cataclastic phases seem to be ascribed to the Late Permian/Early Triassic, with the last fault activity occurring at a depth of c.8-8,5 km and c. 275°C, as witnessed by the presence of pumpellyite.

AFT data, as mentioned in *section 1.2.5*, suggests that the temperatures dropped below 60°C in the region already by the Late Triassic-Early Jurassic. This implies that the present day surface

was located at depths of c. 2 km, as inferred by the established geothermal gradient, already at that time. The apparent 9 km uplift during active rifting, from Late Carboniferous-Early Triassic, may be explained by footwall uplift due to westward incising and displacement of the crust (Indrevær et al., 2014a). Calculating a minimum average exhumation rate since Late Carboniferous to Late Triassic yields c. 36 m/Ma, which is in close relation to the exhumation rate established by earlier work in the region by Indrevær et al. (2014b). The last 2 km uplift since the Late Triassic-Early Jurassic can be explained by erosion alone. Considering only the static exhumation of 36m/Ma, would produce nearly 8 km uplift, but this does not reflect a probable exhumation history due to it being established during, and for, the active rifting. Seeing that the continental average erosion rates ranges from c. 10-100 m/Ma, and that extensive glacial erosion the last 2,7 Ma occurred in the SW Barents Sea region, with average rates of c. 380 m/Ma (Laberg et al., 2012), it is more probable that erosion explains the uplift.

Another important post-kinematic indicator that enhances the theory of erosional processes being responsible for the last 2 km uplift is static grain growth. The author does not think that substantial post-kinematic grain growth took place, for the following reasons: (1) Grains in the monomineralic layers show anisotropic shape preferred orientations (figure 2-16 D), consistent with the imposed kinematic framework and the recrystallization mechanisms during shearing. (2) In the weakly deformed k-fsp grains, adjacent to quartz aggregates, a smaller, dynamically recrystallized grain size is preserved locally around the phorphyroclasts (figure 3-5). This is interpreted to result from local stress concentrations. If post-kinematic grain growth would have affected the Ersfjord granite shear zones, these highly stressed grains should have disappeared first (Heilbronner et al., 2002). (3) Local mesoscopic observations does not exhibit any further kinematic overprinting relationships.

4. PART 4: CONCLUSIONS

Ductile to semi-ductile shear zones and later stage cataclasites have been studied in the Paleoproterozoic Ersfjord granite (1,79 Ga), along the contact to the Neoarchaean Kattfjord complex and the following conclusions are made:

- Through a case study of the WNW-ESE striking shear zones and cataclasites, comprising detailed field mapping, mesoscale investigation- and analysis of structural elements, the movement is inferred to be oblique-dextral with a dominating strike-slip component; the movement sense is supported by microstructural results obtained from analysis of thin sections, where σ-clasts, quartz shape preffered orientation, S-C mylonites and passive displacement markers display dextral shear sense.
- The mineral assemblages within the ductile shear zones and the cataclasites reflects retrograde reactions, as expected for the observed greenschist metamorphic conditions, and the reaction products acts as weak phases which allows elevated fluid circulation, thus creating a larger area for chemical reactions. The formation of the shear zones are self-feeding in such a way that the production of matrix at each stage during deformation enables further grain size reduction without increasing the stresses.
- The pre-existing foliation was reactivated as a weak zone during strain localization of the WNW-ESE ductile shear zones and cataclasites, and is inferred to be of Paleoproterozoic age, mainly caused by NE-SW contraction during upper greenschist facies deformation, in conjunction with an increased transpressive component, along the Paleoproterozoic crustal margin.
- The foliation produced displacements of 10's of meters with a shear strain (γ) of ~2.
- The ENE-WSW steep brittle faults are associated with the formation of the Rekvika fault complex, and are inferred to have propagated outwards and incised downwards with continued rotation of the oblique-extension regime, truncating the observed ductile- and cataclastic fabrics.

- The Ersfjord granite show mainly fabrics dominated by free rotations within a crystallizing melt-phase (pre-RCMP), and low-temperature fabrics (post-RCMP), which reflects the relatively steep thermal gradient towards the ambient country-rock temperatures.

- Microstructural observations indicate that pore pressures locally reached lithostatic levels (σ_3=290 MPa) during faulting, and that faulting was a highly dynamic process, which caused the faults to act as fluid canals during movement, enhancing chemical reactions.
- Microstructural evidence indicates that the ultracataclasites were fluidized and injected into the protocataclasites, with a minimum fluid velocity of ~0,1-0,5 m/s. The maximum differential stresses during faulting is inferred to 40 MPa, assuming a typical Mohr-Coulomb failure criteria.
- The shear zones record a progressive strain gradient toward the core zone (i.e., strain softening) and result in bigger grain sizes along the shear zone margins than for the interior, which produced a change in deformation mechanism from dislocation creep of the aggregates to diffusion creep in the matrix.
- The bulk strain rate is calculated to have been in the order of 10^{-15} s^{-1}, which is too slow for mylonitization. Extensive static recrystallization occurred within quartz aggregates subjected to dislocation creep, causing grain growth during progressive deformation of the matrix.
- The matrix phase have obtained grain size equilibrium at ~20µm and are deforming by diffusion creep processes such as granular flow and dissolution-precipitation.

- Late Carboniferous-Early Triassic fault activity associated with the evolution of the continental margin of Northern Norway occurred, where the observed faults lie within the brittle-ductile transition of minimum 11-12 km depths (290 MPa) and ~350°C, based on greenschist facies mineral assemblages. Late fault movements and fluid infiltration precipitated chlorite within the faults causing reactions between chlorite and epidote, resulting in the formation of pumpellyite which yields a minimum pressure-temperature condition of 8-8,5 km depths (220 MPa) and ~275°C.
- A clockwise rotation of the regional extension regime, which formed the Rekvika fault zone also produced local compressional regimes, as evidenced by the WNW-ESE shear zones. The formation of the ductile shear zones are at early stages of rifting and associated with the formation of the Rekvika fault zone.
- Data obtained during this study suggests that extensional tectonics produced the observed shear zones in association with early-stage rifting in Late Carboniferous, and produced ~9km uplift during rifting. The last ~2-3 km uplift are explained by erosion

alone, and supported by the absence of post-kinematic grain growth, due to the occurrence of highly stressed recrystallized grains, and grains that display SPO consistent with the imposed kinematic framework during deformation.

5. PART 5: REFERENCES

[1] www.esci.umn.edu/people/researchers/withe012/fugacity.htm

Andersen, A. (1979). The age of the Precambrian basement in western Troms, Norway. *Geologiska Föreningens i Stockholm Förhandlingar, 101*, 291-298.

Andersen, A., & Forslund, T. (1987). Post-Caledonian brittle faults in Troms: Geometry, age and tectonic significance. [Abstract].

Anderson, M., Barker, A., Bennett, D., & Dallmeyer, R. (1992). A tectonic model for Scandian terrane accretion in the northern Scandinavian Caledonides. *Journal of the Geological Society, 149*(5), 727-741.

Andresen, A. (1988). Caledonian terranes of northern Norway and their characteristics. *Trabajos de geología, 17*, 103-117.

Andresen, A., & Tull, J. (1983). The age of the Lødingen granite and its possible regional significance. *Norsk geologisk tidsskrift, 63*(4), 269-276.

Antonsdóttir, V. (2006). Structural and kinematic analysis of the post-Caledonian Rekvika Fault Zone, Kvaløya, Troms.

Armitage, P. E. B., & Bergh, S. G. (2005). Structural development of the Mjelde-Skorelvvaten Zone on Kvaløya, Troms: a metasupracrustal shear belt in the Precambrian West Troms Basement Complex, North Norway. *Norwegian Journal of Geology, 85*, 117-132.

Austin, N., & Evans, B. (2009). The kinetics of microstructural evolution during deformation of calcite. *Journal of Geophysical Research: Solid Earth (1978–2012), 114*(B9).

Austin, N. J., & Evans, B. (2007). Paleowattmeters: A scaling relation for dynamically recrystallized grain size. *Geology, 35*(4), 343-346.

Bergh, S. G., Corfu, F., Myhre, P. I., Kullerud, K., Armitage, P. E., Zwaan, K. B., et al. (2012). Was the Precambrian Basement of Western Troms and Lofoten-Vesterålen in Northern Norway Linked to the Lewisian of Scotland? A Comparison of Crustal Components, Tectonic Evolution and Amalgamation History.

Bergh, S. G., Eig, K., Kløvjan, O. S., Henningsen, T., Olesen, O., & Hansen, J.-A. (2007a). The Lofoten-Vesterålen continental margin: a multiphase Mesozoic-Palaeogene rifted shelf as shown by offshoreonshore brittle fault-fracture analysis. *Norwegian Journal of Geology, 87*, 29-58.

Bergh, S. G., Kullerud, K., Armitage, P. E., Zwaan, K. B., Corfu, F., Ravna, E. J., et al. (2010). Neoarchaean to Svecofennian tectono-magmatic evolution of the West Troms basement complex, North Norway. *Nor J Geol, 90*, 21-48.

Bergh, S. G., Kullerud, K., Corfu, F., Armitage, P. E., Davidsen, B., Johansen, H. W., et al. (2007b). Low-grade sedimentary rocks on Vanna, North Norway: a new occurrence of a Palaeoproterozoic (2.4-2.2 Ga) cover succession in northern Fennoscandia. *NORSK GEOLOGISK TIDSSKRIFT, 87*(3), 301.

Bleeker, W. (2003). The late Archean record: a puzzle in ca. 35 pieces. *Lithos, 71*(2), 99-134.

Bruges, E., Latto, B., & Ray, A. (1966). New correlations and tables of the coefficient of viscosity of water and steam up to 1000 bar and 1000 C. *International Journal of Heat and Mass Transfer, 9*(5), 465-480.

Bruhn, R. L., Parry, W. T., Yonkee, W. A., & Thompson, T. (1994). Fracturing and hydrothermal alteration in normal fault zones. *Pure and Applied Geophysics, 142*(3-4), 609-644.

Condie, K. C. (2005). TTGs and adakites: are they both slab melts? *Lithos, 80*(1), 33-44.

Corfu, F. (2004). U-Pb age, setting and tectonic significance of the anorthosite-mangerite-charnockite-granite suite, Lofoten-Vesteralen, Norway. *Journal of Petrology, 45*(9), 1799-1819.

Corfu, F., Armitage, P. E., Kullerud, K., & Bergh, S. G. (2003). Preliminary U-Pb geochronology in the West Troms Basement Complex, North Norway: Archaean and Palaeoproterozoic events and younger overprints. *NORGES GEOLOGISKE UNDERSOKELSE, 441*, 61-72.

Corfu, F., Kullerud, K., & Bergh, S. G. (2006). U-Pb constraints on the Late Palaeoproterozoic evolution of the West Troms Basement Complex, northern Norway. *Geological Society of Finland Bulletin, Special Issue, 1*, 23.

Dallmeyer, R. D. (1992). Ar-40/Ar-39 Mineral Ages within the Western Gneiss Terrane, Troms, Norway - Evidence for Polyphase Proterozoic Tectonothermal Activity (Svecokarilian and Sveconorwegian). *Precambrian Research, 57*(3-4), 195-206.

Davids, C., Wemmer, K., Zwingmann, H., Kohlmann, F., Jacobs, J., & Bergh, S. G. (2013). K-Ar illite and apatite fission track constraints on brittle faulting and the evolution of the nothern Norwegian passive margin. *Tectonophysics*(608), 15.

De Ronde, A., Heilbronner, R., Stünitz, H., & Tullis, J. (2004). Spatial correlation of deformation and mineral reaction in experimentally deformed plagioclase–olivine aggregates. *Tectonophysics, 389*(1), 93-109.

Faleide, J. I., Tsikalas, F., Breivik, A. J., Mjelde, R., Ritzmann, O., Engen, O., et al. (2008). Structure and evolution of the continental margin off Norway and the Barents Sea. *Episodes, 31*(1), 82.

Fitz Gerald, J., & Stünitz, H. (1993). Deformation of granitoids at low metamorphic grade. I: reactions and grain size reduction. *Tectonophysics, 221*(3), 269-297.

Forslund, T. (1988). Post-Kaledonske forkastninger i Vest-Troms, med vekt på kvaløyslettaforkastningen, Kvaløya. *Hovedfagsoppgave i geologi, Universitetet i Tromsø*.

Forslund, T. (1988). Post-kaledonske forkastninger i Vest-Troms, med vekt på Straumsbukta-Kvaløysletta forkastningen. *Kvaløya. Unpubl. Cand. Scient thesis, University of Tromsø*.

Gay, N. (1968). Pure shear and simple shear deformation of inhomogeneous viscous fluids. 1. Theory. *Tectonophysics, 5*(3), 211-234.

Gjerløw, E. (2008). Petrologi og alder av høymetamorfe mafiske bergarter i det vestlige gneiskomplekset i Troms. *Unpublished Master thesis*, 90.

Gleason, G. C., & Tullis, J. (1995). A flow law for dislocation creep of quartz aggregates determined with the molten salt cell. *Tectonophysics, 247*(1), 1-23.
Goldstein, A., & Marshak, S. (1988). *Analysis of fracture array geometry.* (vol. Basic methods of structural geology). In: Marshak, S & Mitra, G. (eds.)
Gorbatschev, R., & Bogdanova, S. (1993). Frontiers in the Baltic shield. *Precambrian Research, 64*(1), 3-21.
Handy, M. R. (1990). The solid-state flow of polymineralic rocks. *Journal of Geophysical Research: Solid Earth (1978–2012), 95*(B6), 8647-8661.
Hanmer, S., & Passchier, C. W. (1991). Shear sense indicators: a review. *Geol. Survey of Canada, 90*(17).
Heilbronner, R., & Tullis, J. (2002). The effect of static annealing on microstructures and crystallographic preferred orientations of quartzites experimentally deformed in axial compression and shear. *Geological Society, London, Special Publications, 200*(1), 191-218.
Henkel, H. (1991). Magnetic crustal structures in northern Fennoscandia. *Tectonophysics, 192*(1), 57-79.
Hippertt, J. (1998). Breakdown of feldspar, volume gain and lateral mass transfer during mylonitization of granitoid in a low metamorphic grade shear zone. *Journal of Structural Geology, 20*(2), 175-193.
Hippertt, J., & Hongn, F. (1998). Deformation mechanisms in the mylonite/ultramylonite transition. *Journal of Structural Geology, 20*(11), 1435-1448.
Hirth, G., Teyssier, C., & Dunlap, J. W. (2001). An evaluation of quartzite flow laws based on comparisons between experimentally and naturally deformed rocks. *International Journal of Earth Sciences, 90*(1), 77-87.
Hirth, G., & Tullis, J. (1992). Dislocation creep regimes in quartz aggregates. *Journal of Structural Geology, 14*(2), 145-159.
Hirth, G., & Tullis, J. (1994). The brittle-plastic transition in experimentally deformed quartz aggregates. *Journal of Geophysical Research: Solid Earth (1978–2012), 99*(B6), 11731-11747.
Hutton, D. H. (1988). Granite emplacement mechanisms and tectonic controls: inferences from deformation studies. *Transactions of the Royal Society of Edinburgh: Earth Sciences, 79*(2-3), 245-255.
Indrevær, K. (2011). The Tromsø Nappe Contact with the Nakkedal Nappe Complex NE of Tromsdalstind: Shear kinematics and relationship with metamorphism.
Indrevær, K., Bergh, S. G., Koehl, J.-B., Hansen, J.-A., Schermer, E. R., & Ingebrigtsen, A. (2014a). Post-Caledonian brittle fault zones on the hyper-extended SW Barents Sea Margin: New insights into onshore and offshore margin architecture.
Indrevær, K., Stunitz, H., & Bergh, S. G. (2014b). High pressure fluid flow during Paleozoic-Mesozoic brittle normal faulting along the SW Barents Sea margin: Implications for past and present basement permeability.

Keilhau, B. M. (1861). Beretning om en geologisk reise til Nordlandene i 1855. *Nyt. Mag. Nat., 11*(209-221).
Kilian, R., Heilbronner, R., & Stünitz, H. (2011). Quartz microstructures and crystallographic preferred orientation: Which shear sense do they indicate? *Journal of Structural Geology, 33*(10), 1446-1466.
Koehl, J.-B. P. (2013). Late Paleozoic-Cenozoic fault correlation and characterization of fault rocks in western Troms, North Norway.
Kohlstedt, D., Evans, B., & Mackwell, S. (1995). Strength of the lithosphere: Constraints imposed by laboratory experiments. *Journal of Geophysical Research, 100*(B9), 17587-17517,17602.
Kullerud, K., Corfu, F., Bergh, S., Davidsen, B., & Ravna, E. (2006a). U-Pb constraints on the Archaean and Early Proterozoic evolution of the West Troms Basement Complex, North Norway. *Geological Society of Finland Bulletin, Special Issue 1*.
Kullerud, K., Skjerlie, K. P., Corfu, F., & de la Rosa, J. D. (2006b). The 2.40 Ga Ringvassøy mafic dykes, West Troms Basement Complex, Norway: the concluding act of early Palaeoproterozoic continental breakup. *Precambrian Research, 150*(3), 183-200.
Laberg, J. S., Andreassen, K., & Vorren, T. O. (2012). Late Cenozoic erosion of the high-latitude southwestern Barents Sea shelf revisited. *Geological Society of America Bulletin, 124*(1-2), 77-88.
Lister, G., & Snoke, A. (1984). SC mylonites. *Journal of Structural Geology, 6*(6), 617-638.
Luan, F. C., & Paterson, M. S. (1992). Preparation and deformation of synthetic aggregates of quartz. *Journal of Geophysical Research: Solid Earth, 97*(B1), 301-320.
Lucas, S. B., & St-Onge, M. R. (1995). Syn-tectonic magmatism and the development of compositional layering, Ungava Orogen (northern Quebec, Canada). *Journal of Structural Geology, 17*(4), 475-491.
Miller, R. B., & Paterson, S. R. (1994). The transition from magmatic to high-temperature solid-state deformation: implications from the Mount Stuart batholith, Washington. *Journal of Structural Geology, 16*(6), 853-865.
Mitra, G. (1978). Ductile deformation zones and mylonites; the mechanical processes involved in the deformation of crystalline basement rocks. *American Journal of Science, 278*(8), 1057-1084.
Moreira da Silva, A., & Rielly, C. (1996). *Modelling the mixing of miscible liquids with a large viscosity difference in constricted channel flow.* Innlegg på INSTITUTION OF CHEMICAL ENGINEERS SYMPOSIUM SERIES.
Motuza, G., Motuza, V., Beliatsky, B., & Savva, E. (2001). *Volcanic rocks of the Ringvassøya Greenstone Belt (North Norway): implication for the stratigraphy and tectonic setting.* Innlegg på Journal of Conference.
Myhre, P. I., Corfu, F., & Bergh, S. (2011). Palaeoproterozoic (2.0–1.95 Ga) pre-orogenic supracrustal sequences in the West Troms Basement Complex, North Norway. *Precambrian Research, 186*(1), 89-100.

Myhre, P. I., Corfu, F., Bergh, S. G., Kullerud, K., Eilertsen, R. S., Olsen, N. R., et al. (2013). U–Pb geochronology along an Archaean geotransect in the West Troms Basement Complex, North Norway. *Norwegian Journal of Geology, 93*(1), 1-24.

Nyheim, H., Bergh, S. G., Krogh, E. J., & Zwaan, K. B. (1994). Torsnes-skjærsonen i det vestlige (nord-norske) gneisterreng, Kvaløya, Troms; evidenser for kompleks skorpeforkortning og orogen- parallell oblik strike- slip. *Nordic Geological Winter Meeting, Luleå*.

Olesen, N. Ø. (1987). Plagioclase fabric development in a high-grade shear zone, Jotunheimen, Norway. *Tectonophysics, 142*(2), 291-308.

Olesen, O., Torsvik, T. H., & Tveten, E. (1997). Basement structure of the continental margin in the Lofoten-Lopphavet area, northern Norway: constraints from potential field data, on-land structural mapping and palaeomagnetic data. *Oceanographic Literature Review, 44*(12).

Passchier, C. W., & Simpson, C. (1986). Porphyroclast systems as kinematic indicators. *Journal of Structural Geology, 8*(8), 831-843.

Passchier, C. W., & Trouw, R. A. (2005). *Microtectonics*: Springer-Verlag Berlin Heidelberg.

Paterson, S. R., Vernon, R. H., & Tobisch, O. T. (1989). A review of criteria for the identification of magmatic and tectonic foliations in granitoids. *Journal of structural geology, 11*(3), 349-363.

Pedersen, B. R. S. (1997). Strukturell analyse av en prekambrisk, duktilt deformert metasuprakrustalsone (Astridal- skjærsonen?) på NØ-Senja, Troms. *Unpublished Cand. Scient. thesis, University of Tromsø*.

Pennacchioni, G. (2005). Control of the geometry of precursor brittle structures on the type of ductile shear zone in the Adamello tonalites, Southern Alps (Italy). *Journal of Structural Geology, 27*(4), 627-644.

Pettersen, K. J. (1887). Den nord-norske fjeldbygning I. *Tromsø Museums Årshefte, 10*.

Pettersen, K. J. (1891). Geologiske kart over Tromsø amt. *Tromsø Museums Årshefte, 14*.

Pitzer, K. S., & Sterner, S. M. (1994). Equations of state valid continuously from zero to extreme pressures for H2O and CO2. *The Journal of chemical physics, 101*(4), 3111-3116.

Poirier, J. (1980). Shear localization and shear instability in materials in the ductile field. *Journal of Structural Geology, 2*(1), 135-142.

Ramsay, J., & Huber, M. (1983). The Techniques of Modern Structural Geology, Vol. 1: Strain Analysis: Academic Press, London.

Roberts, D. (2003). The Scandinavian Caledonides: event chronology, palaeogeographic settings and likely modern analogues. *Tectonophysics, 365*(1), 283-299.

Romer, R. L., Kjøsnes, B., Korneliussen, A., Lindahl, I., Skyseth, T., Stendal, M., et al. (1992). The Archean-Proterozoic boundary beneath the Caledonides of nothern Norway and Sweden: U-Pb, Rb-Sr, and εNd isotope data from the Rombak-Tysfjord area. *NORGES GEOLOGISKE UNDERSOKELSE*(91.225), 76.

Schmidt, E. H., & Mayinger, F. (1963). *Viscosity of Water and Steam at High Pressures and Temperatures Up to 800 Atmospheres and 700° C.* Innlegg på Modern Developments in Heat Transfer.

Schofield, D. I., & D'Lemos, R. S. (1998). Relationships between syn-tectonic granite fabrics and regional PTtd paths: an example from the Gander-Avalon boundary of NE Newfoundland. *Journal of Structural Geology, 20*(4), 459-471.

Segall, P., & Pollard, D. D. (1983). Nucleation and growth of strike slip faults in granite. *Journal of Geophysical Research: Solid Earth (1978–2012), 88*(B1), 555-568.

Segall, P., & Simpson, C. (1986). Nucleation of ductile shear zones on dilatant fractures. *Geology, 14*(1), 56-59.

Shimamoto, T. (1989). The origin of S-C mylonites and a new fault-zone model. *Journal of structural geology, 11*(1), 51-64.

Shimizu, I. (2008). Theories and applicability of grain size piezometers: The role of dynamic recrystallization mechanisms. *Journal of Structural Geology, 30*(7), 899-917.

Sibson, R. (1977). Fault rocks and fault mechanisms. *Journal of the Geological Society, 133*(3), 191-213.

Siivola, J., & Schmid, R. (version 01.02.07). List of Mineral Abbreviations. *Recommendations by the IUGS Subcommission on the Systematics of Metamorphic Rocks: Webversion 01.02.07*

Simpson, C. (1985). Deformation of granitic rocks across the brittle-ductile transition. *Journal of Structural Geology, 7*(5), 503-511.

Simpson, C. (1986). Fabric development in brittle-to-ductile shear zones. *pure and applied geophysics, 124*(1-2), 269-288.

Simpson, C., & De Paor, D. G. (1993). Strain and kinematic analysis in general shear zones. *Journal of Structural Geology, 15*(1), 1-20.

Smith, P., & Parsons, I. (1974). The alkali-feldspar solvus at 1 kilobar water-vapour pressure. *Mineral Mag, 39*, 747-767.

Spear, F. S. (1995). Metamorphic phase equilibria and pressure-temperature-time paths.

Steltenpohl, M. G., Moecher, D., Andresen, A., Ball, J., Mager, S., & Hames, W. E. (2011). The Eidsfjord shear zone, Lofoten–Vesterålen, north Norway: an Early Devonian, paleoseismogenic low-angle normal fault. *Journal of Structural Geology, 33*(5), 1023-1043.

Stipp, M., StuÈnitz, H., Heilbronner, R., & Schmid, S. M. (2002b). The eastern Tonale fault zone: a 'natural laboratory'for crystal plastic deformation of quartz over a temperature range from 250 to 700 C. *Journal of Structural Geology, 24*(12), 1861-1884.

Stipp, M., Stünitz, H., Heilbronner, R., & Schmid, S. M. (2002a). Dynamic recrystallization of quartz: correlation between natural and experimental conditions. *Geological Society, London, Special Publications, 200*(1), 171-190.

Stipp, M., & Tullis, J. (2003). The recrystallized grain size piezometer for quartz. *Geophysical Research Letters, 30*(21).
Stipp, M., Tullis, J., Scherwath, M., & Behrmann, J. H. (2010). A new perspective on paleopiezometry: Dynamically recrystallized grain size distributions indicate mechanism changes. *Geology, 38*(8), 759-762.
Thorstensen, L. (2011). Land-sokkel korrelasjon av tektoniske elementer i ytre del av Senja og Kvaløya i Troms.
Tribe, I. R., & D'Lemos, R. S. (1996). Significance of a hiatus in down-temperature fabric development within syn-tectonic quartz diorite complexes, Channel Islands, UK. *Journal of the Geological Society, 153*(1), 127-138.
Twiss, R. J. (1977). Theory and applicability of a recrystallized grain size paleopiezometer. I *Stress in the Earth* (s. 227-244): Springer.
Vollmer, F. (2011). Orient 2.1.2. *www.frederickvollmer.com*.
Wilson, J., Chester, J., & Chester, F. (2003). Microfracture analysis of fault growth and wear processes, Punchbowl Fault, San Andreas system, California. *Journal of structural geology, 25*(11), 1855-1873.
Zwaan, K. (1995). Geology of the Precambrian West Troms Basement Complex, northern Norway, with special emphasis on the Senja Shear Belt: a preliminary account. *Norges geologiske undersøkelse Bulletin, 427*, 33-36.
Zwaan, K., & Tucker, R. (1996). *Absolute and relative age relationships in the Precambrian West Troms Basement Complex, northern Norway.* Innlegg på 22nd Nordic Geological Winter Meeting, Åbo, Finland.
Zwaan, K. B. (1992a). Database for alle geologiske opplysninger om forkastninger og skjærsoner som opptrer på kartblad 1:250000 Tromsø. *NORGES GEOLOGISKE UNDERSOKELSE, 92.107*.
Zwaan, K. B. (1992b). Database for alle geologiske opplysninger om den prekambriske geologien på Kvaløya, Troms fylke. *NORGES GEOLOGISKE UNDERSOKELSE, 92.104*.
Zwaan, K. B., Fareth, E., & Grogan, P. W. (1998). Geologiske kart over norge, berggrunskart Tromsø, M 1:250000. *NORGES GEOLOGISKE UNDERSOKELSE*.

6. PART 6: APPENDICES

Apendix 1: Raw data used for estimating the fabric trajectories in section 2.4.2.3, where the methods are highlighted in 1.3.3.2

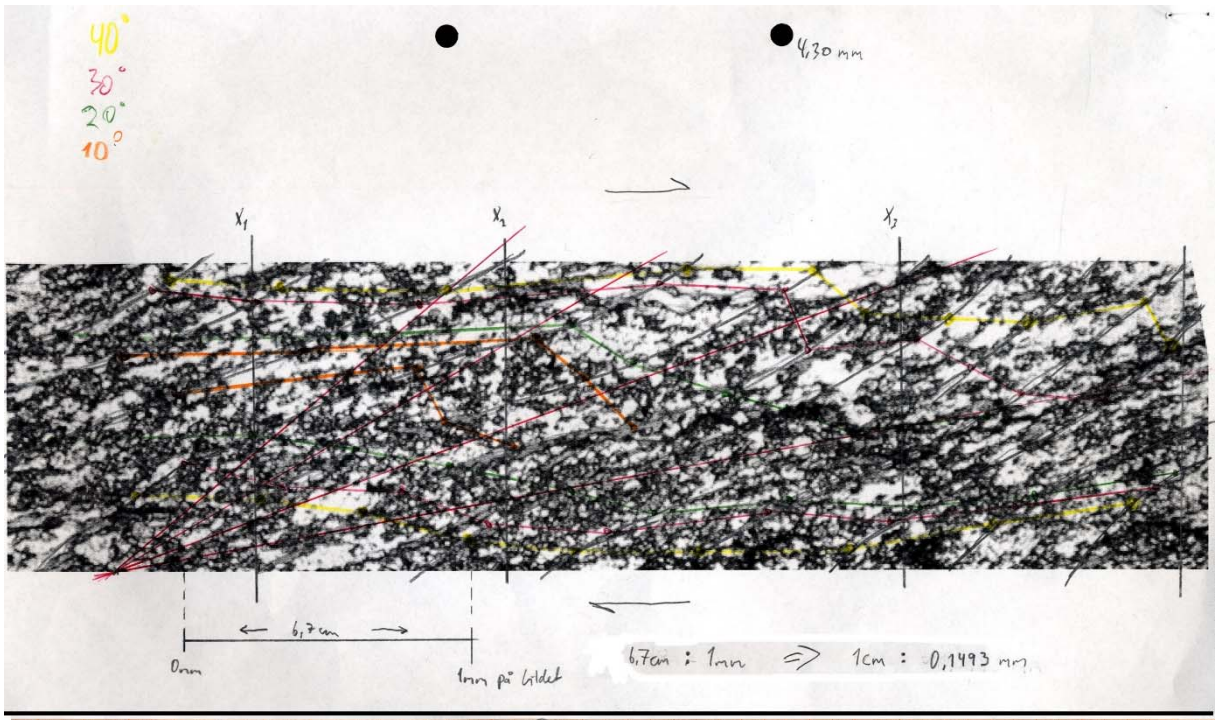

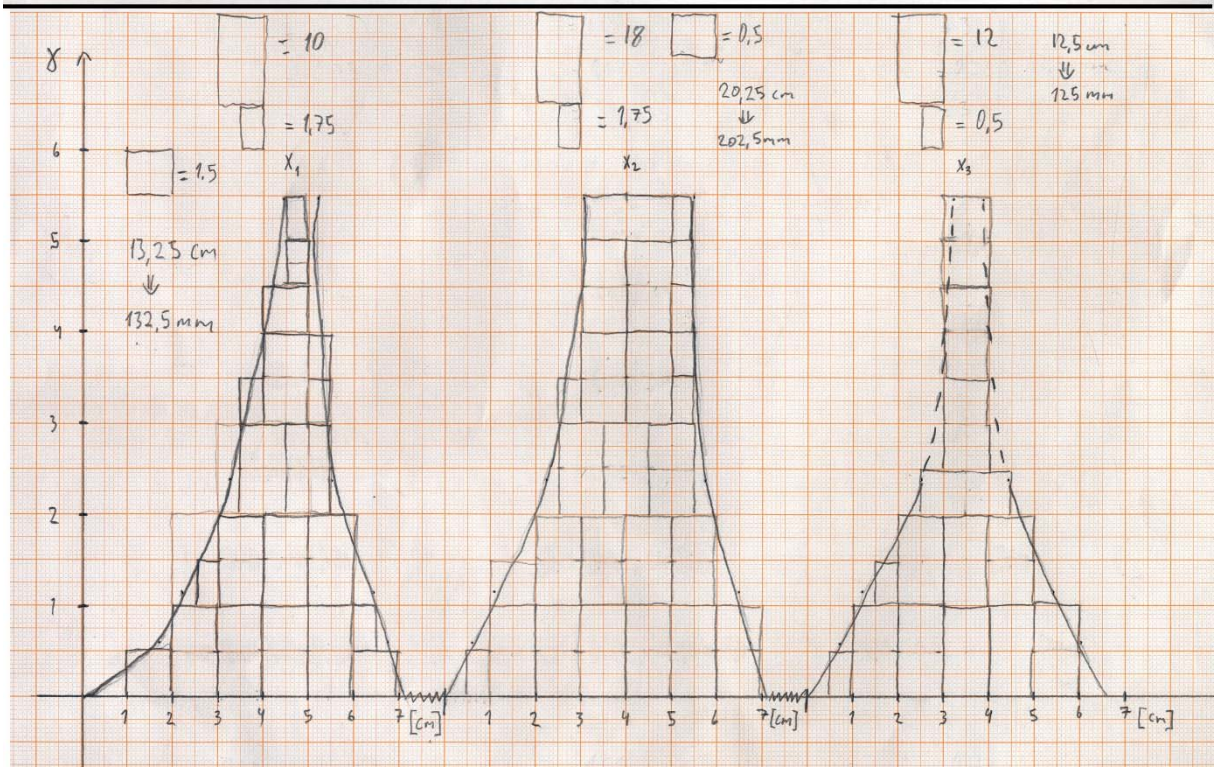

Apendix 2: MatLAB code used to generate Diagram 2-2, based on the methods described in section 1.3.3.2.

```
clear all
close all
clc

%defining the three cross sections as s1-s6. y is the defined gamma values
y = [0.35 1.15 2.38 5.49];
s1 = [1.7 2.2 3.25 4.45];
s2 = [6.75 6.45 5.55 5.2];

s3 = [0.6 1.1 2.25 3.05];
s4 = [6.75 6.5 5.75 5.5];

s5 = [0.7 1.2 2.5 3.2];
s6 = [6.05 5.45 4.45 3.9];
%plotting the cross sections
figure(1)
plot(s1,y,'-b',s2,y,'-b', 'linewidth',1.5)
hold on
plot(s3,y,'-r',s4,y,'-r', 'linewidth',1.5)
plot(s5,y,'-g',s6,y,'-g', 'linewidth',1.5)
%setting parameters for the x- and y-axis
set(gca, 'YTick', 0:0.5:6)
set(gca, 'xtick', 0:0.5:7)
grid on
xlabel('Displacement [cm]')
ylabel('Shear strain')
title('Plot of displacement')
legend('data1','data2','data3','data4','data5','data6','location','best')
%creating the file as a .png with 1200 dpi and with a name
%'fabrictrajectories'
figure(1)
print -dpng -r1200 fabrictrajectories
```

Published with MATLAB® R2013b

Apendix 3: MatLAB r2013b code used to produce Diagram 2-3, and methods described in section 1.3.3.4.

```
clear all
close all
clc

z=(1000);   %Indrevær, 2014b resultat av slip rate
a=(0.3706);        %Indrevær, 2014b resultat av slip rate

x = linspace(0,3000);    %creates a row vector between 0 and 3000
%linear relationships calculated using 100 um grain sizes
y = -2.1779*10^-4*(x)+0.588;    %0,1 centipoise@Indrevær,2014b variabler
v = -3.364*10^-4*(x)+0.908;     %0,0648 centipoise @ 350 gC
b = -2.995*10^-4*(x)+0.808;     %0,0728 centipoise @ 350 gC

%linear relationships calculated using 50 um grain sizes
g = -8.41*10^-5*(x)+0.227;  %0,0648 cP and 50 um grain size
h = -7.486*10^-5*(x)+0.202; %0,0728 cP and 50 um grain size

figure(1)
hold on
plot(x,y, '--r')    %plot work by Indrevær et al. 2014b
plot(z,a, 'or')     %obtained slip rate @ Indrevær et al. 2014
plot(x,v, '-k', 'linewidth',2)  %plots the black graph
plot(x,b, '-b', 'linewidth',2)  %plots the blue graph
plot(x,g, '-c', 'linewidth',2)  %plots the cyan graph
plot(x,h, '-m', 'linewidth',2)  %plots the magenta graph
set(gca, 'YTick', 0:0.075:1.0)  %defines the y-axis interval
axis ([0 3000 0 1])             %defines the x- and y-axis lenght
grid off

xlabel('Fluid density [kg/m^3]')
ylabel('Slip rate [m/s]')
title('Fluid flow velocity and slip rates as a function of fluid density')

%saves the graph as a .png with a dpi of 1200 and name 'fluidflow'
figure(1)
print -dpng -r1200 fluidflow
```

Published with MATLAB® R2013b

Apendix 4: Two BSD spectrums; spectrum 16, 53 and 63 are representing sample DP07_1, and spectrum 51 is representing sample DP12_2. Methods described in section 1.3.4.1.

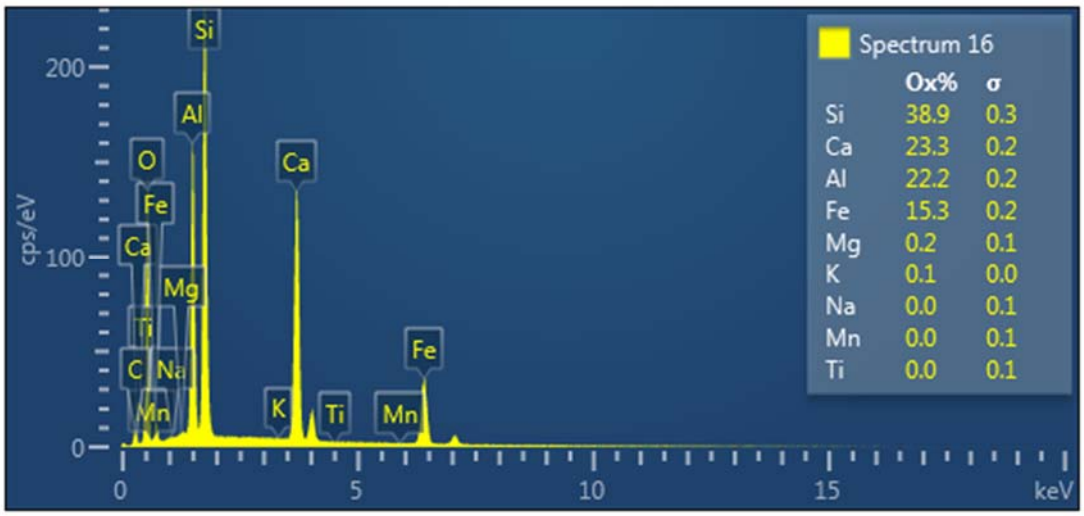

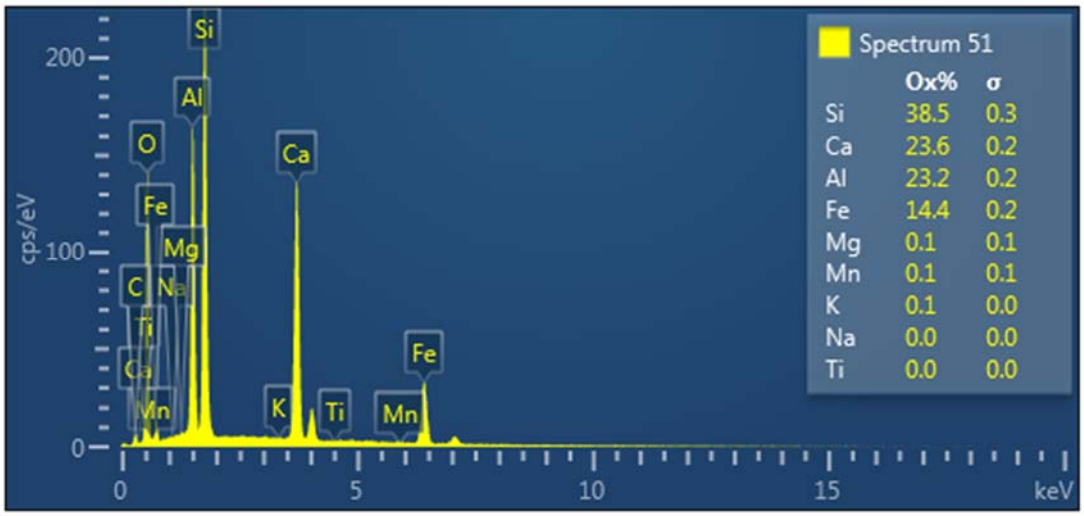

Analysis title		spectra 16			kat			
					formula =			
				kat	8,0			
Oxide	**GFW**	**Wt.%**	**Mole Units**	**Kation Units**	**Normaliz. kat Units**		**Expected value**	**Actual value**
SiO2	60,084	38,87	**0,64693**	**0,64693**	**3,01**	**Si**	3	3,01
TiO2	79,866	0,00	0,00000	0,00000	0,00	**Ti**		
Al2O3	101,961	22,21	0,21783	0,43566	2,03	**Al**		
Cr2O3	151,9902	0,00	0,00000	0,00000	0,00	**Cr**		
Fe2O3	159,688	0,00	0,00000	0,00000	0,00	**Fe+3**		
FeO	71,844	15,33	0,21338	0,21338	0,99	**Fe+2**		
MnO	70,937	0,00	0,00000	0,00000	0,00	**Mn**		
MgO	40,304	0,18	**0,00447**	**0,00447**	**0,02**	**Mg**	3	3,04
CaO	56,077	23,32	**0,41586**	**0,41586**	**1,94**	**Ca**	2	1,94
Na2O	61,979	0,03	0,00048	0,00097	0,00	**Na**	=	4,98
K2O	94,196	0,06	0,00064	0,00127	0,01	**K**		
H2O	18,015	0,00	0,00000	0,00000	0,00	**H**		
Totals		**100,00**	**1,49958**	**1,71853**	**8,00000**	**0,000**		

Analysis title		spectra 51			kat			
					formula =			
				kat	8,0			
Oxide	**GFW**	**Wt.%**	**Mole Units**	**Kation Units**	**Normaliz. kat Units**		**Expected value**	**Actual value**
SiO2	60,084	38,48	**0,64044**	**0,64044**	**2,97**	**Si**	3	2,97
TiO2	79,866	0,00	0,00000	0,00000	0,00	**Ti**		
Al2O3	101,961	23,22	0,22773	0,45547	2,12	**Al**		
Cr2O3	151,9902	0,00	0,00000	0,00000	0,00	**Cr**		
Fe2O3	159,688	0,00	0,00000	0,00000	0,00	**Fe+3**		
FeO	71,844	14,42	0,20071	0,20071	0,93	**Fe+2**		
MnO	70,937	0,07	0,00099	0,00099	0,00	**Mn**		
MgO	40,304	0,09	**0,00223**	**0,00223**	**0,01**	**Mg**	3	3,06
CaO	56,077	23,63	**0,42138**	**0,42138**	**1,96**	**Ca**	2	1,96
Na2O	61,979	0,00	0,00000	0,00000	0,00	**Na**	=	5,02
K2O	94,196	0,07	0,00074	0,00149	0,01	**K**		
H2O	18,015	0,00	0,00000	0,00000	0,00	**H**		
Totals		**99,98**	**1,49423**	**1,72271**	**8,00000**	**0,000**		

Analysis title		spectra 53			kat			
					formula =			
				kat	8,0			
Oxide	**GFW**	**Wt.%**	**Mole Units**	**Kation Units**	**Normaliz. kat Units**		**Expected value**	**Actual value**
SiO2	60,084	38,17	**0,63528**	**0,63528**	**2,96**	**Si**	3	2,96
TiO2	79,866	0,17	0,00213	0,00213	0,01	**Ti**		
Al2O3	101,961	22,06	0,21636	0,43271	2,02	**Al**		
Cr2O3	151,9902	0,00	0,00000	0,00000	0,00	**Cr**		
Fe2O3	159,688	0,00	0,00000	0,00000	0,00	**Fe+3**		
FeO	71,844	15,24	0,21213	0,21213	0,99	**Fe+2**		
MnO	70,937	0,13	0,00183	0,00183	0,01	**Mn**		
MgO	40,304	0,07	**0,00174**	**0,00174**	**0,01**	**Mg**	3	3,02
CaO	56,077	24,09	**0,42959**	**0,42959**	**2,00**	**Ca**	2	2,00
Na2O	61,979	0,06	0,00097	0,00194	0,01	**Na**	=	5,02
K2O	94,196	0,02	0,00021	0,00042	0,00	**K**		
H2O	18,015	0,00	0,00000	0,00000	0,00	**H**		
Totals		**100,01**	**1,50023**	**1,71776**	**8,00000**	**0,000**		

Analysis title		spectra 63			kat			
					formula =			
				kat	8,0			
Oxide	**GFW**	**Wt.%**	**Mole Units**	**Kation Units**	**Normaliz. kat Units**		**Expected value**	**Actual value**
SiO2	60,084	38,24	**0,63644**	**0,63644**	**2,96**	**Si**	3	2,96
TiO2	79,866	0,23	0,00288	0,00288	0,01	**Ti**		
Al2O3	101,961	22,00	0,21577	0,43154	2,01	**Al**		
Cr2O3	151,9902	0,00	0,00000	0,00000	0,00	**Cr**		
Fe2O3	159,688	0,00	0,00000	0,00000	0,00	**Fe+3**		
FeO	71,844	15,33	0,21338	0,21338	0,99	**Fe+2**		
MnO	70,937	0,18	0,00254	0,00254	0,01	**Mn**		
MgO	40,304	0,11	**0,00273**	**0,00273**	**0,01**	**Mg**	3	3,03
CaO	56,077	23,80	**0,42442**	**0,42442**	**1,98**	**Ca**	2	1,98
Na2O	61,979	0,12	0,00194	0,00387	0,02	**Na**	=	5,00
K2O	94,196	0,00	0,00000	0,00000	0,00	**K**		
H2O	18,015	0,00	0,00000	0,00000	0,00	**H**		
Totals		**100,01**	**1,50009**	**1,71779**	**8,00000**	**0,000**		

UNIVERSITY OF TROMSØ